PASSIVE ANTENNA SENSOR DESIGN THROUGH MULTI-PHYSICS MODELING, SIMULATION, AND OPTIMIZATION

A Dissertation
Presented to
The Academic Faculty

by

Chunhee Cho

In Partial Fulfillment
of the Requirements for the Degree
Doctor of Philosophy in the
School of Civil and Environmental Engineering

Georgia Institute of Technology
December 2016

PASSIVE ANTENNA SENSOR DESIGN THROUGH MULTI-PHYSICS MODELING, SIMULATION, AND OPTIMIZATION

Approved by:

Dr. Yang Wang, Advisor
School of Civil and Environmental Engineering
Georgia Institute of Technology

Dr. Phanish Suryanarayana
School of Civil and Environmental Engineering
Georgia Institute of Technology

Dr. Manos M. Tentzeris
School of Electrical and Computer Engineering
Georgia Institute of Technology

Dr. Ying Zhang
School of Electrical and Computer Engineering
Georgia Institute of Technology

Dr. Xiaohua Yi
Senior Research Engineer
ExxonMobil Corporation

Date Approved: [November 2, 2016]

ACKNOWLEDGEMENTS

I would like to express my deepest gratitude to my advisor, Dr. Yang Wang, for his guidance and support through my Ph.D. life at Georgia Institute of Technology. It has been a wonderful experience to work with him. He continuously encouraged and motivated me to grow as a researcher, and leader through encouraging independent thought.

I would also like to thank Dr. Tentzeris, Dr. Zhang, Dr. Suryanarayana, and Dr. Yi for being part of my thesis committee and for their time and support for my research. Dr. Yi was a senior Ph.D. student in the Laboratory of Smart Structural System (LSSS) and has been a great colleague and friend that I can always count on.

I would like to acknowledge Federal Highway Administration (FWHA) and Air Force Office of Scientific Research (AFOSR) for funding research projects.

I would like to thank Dan Li for being my research partner. I want to thank Ph.D. students in our group, Xinjun Dong and Xi Liu, for the technical assistances as well as good friendship.

Last but not least, I would like thank my parents and brother for being there every step of the way and encouraging me to complete my Ph.D. study. Their unconditional trust and love will never be forgotten.

TABLE OF CONTENTS

Page

LIST OF FIGURES

LIST OF TABLES

LIST OF SYMBOLS AND ABBREVIATIONS

f	Resonance frequency
f_{R}	Resonance frequency of the sensor
f_{R0}	Resonance frequency of the sensor at zero strain level
L	Length of the top copper cladding of the sensor
L'	Additional length due to fringe effect
β	Material permittivity
β_0	Air permittivity
β_{r}	Material relative permittivity (dielectric constant)
β_{r0}	Material relative permittivity at room temperature
β_{reff}	Material effective dielectric constant
h	Thickness of substrate
W	Width of substrate
ε	Strain
ε_i	The *i*-th strain level
$\Delta\varepsilon_i$	Difference between measured strain and strain estimated using the linear relationship at the *i*-th strain level
SHM	Structural health monitoring
UHF	Ultra high frequency
RFID	Radiofrequency identification
WISP	Wireless identification sensing platform
PTFE	Poly-tetra-fluoro-ethylene
RQI	Rayleigh quotient iteration
IPIRQ	Inverse power iteration method with Rayleigh quotient

EPC	Electronic product code
PEC	Perfect electrical conductor
PML	Perfectly matched layer
[C]	Inductance matrix
$[C^e]$	Elementary inductance matrix
[R]	Damping matrix
$[R^e]$	Elementary damping matrix
[T]	Capacitance matrix
$[T^e]$	Elementary capacitance matrix
$[\Delta A_j]$	Difference between [A] matrices at two adjacent strain steps ε_j and ε_{j+1}
$[\Delta B_j]$	Difference between [R] matrices at two adjacent strain steps ε_j and ε_{j+1}
$\{\Phi\}$	Right eigenvector
$[\Phi_{j+1}]$	Right eigenvector matrix at strain step j+1
$[\Phi_j]$	Right eigenvector matrix at strain step j
C_{ij}^e	(i, j) entry of elementary inductance matrix for element e
R_{ij}^e	(i, j) entry of elementary damping matrix for element e
T_{ij}^e	(i, j) entry of elementary capacitance matrix for element e
$\mathbf{E}$	Electric field
E_x	x component of global electric field
E_y	y component of global electric field
E_z	z component of global electric field

E_i^e	Tangential electric field along the *i*-th edge of element *e*
F	Functional
H	Magnetic field
H_x	*x* component of the magnetic field
H_y	*y* component of the magnetic field
H_z	*z* component of the magnetic field
[I]	Identity matrix
IC	Integrated circuit
j	Imaginary unit
k_0	wave number
$\mathbf{N}_i^e$	shape function of *i*-th edge of element *e*
V_a	Voltage at antenna port
I_a	Current at antenna port
[L]	Lower triangular matrix
[U]	Upper triangular matrix
$\sigma(\varepsilon)$	Stress at ε
b	Ratio of the final to initial tangent stiffness
$K_A(\varepsilon)$	Spring stiffness at ε
$G(\varepsilon)$	Tangential shear modulus of the adhesive at ε
t	Thickness of the adhesive
ν	Poisson's ratio
$E(\varepsilon)$	Tangent Young's modulus at ε
$\sigma_{\mathrm{Exp}}(\varepsilon_i)$	Stress at strain ε_i measured from the experiment

$\sigma_{\mathrm{FEM}}(\varepsilon_i, \mathbf{x})$	$\sigma_{\mathrm{FEM}}(\varepsilon_i, \mathbf{x})$ is simulated stress at strain ε_i using parameter $\mathbf{x}$
MD	Machine direction
CMD	Cross machine direction
$\mathrm{T}_{\mathrm{Exp}}(\varepsilon_i)$	Strain transfer ratio at strain step ε_i from the experiment
$\mathrm{T}_{\mathrm{FEM}}(\varepsilon_i, \mathbf{x})$	Transfer ratio at strain step ε_i from the COMSOL FE model
$V_2^{\mathrm{Out}}(f)$	V_2^{Out} is the output voltage from Port 2 at the same electromagnetic frequency as the input frequency f
$V_1^{\mathrm{Input}}(f)$	V_1^{Input} is the incident voltage from Port 1 at certain frequency f
δ_{ij}	Kronecker delta
ε_{ij}	Strain tensor
$f_{\mathrm{Exp}}(\varepsilon_i)$	Normalized resonance frequency at ε_i from an experiment
$f_{\mathrm{FEM}}(\varepsilon_i, \boldsymbol{\alpha})$	Normalized resonance frequency at ε_i from the COMSOL multi-physics simulation
$\boldsymbol{\alpha}$	Vector for electrostriction parameters
$S(\mathbf{x})$	Strain sensitivity from COMSOL
$G(\mathbf{x})$	Radiation gain generated by COMSOL
λ	Regularization parameter
P	Interrogation power level; Power transmitted back to the reader from the frequency doubling sensor
P_0	Incident power received at the frequency doubling sensor
P_1	Power transmitted from 2.4GHz antenna to the matching network
P_2	Power transmitted from the matching network to the 4.8GHz antenna
R^2	Coefficient of determination

s	Matrix scaling factor
S_{11}	Reflection coefficient
S_{11}^{R}	Reflection coefficient of the 2.4GHz receiving antenna
S_{11}^{T}	Reflection coefficient of the 4.8GHz transmitting antenna
G_c	Gain conversion
μ	Permeability
μ_0	Air permeability
μ_r	Relative permeability
$\tilde{\omega}$	Angular frequency

SUMMARY

This dissertation develops passive (battery-free) wireless strain sensing techniques for low-cost structural health monitoring (SHM). Passive wireless strain sensing has obvious advantages among SHM technologies because the sensors require neither cable nor external power supply for operation. However, current numerical approaches for modeling and designing passive antenna sensors are oftentimes inefficient and inaccurate. In this study, a partially air-filled cavity modeling and an inverse power iteration method with Rayleigh quotient (IPIRQ) are proposed to significantly improve computational speed of strain sensing simulation. Optimization frameworks are proposed for identifying accurate mechanical and electromagnetic parameter values of an antenna sensor through finite element model updating using experimental measurements. In addition, a multi-objective optimization approach is formulated to maximize sensor performance such as strain sensitivity and antenna gain. Finally, in order to overcome the limit of radiofrequency identification (RFID) antenna sensors, a frequency doubling technology is investigated. To achieve close deployment of multiple frequency doubling antenna sensors, a wireless switching mechanism is designed and implemented. Performance of the frequency doubling antenna sensors with wireless switching is experimentally validated.

CHAPTER 1 INTRODUCTION

In this chapter, Section 1.1 introduces the background and motivation of this research. Section 1.2 discusses research purpose and objective. Finally, Section 1.3 presents the organization of this dissertation.

1.1 Background and Motivation

In order to accurately monitor the safety condition of a structure, various sensors can be deployed on the structure to measure structural responses and operating conditions, such as strain, displacement, acceleration, humidity, temperature, etc. [1]. Among various measurands needed for structural health monitoring (SHM), strain is the one of the most important indicators of stress concentration and damage development. Many types of sensors can measure strain, such as metal foil strain gages, vibrating wire sensors, and fiber optic sensors [2]. Although the performance of these sensors is adequate in many applications, most of the sensors require a cabled system for data acquisition and power supply. However, cabled systems can be costly not only in system installation, but also in long-term system maintenance [3]. Therefore, passive radiofrequency identification (RFID) antenna sensors have been developed to monitor strain concentration and crack propagation in structures [4-6]. Because these antenna sensors are bonded on the structural surface, sensors deform together with the structure. As a result, the length of antenna sensors changes with structural deformation, which causes the electromagnetic resonance frequency change of the sensors. Therefore, the relationship between resonance frequency and strain can be used for strain measurement. However, since antenna sensors have been manually designed by experience, performances of strain sensing and interrogation distance are not maximized [4-7]. Therefore, in order to automatically optimize sensor performance, a systematic approach for automatically sensor design is needed to study.

Literature review of relevant research topics is provided in the following three subsections. Section 1.1.1 first reviews conventional wireless technologies for structural health monitoring. Section 1.1.2 introduces the state of the art in passive wireless antenna sensors. Section 1.1.3 briefly discusses multi-physics coupled simulation techniques for antenna sensor designs. In order to reduce computing time of simulation, eigenfrequency solution and FE modeling techniques are also proposed.

1.1.1 Conventional Wireless Sensing Technologies for Structural Health Monitoring (SHM)

For a few decades, cost-effective wireless sensor nodes have been developed in order to save SHM system installation and costs [8-10]. An extensive review on wireless sensing for SHM can be found in Lynch and Loh [11], which summarizes various academic and industrial wireless sensing technologies. A typical wireless sensor node mainly has three functional modules: sensing interface (converting analog sensor signal to digital data), computing core (data storage and processing), and wireless transceiver (digital communication with peers or a wireless gateway server). For example, measurement of strain or acceleration is achieved by interfacing the wireless node with a metal foil strain gage or an accelerometer.

Past wireless sensors usually rely on external power such as batteries for operation. In order to avoid battery replacement in the field, rechargeable batteries are often deployed and charged by an integrated energy harvester. Typical sources for energy harvesting include solar energy, wind, mechanical vibration, and thermal gradients, *etc*. [12]. However, a reliable energy source may not be available in the field, e.g. solar energy is highly limited in shaded area or inside a box girder. Secondly, even with a reliable source for energy harvesting, rechargeable batteries usually have a limited life span. In order to address issues associated with the dependency on battery power, passive (battery-free) wireless sensors have been proposed [13]. For example, a WISP (wireless

interrogation and sensing platform) node is wirelessly charged by a reader signal [14]. However, operation of the WISP node follows the conventional wireless sensing approaches with the three functional modules described in [11]. Although conventional wireless SHM systems reduce system installation and costs, long-term field monitoring is limited to requirement of external power supply.

1.1.2 Passive Wireless Sensors

A passive wireless sensor can operate without external power supply such as batteries [13]. There are two main categories of passive sensing technologies. The first one utilizes a resonating circuit consisting of inductors, capacitors, and resistors for strain measurement [15-17]. Once mechanical strain is applied to the resonating circuit, impedance changes, which cause change to resonance frequency eventually. In this method, the interrogation is achieved by inductive coupling. Therefore, the wireless interrogation distance is usually limited to a few inches, which is inconvenient for practical applications. On the other hand, the second method characterizes far-field antenna property changes, including resonance frequency, power spectrum, and return loss [18-20]. For example, when an antenna experiences deformation, the antenna shape changes, causing shift in electromagnetic resonance frequency of the antenna. Yi *et al* [4, 5] proposed passive (battery-free) RFID (radiofrequency identification) antennas for wireless strain measurement, using signal modulation by an economic RFID chip (costing about $0.10). Utilizing far-field effect, the RFID patch antenna sensors achieved longer interrogation distances (demonstrated to be 2m) and showed promising performance for wireless strain/crack sensing. Later on, a frequency doubling technique has been introduced as an alternative way of signal modulation [21]. By doubling the backscattered signal frequency, unwanted environmental reflections are removed. In addition, higher operating frequencies (compared with ~900 MHz RFID) can enable sensor size reduction and strain sensitivity improvement. However, previous work on

frequency doubling antenna sensor could not distinguish two or more sensors installed next to each other.

1.1.3 Simulation Techniques for Antenna Sensors

Numerical simulation techniques for antenna design have been developed for several decades. Antenna simulation methods mainly include finite difference time domain (FDTD) method [22, 23], multiresolution time-domain method (MRTD) [24], finite element method (FEM) [25, 26], finite integration technique (FIT) [27], and method of moment (MOM) [28, 29]. Antenna sensor design and its performance prediction are usually achieved using commercial software packages specialized in electromagnetics, such as HFSS (High Frequency Structural Simulator), CST (Computer Simulation Technology), ADS (Advanced Design System), *etc*. However, these software packages are specialized in solving only electromagnetic problems and cannot add other simulation of physical domains (such as mechanics required for antenna sensor simulation under strain effect). In order to accurately describe antenna sensor behavior involving mechanics and electromagnetics, multi-physics coupled simulation is necessary Two popular commercial multi-physics coupled simulation software packages are COMSOL Multiphysics [30] and ANSYS [31]. In this research, coupling mechanics and electromagnetics simulation is performed using COMSOL.

In past research, a frequency domain solver is usually used to identify the resonance frequency under strain [7]. The solver calculates antenna scattering parameter (S_{11}), antenna gain, and surface currents in a given frequency range. The resonance frequency is determined as the peak of frequency in the S_{11} curve. The frequency domain process requires high computational load to identify the resonance frequency of an antenna sensor under every strain level being simulated. Design optimization of antenna sensors requires resonance frequency simulation of different antenna geometry at many strain levels, which makes frequency domain solver inefficient.

In order to improve simulation efficiency of antenna sensors, eigenvalue perturbation methods were proposed by Yi [32]. Since the eigenfrequency at the 1st resonating antenna mode is resonance frequency of an antenna, eigenfrequency solution directly finds resonance frequency in strain sensing simulation. After formulating eigenvalue problem, a first-order eigenvalue perturbation method [33, 34] and the Rayleigh quotient iteration [35] were used to determine eigenvalue and eigenvector results from previous strain step to improve solution efficiency. In this thesis, cavity and partially air-filled cavity FE modeling techniques are proposed to further improve the simulation efficiency by reducing the number of degrees-of-freedom (DOFs). In addition, the inverse iterative power method with Rayleigh quotient (IPIRQ) is suggested to further speed up the eigenfrequency computation.

In summary, study of antenna sensors should include two physical domains, mechanics and electromagnetics, in order to maximize sensor performance. However, current numerical simulation techniques for antenna sensor design are inefficient due to their focus on electromagnetic problems. In this thesis, an efficient method for strain sensing simulation is proposed.

1.2 Purpose and Objective

The main research objective of this thesis is to develop an optimization framework for designing wireless strain/crack antenna sensors. The objective is achieved by addressing following tasks.

1. To improve the simulation efficiency, new FE modeling techniques for electromagnetic simulation are proposed. The current modeling method (full-wave modeling) is appropriate for the frequency domain solver. However, for an eigenfrequency solver, it is not necessary to build a large volume of simulation domain. A proposed cavity model or a partially air-filled cavity model reduces the number of DOFs by reducing the size of air domain. In

addition, the inverse power iteration method with Rayleigh quotient (IPIRQ) improves the efficiency of the simulation time while maintaining the similar accuracy as previously used solvers.

2. To improve the modeling accuracy, model updating for material parameters, such as constitutive relations (mechanical parameter) and dielectric constant (electromagnetic parameter), is conducted. Previous models used nominal parameter values and thus easily result in discrepancy between simulation and experiment. In this thesis, strain dependent mechanical and electromagnetic model parameters are updated based on experimental results. Mathematical optimization problems are formulated for model updating. Updated parameter values are implemented into the FE model, achieving higher simulation accuracy.

3. To find the optimal design of antenna sensors, a systematic optimization framework is proposed to maximize the strain sensing performance of antenna sensors. Although promising performance of patch antenna sensors has been demonstrated by both simulation and experimental results, the sensor design was manually optimized by experience. A more systematic framework is proposed for automatically optimizing sensor performance such as strain sensitivity, using COMSOL Livelink that allows interface with MATLAB optimization toolbox. For validation of the optimal design, extensive experiments are conducted.

4. To develop an alternative signal modulation approach, a frequency doubling technology has been implemented in antenna sensors. As described previously, the frequency doubling antenna sensor cannot distinguish two or more sensors which are deployed in close proximity. Therefore, a wireless switching mechanism is proposed for sensor array operation. The switching mechanism

utilizes the forward biasing voltage of the Schottky diode in the sensor, which is the key component that enables frequency doubling.

1.3 Organization of Dissertation

The rest of this dissertation is organized as follows.

CHAPTER 2 introduces strain/crack sensing mechanisms of two types of antenna sensors, an RFID antenna sensor and a frequency doubling antenna sensor. The sensing mechanisms describe how mechanical responses such as strain and crack are converted into electromagnetic signals to enable wireless measurements.

CHAPTER 3 proposes several techniques for improving efficiency of multi-physics simulation of antenna strain sensors. First, the finite element formulation for electromagnetics is introduced and two different solutions (frequency domain and eigenfrequency solutions) are compared. To improve the simulation efficiency of the eigenfrequency solution, two new modeling techniques, cavity modeling and partially air-filled cavity modeling, are proposed. Furthermore, two eigenvalue perturbation techniques, Rayleigh quotient iteration method (RQI) and inverse power iteration method with Rayleigh quotient (IPIRQ), are studied. Finally, the proposed methods are validated by an example model of a 2.9GHz patch antenna.

CHAPTER 4 proposes model updating methods for both mechanical and electromagnetic parameters to improve accuracy of antenna-sensor simulation. For mechanical model updating, a phenomenological model is studied first and constitutive relationships of three materials (aluminum, copper, and substrate) are updated based on the experimental results. The three updated constitutive relationships are implemented into a mechanical FE model, to finally update adhesive shear modulus using experimental strain transfer ratios. Furthermore, the change of dielectric constant value under strain effect is updated in the electromagnetic domain. Based on all model updating results, an accurate multi-physics FE model can be obtained.

CHAPTER 5 proposes a design optimization framework of the antenna sensor. Two objectives, strain sensitivity and radiation gain, are formulated. Using an example sensor model, the optimized sensor design is fabricated, and validated through extensive experiments.

CHAPTER 6 presents the design, simulation, and validation experiments of a frequency doubling antenna sensor. Adopting a discrete component matching method, the sensor has more flexible frequency range. Therefore, the resonance frequency is tunable to compensate fabrication imperfection and environmental effect. Furthermore, a wireless switching mechanism for frequency doubling antenna sensor is proposed. Experimental validation is also included.

CHAPTER 7 presents a summary of the research and the primary conclusions. Future research topics are recommended.

CHAPTER 2 Wireless Strain Sensing Mechanisms for Antenna Sensors

In order to achieve passive wireless strain sensing, antenna sensors characterize antenna property changes such as resonance frequency which is measured and used as the damage indicators [18-20]. When an antenna experiences deformation, the antenna shape changes, causing shift in electromagnetic resonance frequency of the antenna. Because passive system operation relies on electromagnetic backscattering at low power, it is difficult to distinguish the sensor signal from environmental reflections. In addition, the interrogation distance would be limited to a few inches without proper signal modulation.

In this chapter, a conceptual idea of a passive RFID slotted patch antenna sensor is first introduced. Through signal modulation by an economic RFID chip (costing about $0.10), patch antennas can achieve longer interrogation distances and demonstrate promising performance for wireless strain/crack sensing. The RFID slotted patch antenna sensor utilizes antenna folding technique using vias and slots on the antenna structure, in order to reduce antenna size. Therefore, the slotted patch antenna reduces the size to a quarter of a normal patch antenna, while maintaining the RFID operation frequency at around 915MHz.

As an alternative way of signal modulation, a frequency doubling technique is introduced to improve strain sensitivity and to reduce sensor size while removing unwanted environmental reflections by doubling the backscattered signal frequency. The frequency doubling antenna sensor consists of three main components — a 2.9GHz receiving patch antenna, a matching network, and a 5.8GHz transmitting patch antenna. For interrogation, a wireless reader emits a 2.9GHz interrogation signal to the 2.9GHz receiving patch antenna of the antenna sensor. The matching network integrated with a Schottky diode then doubles the interrogation frequency of 2.9GHz to the backscattering frequency of 5.8GHz. The 5.8GHz transmitting patch antenna finally responds with the backscattered signal to the reader.

This chapter introduces strain sensing mechanism of both the RFID slotted patch antenna and the frequency doubling antenna sensor. Section 2.1 presents the strain/crack sensing mechanism of the slotted patch antenna sensor including RIFD reader and sensor system. Section 2.2 describes the frequency doubling technique for wireless strain/crack measurement.

2.1 RFID Antenna Sensors

RFID patch antenna sensors can achieve wireless strain and crack sensing by its detecting resonance frequency change. Once an antenna sensor is bonded on a structural surface for strain measurement, the sensor deforms together with the structure. As a result, the antenna length changes with structural deformation. Eq. (2.1) shows that resonance frequency of a regular patch antenna , $f_{\mathrm{R0}}^{\mathrm{Patch}}$, is related to antenna length [36]:

$$f_{\mathrm{R0}}^{\mathrm{Patch}} = \frac{c}{2(L + L')\sqrt{\beta_{\mathrm{reff}}}} \tag{2.1}$$

where c is the speed of the light, L is the physical length of the copper cladding on the antenna, β_{reff} is the effective dielectric constant of the antenna substrate, and L' is the additional electrical length due to fringing effect. Because the thickness-to-width ratio of a patch antenna is much smaller than one, the effective dielectric constant β_{reff} has approximately the same value as the dielectric constant β_{r0} [36] :

$$\beta_{\mathrm{reff}} = \frac{\beta_{\mathrm{r0}} + 1}{2} + \frac{\beta_{\mathrm{r0}} - 1}{2}\left[1 + 12\frac{h}{W}\right]^{-1/2} \cong \beta_{\mathrm{r0}} \tag{2.2}$$

where h and W are thickness and width of the substrate, respectively; β_{r0} is the relative dielectric constant of the substrate at room temperature without any deformation.

When the antenna is deformed or cracked as shown in Fig. 2.1 (a) and (b), the length of electrical path is changed. When strain ε occurs in the longitudinal direction, the resonance frequency is shifted to:

$$f_{\mathrm{R}}^{\mathrm{Patch}} = \frac{c}{2(1+\varepsilon)(L+L')\sqrt{\beta_{r0}}} = \frac{f_{\mathrm{R0}}^{\mathrm{Patch}}}{1+\varepsilon} \tag{2.3}$$

If the applied strain ε is small (usually less than a few thousand micro-strains), the resonance frequency of the sensor changes approximately linearly with respect to strain:

$$\begin{aligned} f_{\mathrm{R}}^{\mathrm{Patch}} &= f_{\mathrm{R0}}^{\mathrm{Patch}}(1-\varepsilon+\varepsilon^2-\varepsilon^3+\varepsilon^4-\varepsilon^5+\cdots) \\ &\cong f_{\mathrm{R0}}^{\mathrm{Patch}}(1-\varepsilon) \end{aligned} \tag{2.4}$$

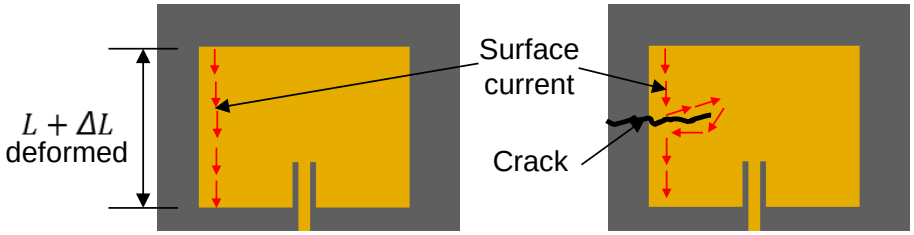

(a) Strain sensing (b) Crack sensing

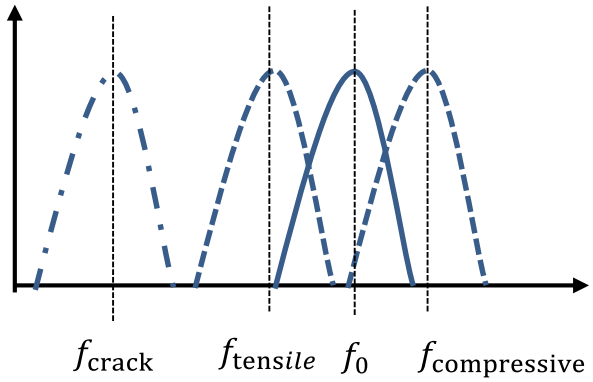

(c) Frequency change by crack and strain

Fig. 2.1. Strain/Crack simulation mechanism of a patch antenna sensor

This linear relationship indicates that strain can be derived by measuring shift in the antenna resonance frequency. This serves as the fundamental strain sensing mechanism of the wireless antenna sensor. Fig. 2.1 (a) and (b) illustrate the relationship between sensor deformation or crack development and antenna resonance frequency. When strain ε is positive, the current path is elongated. Therefore, the resonance

frequency f decreases according to Eq. (2.4) . On the other hand, if strain ε is negative, the resonance frequency f increases (Fig. 2.1 (c)). In addition, when a crack is propagated into the antenna sensor, the surface current is detoured and the current path also becomes longer, reducing resonance frequency.

The operating frequency range of the commercial RFID chip (SL3ICS1002 model manufactured by NXP Semiconductor) is around 900MHz. To utilize the RFID chip for signal modulation, the designed resonance frequency of the antenna sensor should also be around 900MHz. According to Eq. (2.1), the length of the antenna sensor needs to be over 130mm, which is undesired in many engineering applications. To achieve size reduction, the slotted patch antenna design is shown in Fig. 2.2 [7, 37]. Vias go through substrate and connect top copper cladding with bottom copper (ground plane) to increase electrical length travelled by the current. Two slots are added on the top copper cladding to further detour surface current path. The initial resonance frequency of the slotted patch antenna sensor can be estimated as:

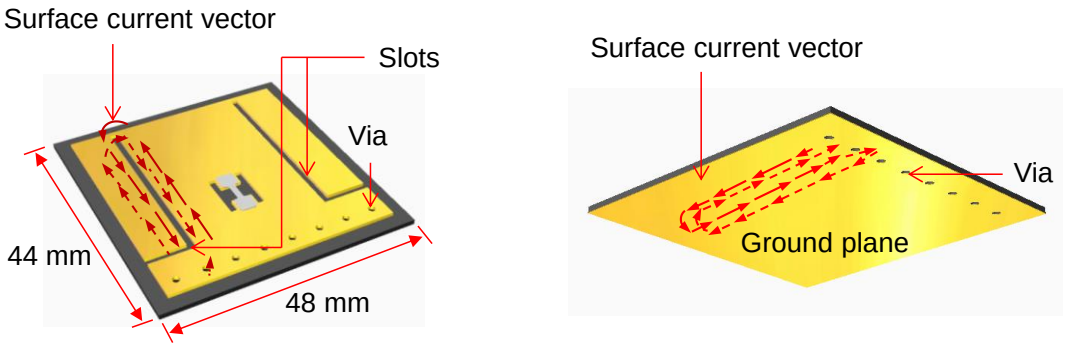

(a) Top skewed view (b) Bottom skewed view

Fig. 2.2. Illustration of the surface current flows in the slotted patch antenna

$$f_{\mathrm{R0}}^{\mathrm{Slotted}} = \frac{c}{8(L+L')\sqrt{\beta_{\mathrm{reff}}}} \tag{2.5}$$

The shifted resonance frequency under strain is:

$$f_{\mathrm{R}}^{\mathrm{Patch}} = \frac{c}{8(1+\varepsilon)(L+L')\sqrt{\beta_{r0}}} = \frac{f_{\mathrm{R0}}^{\mathrm{Patch}}}{1+\varepsilon} \tag{2.6}$$

This approximately linear relationship indicates that the applied strain can be derived by measuring the antenna resonance frequency shift.

Fig. 2.3 illustrates wireless backscattering measurement in the RFID system. The RFID slotted patch antenna sensor is composed of the patch antenna and the RFID chip The Tagformance Lite unit from Voyantic Ltd. is used as the RFID reader [38]. The antenna sensor receives power from the reader when the sensor is within the interrogation range. Part of the captured power is harvested by the RFID chip. If the harvested power is higher than the turn-on power of the chip (32μW), the sensor is activated. The RFID chip modulates a response signal, and transmits the modulated signal back to the reader. Finally, the reader demodulates the response signal to distinguish the sensor response from the reflection by surrounding environment.

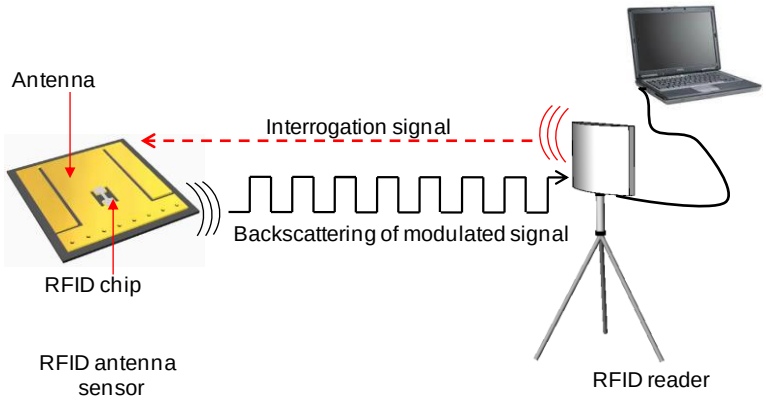

Fig. 2.3. Wireless communication in a passive RFID system

The system is passive (battery-free) since the sensor operates on the harvested interrogation power from the reader, i.e. the sensor does not require power sources such as batteries or solar energy harvesting. The passive RFID chip conforms with EPC Class-

1 Generation-2 UHF RFID Protocol and operates in the limited frequency range between 860 MHz and 960 MHz [39].

2.2 Frequency Doubling Antenna Sensor

A frequency doubling antenna sensor operates different from an RFID sensor. The frequency doubling antenna sensor consists of three main components, i.e., a receiving antenna (with resonance frequency f_{R0}), a transmitting antenna (with doubled resonance frequency $2f_{\mathrm{R0}}$), and a diode-integrated matching network between receiving and transmitting antennas. Fig. 2.4 illustrates the operation mechanism of a frequency doubling sensor. During operation, a wireless interrogation signal is emitted from the reader side through a transmitting reader antenna. If interrogation frequency f is in the neighborhood of f_{R0}(resonance frequency of the receiving patch antenna at sensor side), interrogation power is captured by the sensor-side receiving patch antenna and transferred to the matching network. Due to nonlinear behavior of the diode, the output signal from the diode has significant amplitude at harmonics (multiples) of the incident frequency.

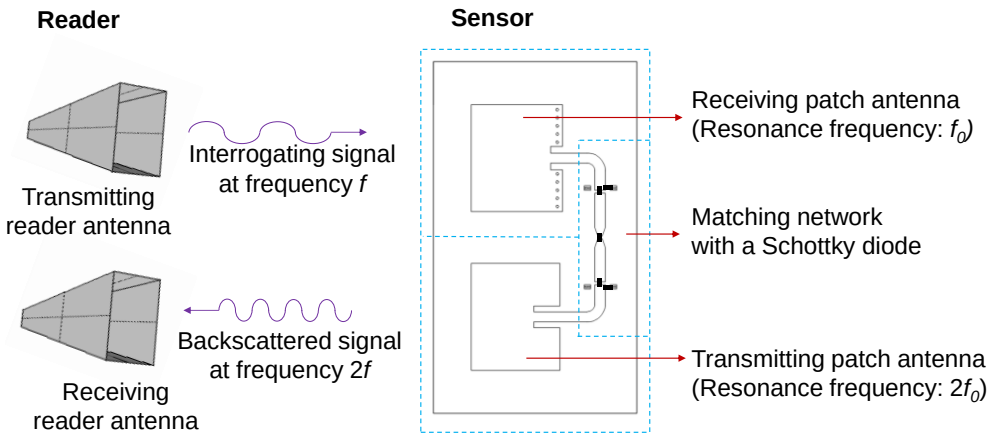

Fig. 2.4. Operation mechanism of a passive frequency doubling device

In this application, the second harmonic ($2f$) of the incident frequency is utilized for measurement by the reader. The output signal at $2f$ is backscattered to the reader

through sensor-side transmitting patch antenna (resonance frequency at $2f_{R0}$). Because the unwanted environmental reflections to original reader interrogation signal remains at f, it is easy for the reader to distinguish backscattered sensor signal from unwanted environmental reflections.

2.3 Summary

This chapter presents strain and crack sensing mechanisms of the RFID antenna sensor and the frequency doubling antenna sensor. Antenna sensor deformation on a monitored structural surface causes electromagnetic resonance frequency change. For wireless interrogation, two signal modulation methods (RFID and frequency doubling) are introduced. In the RFID system, the reader distinguishes the sensor response by the demodulated signal. In the frequency doubling system, the response signal is two times of the input frequency. Therefore, the reader can distinguish the sensor signal from environmental reflection.

CHAPTER 3 IMPROVING EFFICIENCY OF MULTI-PHYSICS SIMULATION FOR ANTENNA STRAIN SENSORS

To simulate the behavior of a passive antenna strain sensor, current multi-physics coupled simulation (between mechanics and electromagnetics) has mainly adopted the frequency domain solution. For every frequency point in the sweeping range, the frequency domain solver computes the value of scattering parameter S_{11}. The S_{11} curve is used to identify the new resonance frequency when the antenna sensor is at certain strain level. As a result, the frequency domain solution is computationally expensive. In this study, an eigenfrequency solution, whose efficiency is shown to be much higher than the frequency domain solver, is proposed to directly detect changes of antenna resonance frequency under strain. Towards the eigenfrequency solution, cavity and partially air-filled cavity FEM modeling techniques are proposed to reduce the number of degrees of freedom. In addition, by formulating the eigenfrequency solution as an eigenvalue perturbation problem, Rayleigh quotient iteration (RQI) and the inverse power iteration method with Rayleigh quotient (IPIRQ) are proposed to further improve the computational efficiency. The proposed methods greatly improve the efficiency of antenna sensor designs.

The rest of this chapter is organized as follows. Section 3.1 presents the finite element formulation for modeling the electromagnetic behavior of the antenna sensor. Frequency domain and eigenfrequency solutions are compared. Section 3.2 proposes novel modeling techniques for eigenfrequency solution. To improve the computing speed of the antenna sensor simulation, cavity and partially air-filled cavity models are proposed and pros and cons of these models are investigated. Section 3.3 suggests two eigenfrequency solvers, RQI and IPIRQ to improve computing speed for antenna sensor simulation. Section 3.4 validates performances of the proposed air-filled cavity model and the IPIRQ eigenvalue perturbation method through an example of a 2.9GHz patch antenna. The results are summarized and discussed in Section 3.5.

3.1 Finite Element Formulation of the Eigenvalue Problem

This section describes the finite element formulation and its eigenfrequency solution of antenna sensor, which is organized based on work from Yi [32] and contains excerpts. Section 3.1.1 introduces the basic finite element formulation in electromagnetic problems. Section 3.1.2 and Section 3.1.3 present frequency domain and eigenfrequency solutions, respectively. Section 3.1.4 compares the simulation efficiency of the eigenfrequency solution and the frequency domain solution with an example FEM model of a 2.9GHz antenna.

3.1.1 Finite Element Formulation

For simulating an antenna strain/crack sensor, Fig. 3.1 illustrates the domains including the sensor, an air sphere, and PML. An antenna sensor usually includes a metallic surface and a dielectric substrate, which is used to separate the antenna metallic surface from the surface of the structure being monitored. The metallic surface is usually modeled as PEC materials. The boundary of the metallic surface is denoted as S_{PEC}, whose direction is $\hat{n}$. The volume of the dielectric substrate is denoted as V_d and the substrate relative permittivity and permeability are μ_r and β_r, respectively. The entire antenna sensor is placed inside an air sphere, whose permittivity and permeability are μ_0 and β_0, respectively. Since a resonant antenna model is an open structure that has no definite physical boundaries, it is necessary to set termination boundaries so that the simulation domain is finite. The combination of PML and PEC is adopted in the 3D electromagnetic simulation.

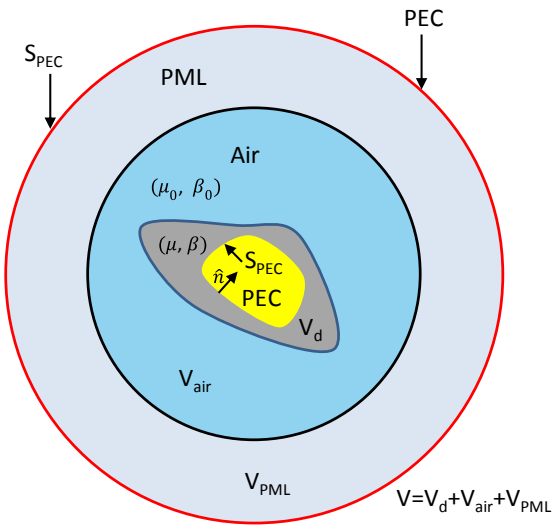

Fig. 3.1. Inhomogeneous structure enclosed by termination boundaries

The Maxwell's equations in an inhomogeneous material have the general vector form [25, 40]:

$$\begin{aligned} \nabla \times \mathbf{E} &= -j\omega\mu\mathbf{E} \\ \nabla \times \mathbf{H} &= -j\omega\beta\mathbf{H} + \mathbf{J} \\ \nabla \cdot (\beta\mathbf{E}) &= 0 \\ \nabla \cdot (\mu\mathbf{E}) &= 0 \end{aligned} \tag{3.1}$$

where $\mathbf{E} = E_x\hat{\mathrm{x}} + E_y\hat{\mathrm{y}} + E_z\hat{\mathrm{z}}$ is the electric field; $\mathbf{H} = H_x\hat{\mathrm{x}} + H_y\hat{\mathrm{y}} + H_z\hat{z}$ is the magnetic field; $\mathbf{J}$ is the current vector; μ and β are the permeability and permittivity of the material, respectively; ω is the angular frequency; ∇ is a standard differential operator in Cartesian coordinates:

$$\nabla = \hat{\mathrm{x}}\frac{\partial}{\partial \mathrm{x}} + \hat{\mathrm{y}}\frac{\partial}{\partial \mathrm{y}} + \hat{\mathrm{z}}\frac{\partial}{\partial \mathrm{z}} \tag{3.2}$$

According to Ritz method, a functional for the total electric field can be expressed through a volume integral after considering boundary conditions of the simulation model [26, 41, 42]:

$$\boldsymbol{F} = \int_V \left[\frac{1}{\mu}(\nabla \times \mathbf{E}) \cdot (\nabla \times \mathbf{E}) + (j\tilde{\omega})^2 \beta \mathbf{E} \cdot \mathbf{E}\right] dv + + \int_{S_0} [\mathbf{E} \cdot (\hat{n} \times \nabla \times \mathbf{E})]\, dS + \int_V \mathbf{E} \cdot \mathbf{f}\, dv \tag{3.3}$$

where μ_0 (=$4\pi\times10^{-7}$ N/A^2) is the air permeability; ω is angular frequency; S_0 denotes the surfaces within volume V for which the tangential component of electric field **E** and/or magnetic field **H** is discontinuous; **f** denotes the sources in the model. In finite element method, the entire solution domain is discretized into a finite number of elements. Each element occupies a separate volume V^e (e = 1, 2, …, N_T), where N_T is the total number of elements. The electric field can then be denoted in a vector form in terms of the polynomial basis functions $\mathbf{N}_i^e$ over a general m-edge finite element [25]:

$$\mathbf{E}^e = \sum_{i=1}^{m} E_i^e \mathbf{N}_i^e \tag{3.4}$$

where $\mathbf{N}_i^e$ is the i-th edge based vector basis function of element e; m is the total edge number of one element; E_i^e is the tangential electric field along the i-th edge of element e. Substituting Eq. (3.4) into Eq. (3.3), integrating over the volume of one element, and deriving according to variational principle, the following equation can be obtained [26]:

$$(j\omega)^2 \sum_{e=1}^{N_T} [T^e]\{E^e\} + (j\omega) \sum_{e=1}^{N_T} [R^e]\{E^e\} + \sum_{e=1}^{N_T} [C^e]\{E^e\} = \sum_{e=1}^{N_T} \{\mathrm{f}^e\} \tag{3.5}$$

where $[C^e]$, $[R^e]$and $[T^e]$ are elementary inductance, resistance and capacitance matrices, respectively; f^e is the source term due to incident voltage or current excitation at the port. The entries of the matrix, $[C^e]$, $[R^e]$and $[T^e]$ are given by

$$C_{ij}^{e} = \int_{V^e} \frac{1}{\mu} (\nabla \times \mathbf{N}_i^e) \cdot \left(\nabla \times \mathbf{N}_j^e\right) dv$$

$$R_{ij}^{e} = \mu_0 \left[\int_{S^e} \mathbf{N}_i^e \cdot (\hat{n} \times \mathbf{H}) dS \right] \tag{3.6}$$

$$T_{ij}^{e} = \int_{V^e} \beta \mathbf{N}_i^e \cdot \mathbf{N}_j^e dv$$

where V^e is the volume of element *e*; S^e is the boundary of element *e*.

3.1.2 Frequency Domain Solution

An incident electromagnetic wave is propagated by voltage or current excitation at the feeding port from source $\{f^e\}$ as shown in Eq. (3.5). Electric and magnetic fields are calculated based on $[C^e]$, $[R^e]$and $[T^e]$ matrices with voltage or current excitation. From Maxwell's equation, electric and magnetic field distributions are calculated:

$$\mathbf{E} = \frac{1}{j\omega\mu_0} \nabla \times \mathbf{H} \tag{3.7}$$

$$\mathbf{H} = \frac{1}{-j\omega\mu_0} \nabla \times \mathbf{E} \tag{3.8}$$

Based on the computed electric and magnetic field distributions, voltage and current at the port of an FEM antenna model are calculated [43]:

$$V_a = \int_1^2 \vec{E} \cdot \overrightarrow{dl} \tag{3.9}$$

$$I_a = \int_c \vec{H} \cdot \overrightarrow{dl} \tag{3.10}$$

where 1 and 2 are starting and ending feeding points of the antenna; *C* is the cross-sectional contour of the antenna feeds. The antenna impedance can be simply defined as:

$$Z_a = \frac{V_a}{I_a} \tag{3.11}$$

Once the antenna impedance is known according to the field distributions, the scattering parameter S_{11} between the port and the antenna is calculated as [43]:

$$S_{11}(f) = \frac{Z_a(f) - Z_p(f)}{Z_a(f) + Z_p(f)} \tag{3.12}$$

where Z_p is the impedance of the feeding port, which equals to the IC chip impedance in the antenna sensor simulation, but standard port impedance is commonly 50 Ω such as patch antenna simulation for frequency doubling antenna sensors; f is operating frequency.

3.1.3 Eigenfrequency Solution

If no excitation is considered, the source term $\{f^e\}$ in Eq. (3.5) vanishes. The equation can be rewritten as [25] with simplification:

$$\lambda^2[T]\{E\} + \lambda[R]\{E\} + [C]\{E\} = \{0\} \tag{3.13}$$

where λ is eigenvalue; [C] is named as inductance matrix; [T] is named as capacitance matrix, while [R] is the damping matrix. The final formulation in Eq. (3.13) ends up as a quadratic eigenvalue problem [41, 44]. Using N to denote the total number of degrees of freedom in Eq. (3.13), [C] and [R] are N × N complex symmetric matrices, while [T] is an N × N real symmetric matrix. Since the entry T_{ij}^e in Eq. (3.6) includes material permittivity β, which is a small number on the order of 10^{-12}, the magnitudes of T_{ij}^e as well as entries in global matrix [T] are small. The entry R_{ij}^e in Eq. (3.6) is also small due to small magnitude of μ_0. With small-magnitude entries in [R] and [T], the matrices are usually ill-conditioned. To improve the condition number of the two matrices, scaling can be performed. To this end, Eq. (3.13) is reformulated as:

$$\tilde{\lambda}^2[\mathrm{T}^s]\{\mathrm{E}\} + \tilde{\lambda}[\mathrm{R}^s]\{\mathrm{E}\} + [\mathrm{C}]\{\mathrm{E}\} = \{0\} \tag{3.14}$$

where

$$[\mathrm{R}^s] = \sqrt{s}[\mathrm{R}]; \quad [\mathrm{T}^s] = s[\mathrm{T}]; \quad \tilde{\lambda} = \lambda/\sqrt{s}; \tag{3.15}$$

Here s is the scaling factor.

State-space formulation equivalently converts Eq. (3.14) into a generalized eigenvalue problem:

$$[\mathrm{A}]\{\Phi\} = \tilde{\lambda}[\mathrm{B}]\{\Phi\} \tag{3.16}$$

where

$$[\mathrm{A}] = \begin{bmatrix} -[\mathrm{C}] & [0] \\ [0] & [\mathrm{T}^s] \end{bmatrix}, [\mathrm{B}] = \begin{bmatrix} [\mathrm{R}^s] & [\mathrm{T}^s] \\ [\mathrm{T}^s] & [0] \end{bmatrix}, \{\Phi\} = \begin{Bmatrix} \{\mathrm{E}\} \\ \tilde{\lambda}\{\mathrm{E}\} \end{Bmatrix} \tag{3.17}$$

Here [I] is an N×N identity matrix and [0] is an N×N zero matrix.

The eigenvalue $\tilde{\lambda}$ is closely related with resonance frequency of the antenna sensor f_R according to the following equation:

$$\tilde{\lambda} = \frac{\mathrm{j}\tilde{\omega}}{\sqrt{s}} = \frac{\mathrm{j}\omega - \alpha}{\sqrt{s}} = \frac{\mathrm{j}2\pi f_\mathrm{R} - \alpha}{\sqrt{s}} \tag{3.18}$$

The resonance frequency f_R is a key parameter determining the strain effects of the antenna sensor. Associated with every eigenvalue $\tilde{\lambda}$, eigenvector $\{\Phi\}$ represents the electric field distribution of each eigenmode. The plot of $\{\mathrm{E}\}$ field is an intuitive way to check the correctness of the antenna mode. Furthermore, the quality factor (Q) of the antenna sensor can be defined as [25]:

$$Q = \left|\frac{\omega}{2\alpha}\right| \tag{3.19}$$

If the calculated eigenmode is an antenna mode, a large Q is expected. Otherwise, Q is smaller due to large decay rate α caused by the boundary conditions. Therefore, Q is another indicator to distinguish antenna mode and spurious mode.

3.1.4 Solution Example for Comparing the Solvers

In order to compare performances of two solutions for strain sensing simulation, i.e. the eigenfrequency solution and the frequency domain solution, a 2.9GHz patch antenna is modeled as an example using the commercial multi-physics software package COMSOL (Fig. 3.2).

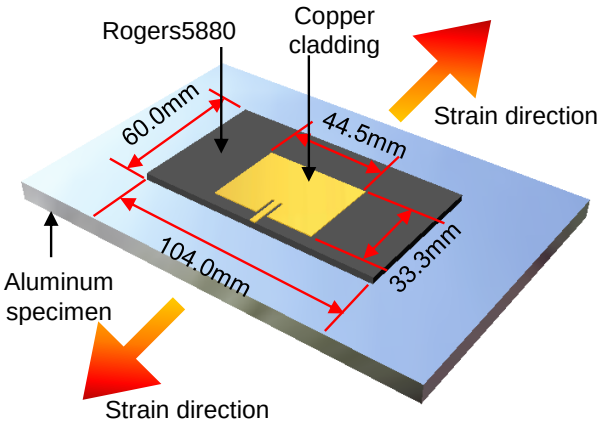

Fig. 3.2. Illustration of the 2.9GHz patch antenna on the aluminum plate

The substrate material of the example model is Rogers RT/duriod®5880 with dielectric constant ($\varepsilon_r = 2.2$) and low loss tangent of 0.0009. The thickness of the substrate is 0.7874mm and the planar dimension of the 2.9GHz patch antenna is 44.5mm × 33.3mm. The antenna is mounted on an aluminum specimen. Strain is applied to the two ends of the aluminum specimen. The 3D full-wave electromagnetic simulation setup of the 2.9GHz model for COMSOL is presented in Fig. 3.3(a). PEC boundaries are assigned to the outside of the air sphere, the patch, and the ground plane. The PML boundary is also combined with the PEC at the air sphere. The total number of degrees of freedom (DOFs) is 259,975. Simulations are conducted on a desktop with Intel® Xeon® processor E5-1620V3 (four cores, 3.5GHz) and 16 GB RAM memory.

At first, the frequency domain solver simulates a scattering parameter S_{11} plot (Fig. 3.3(b)). This is an indicator of the antenna radiation performance in the sweeping frequency ranges at different strain levels from zero to 2,000με, with 500με strain increase per step. The computation of S_{11} curve at each strain level is performed for 51 frequency points, consuming 9,722 seconds (2hours, 42 minutes, 2 seconds) in total.

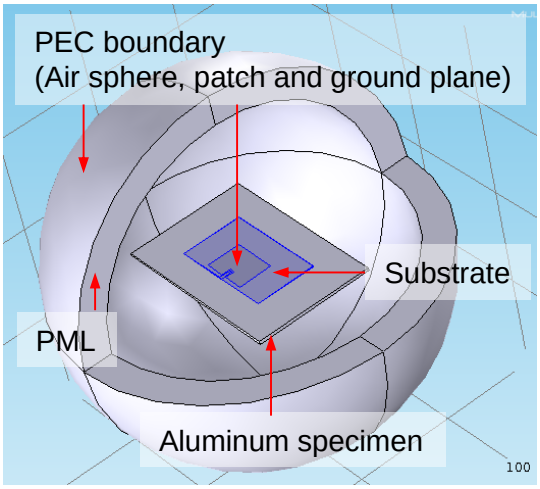

(a) Full-wave model

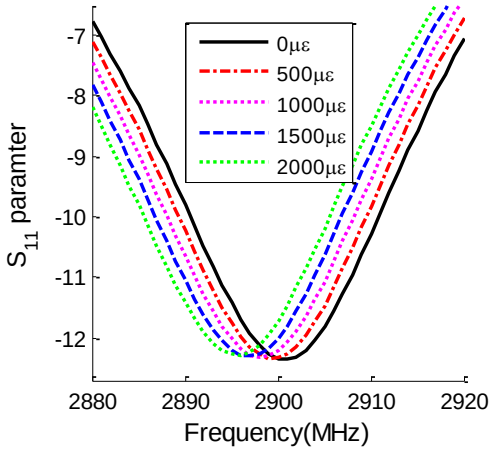

(b) S_{11} parameter
(frequency domain solver)

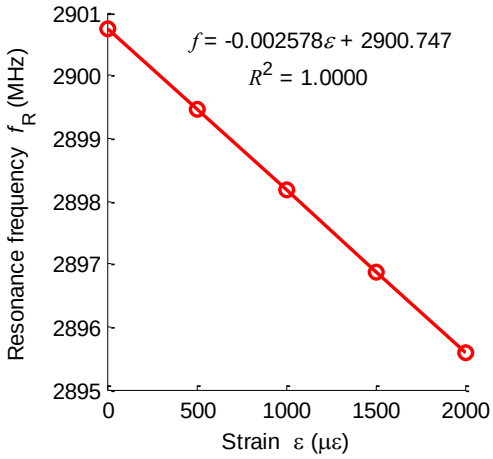

(c) Resonance frequency versus strain
(frequency domain solver)

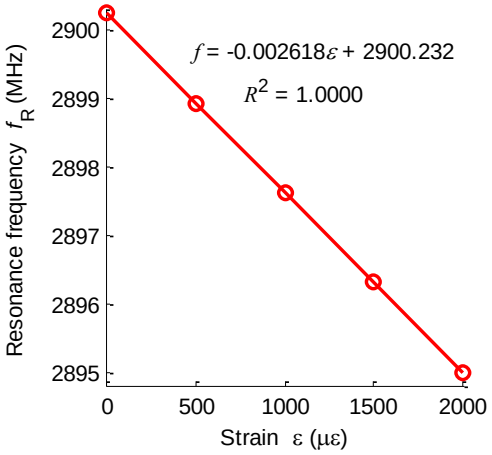

(d) Resonance frequency versus strain
(eigenfrequency solver)

Fig. 3.3. Comparison between frequency domain and eigenfrequency solvers in the full-wave model

The minimum valley point of a S_{11} plot presents the resonance frequency of the antenna at that strain level. As a post processing procedure, linear regression is performed between resonance frequency and strain to construct the strain sensitivity plot (Fig. 3.3(c)). The resonance frequency is 2,900.75MHz and strain sensitivity is –2,578Hz/με, which means 1με strain experienced by the patch antenna introduces a frequency change of –2,578Hz. The coefficient of determination is close to 1.0000, which shows a highly linear relationship. In the eigenfrequency solution, COMSOL LiveLink™ interface for MATLAB is adopted [45]. The mechanics simulation for certain strain level is conducted first in the mechanical domain. Through the LiveLink™, the [C], [R], and [T] from COMSOL are transferred into the MATLAB, which formulates [A] and [B] matrix (Eq. (3.16) and (3.17)).

Finally, MATLAB `eigs` command is used to compute the generalized eigenvalue solution of these sparse [A] and [B] matrix [45]. The `eigs` command is set to directly search the eigenfrequency close to 2,900MHz. The eigenfrequency is again extracted for each strain level. After performing linear regression between resonance frequency and strain data, the strain sensitivity is identified as –2,618Hz/με and resonance frequency at zero strain level is 2,900.23MHz (Fig. 3.3(d)). These are very close to the frequency-domain results. The coefficient of determination is also rounded off to 1.0000. The computing time at each strain level is 520 seconds (8 min 40 seconds) for the eigenfrequency solver, which is much faster than the frequency-domain solver. Therefore, it is demonstrated that the strain sensitivity simulation, the efficiency of the eigenfrequency solver is nearly 20 times higher than the frequency-domain solver.

3.2 FEM Modeling Techniques to Improve Simulation Efficiency

This section describes two electromagnetic FEM modeling techniques to reduce computational efforts with much less number of DOFs. Section 3.2.1 presents a cavity model, which removes the air volume from the full-wave model to reduce DOFs. However, it was observed that the cavity model cannot consider fringing effect due to the lack of air volume. In order to address this problem, Section 3.2.2 describes a partially air-filled cavity model which has a shallow air box on the patch antenna to compensate the fringing effect, without significantly increasing the number of DOFs.

3.2.1 Cavity Model

Although the eigenfrequency solution in the full-wave model provides similar results as the frequency-domain results, many spurious modes exist along with the resonance mode. Therefore, it can be difficult to identify the correct resonance mode and the corresponding frequency. By removing the air sphere and modifying boundary conditions correspondingly, a cavity model entails much less DOFs than the full-wave model. The cavity model of the 2.9GHz patch antenna is shown in Fig. 3.4(a). PEC boundaries are assigned as the microstrip patch and a ground plane. PMC boundaries are assigned to four sides and the top of the substrate. These boundary conditions exclude the aluminum plate in this electromagnetic domain simulation although the plate still exists in the mechanical simulation. Therefore, while electromagnetic domain of the full-wave model contains the aluminum plate and the air, the cavity model contains only the patch antenna and achieves faster computing. The total number of DOFs is 24,459, which is about 10 times smaller than that of the full-wave model.

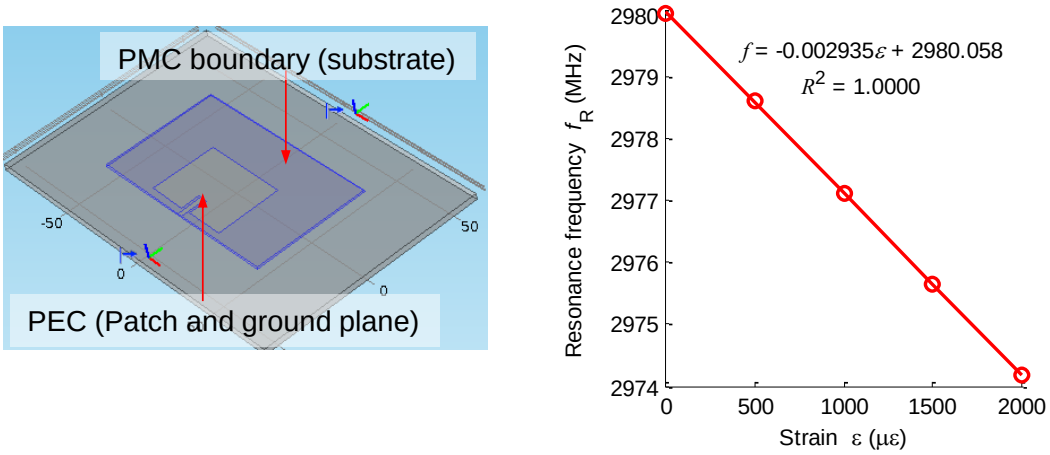

(a) Cavity model (b) Resonance frequency versus strain

Fig. 3.4. Cavity model simulation

Benefiting from much less DOFs, total computing time of the eigenfrequency solver at each strain level is only 8 seconds. However, because PMC boundary conditions are assigned on the substrate, a fringing field is not generated around the side of the microstrip patch in the cavity model. Therefore, the simulated resonance frequency at zero strain is 2980.06MHz (Fig. 3.4 (b)), which is 2.7% different from resonance frequency of the full-wave model in Section 3.1.4. Fig. 3.4 (b) shows the simulated strain sensitivity to be –2,935 Hz/με, which is also 12.1% higher than the full-wave model. In conclusion, although the cavity model requires less computation, this approach has notable inaccuracy because of neglecting the fringing effect.

3.2.2 Partially Air-Filled Cavity Model

By adding a small air box to the cavity model, the fringing field is restored in the electromagnetics simulation. Fig. 3.5 explains the electric field comparison between a cavity and a partially air-filled cavity model. The cavity model assigns PMC boundaries on the surface of the substrate, which blocks the generation of the electric field in the

horizontal direction. In other words, the direction of the electrical field is only vertical (Fig. 3.5(a)). The partially air-filled cavity model assigns PMC boundary conditions on the added air box, which provides enough space for generating the horizontal electrical field (Fig. 3.5(b)). Therefore, the partially air-filled cavity model is able to describe the fringing field.

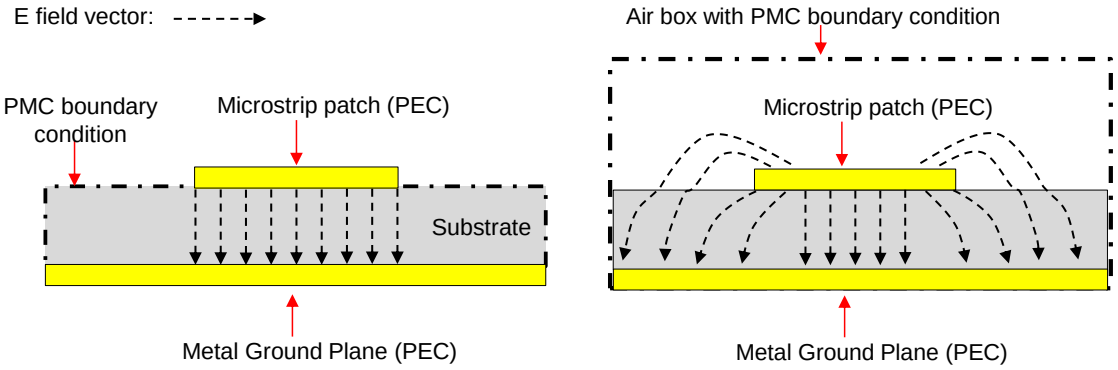

(a) Cavity model (b) Partially air-filled cavity model

Fig. 3.5. Electric field comparison

The partially air-filled cavity model of the 2.9GHz patch antenna is simulated in COMSOL. PEC boundary conditions are the same as in the cavity model in the previous section, and PMCs are assigned on the surface of the air box (Fig. 3.6(a)). The number of DOFs is 56,379. Although this number is larger than that of the cavity model, it is still five times smaller than the full-wave model. As shown in Fig. 3.6(b), simulated resonance frequency is 2905.91 MHz, which is much closer to the resonance frequency from the full wave model. Strain sensitivity is calculated as –2,677Hz/με and the coefficient of determination is close to 1.0000. The computing time at each strain level of the eigenfrequency solver is 25 seconds. The comparison among three FEM models in Section 3.1.4 is briefly summarized in Table 3.1. The partially air-filled cavity model is shown to achieve the best trade-off between computing time and accuracy.

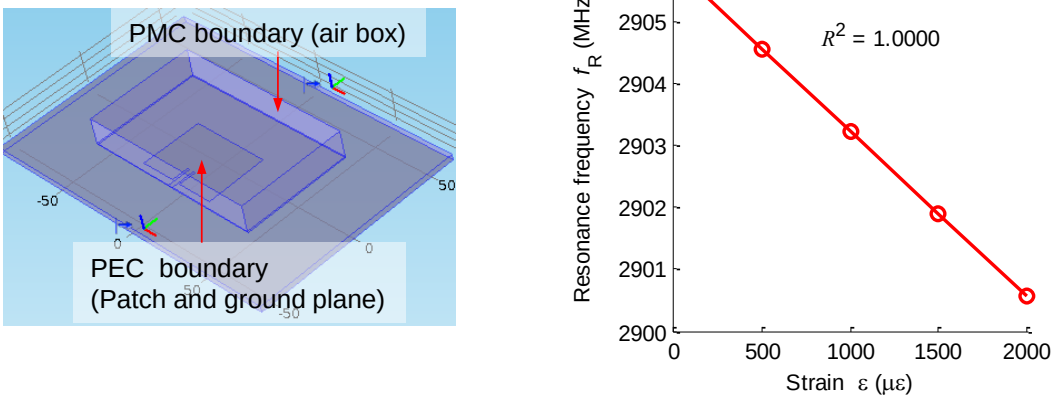

(a) Cavity model (b) Resonance frequency versus strain

Fig. 3.6. Partially air-filled cavity model simulation

Table 3.1. Comparison of three FEM models

	Full-wave model	**Cavity model**	**Partially air-filled cavity model**
Resonance frequency	2900.23MHz	2980.06MHz	2905.91MHz
Strain sensitivity	–2,618Hz/με	–2,935 Hz/με	–2,677Hz/με
No. of DOFs	259,975	24,459	56,379
Eigenfrequency solution time at each strain level	520 seconds	8 seconds	25 seconds

3.3 Eigenfrequency Solvers for Strain Sensing Simulation

In the strain sensing simulation, because changes of system matrices [A] and [B] between two adjacent strain levels are expected to be small, the differences in eigenfrequencies and eigenvectors are likewise small. In order to reach fast convergence, the eigenvalues and eigenvectors in the previous step can be utilized as starting vectors to search for solution at the next strain step. Section 3.3.1 explains the Rayleigh quotient

iteration (RQI) method, a commonly used eigenvalue algorithm. In Section 3.3.2, we proposed the inverse power iteration with Rayleigh quotient (IPIRQ) method which can be implemented to further improve the solution speed. Section 3.3.3 describes the overall COMSOL-MATLAB framework for strain sensing simulation using these eigenvalue perturbation algorithms.

3.3.1 Rayleigh Quotient Iteration (RQI) Method

The Rayleigh quotient iteration (RQI) method is implemented to improve computational efficiency of the eigenfrequency solution. To find the interested eigenfrequency of an antenna resonance mode, the shifted version of RQI is implemented (Fig. 3.7). As described in Eq.(3.17), [A] and [B] are complex-valued symmetric and sparse matrices. Since matrix with a smaller bandwidth generally improves speed of linear solvers, the reverse Cuthill-McKee algorithm [46] is applied to [A] and [B] first in step ①, producing a preordering permutation matrix [P] and preordered matrices $\left[\widetilde{\mathrm{A}}_{j+1}\right]$ and $\left[\widetilde{\mathrm{B}}_{j+1}\right]$ with smaller bandwidth. In step ②, since the generalized eigenvalue is not affected by the preordering process, λ_j at strain level ε_j is directly saved as an intermediate eigenvalue μ for starting the search. Meanwhile, the starting eigenvector $\{q\}$ is determined by reordering eigenvector $\{\Phi_j\}$ with permutation matrix [P]. In step ③, a temporary scaler d is computed once for later repetitive use in the `do-while` loop. In step ④, the LU factorization is performed with $\left[\widetilde{\mathrm{A}}_{j+1}\right]-\mu\left[\widetilde{\mathrm{B}}_{j+1}\right]$ to obtain a lower triangular matrix [L] and upper triangular matrix [U]. This LU factorization is the most computationally expensive step in RQI process. In step ⑤, the intermediate eigenvector $\{q\}$ is updated and normalized. In step ⑥, the intermediate eigenvalue μ is updated by the Rayleigh quotient. In step ⑦, the error of the current step is calculated. If the error is

lower than tolerance, the loop terminates; the eigenvalue λ_{j+1} and eigenvector $\{\Phi_{j+1}\}$ at strain level ε_{j+1} are updated in step ⑧. To restore the original eigenvector order, the intermediate eigenvector $\{q\}$ is reordered by the transpose of the permutation matrix $[\mathrm{P}]^{\mathrm{T}}$. If the error is higher than tolerance, the algorithm returns to step ④ and iterates the process.

① Preordering $[\mathrm{P}][\mathrm{A}_{j+1}][\mathrm{P}]^{\mathrm{T}} = [\widetilde{\mathrm{A}}_{j+1}]$;
$[\mathrm{P}][\mathrm{B}_{j+1}][\mathrm{P}]^{\mathrm{T}} = [\widetilde{\mathrm{B}}_{j+1}]$;

② $\mu = \lambda_j$; $\{q\} = [\mathrm{P}]\{\Phi_j\}$;

③ $d = \|[\widetilde{\mathrm{A}}_{j+1}]\| + \|\mu[\widetilde{\mathrm{B}}_{j+1}]\|$;

do {

④ LU factorization $([\widetilde{\mathrm{A}}_{j+1}] - \mu[\widetilde{\mathrm{B}}_{j+1}]) = [\mathrm{L}][\mathrm{U}]$;

⑤ $\{q\} = [\mathrm{U}^{-1}][\mathrm{L}^{-1}][\widetilde{\mathrm{B}}_{j+1}]\{q\}$;

$\{q\} = \dfrac{\{q\}}{\|\{q\}\|}$;

⑥ $\mu = \dfrac{\{q\}^{\mathrm{H}}[\widetilde{\mathrm{A}}_{j+1}]\{q\}}{\{q\}^{\mathrm{H}}[\widetilde{\mathrm{B}}_{j+1}]\{q\}}$;

⑦ error $= \dfrac{\|[\widetilde{\mathrm{A}}_{j+1}]\{q\} - \mu[\widetilde{\mathrm{B}}_{j+1}]\{q\}\|}{d}$;

} **while** (error > tolerance);

⑧ $\lambda_{j+1} = \mu$; $\{\Phi_{j+1}\} = [\mathrm{P}]^{\mathrm{T}}\{q\}$;

Fig. 3.7. RQI routine for shifted symmetric [A] and [B] formulations

3.3.2 Inverse Power Iteration with Rayleigh Quotient (IPIRQ) Method

Although the RQI method is commonly used, an inverse power iteration with Rayleigh quotient (IPIRQ) method is proposed to herein further improve computing speed. In the RQI method, the most computationally expensive step is the LU

factorization. When the RQI method iterates in the `do-while` loop, the LU factorization is computed in every iteration, increasing computational loads. In comparison, the proposed IPIRQ method performs the factorization only one time and effectively reuses factorization results ([L] and [U] matrices) for each iteration. Therefore, the IPIRQ method can be much faster than the ROI method in most cases [47]. The shifted version of the IPIRQ method is as shown in Fig. 3.8.

① Preordering $[\mathrm{P}][\mathrm{A}_{j+1}][\mathrm{P}]^{\mathrm{T}} = [\widetilde{\mathrm{A}}_{j+1}]$;
$[\mathrm{P}][\mathrm{B}_{j+1}][\mathrm{P}]^{\mathrm{T}} = [\widetilde{\mathrm{B}}_{j+1}]$;

② $\mu = \lambda_j$; $\{q\} = [\mathrm{P}]\{\Phi_j\}$;

③ $d = \|[\widetilde{\mathrm{A}}_{j+1}]\| + \|\mu[\widetilde{\mathrm{B}}_{j+1}]\|$;

④ LU factorization $([\widetilde{\mathrm{A}}_{j+1}] - \mu[\widetilde{\mathrm{B}}_{j+1}]) = [\mathrm{L}][\mathrm{U}]$;

do {

⑤ $\{q\} = [\mathrm{U}^{-1}][\mathrm{L}^{-1}][\widetilde{\mathrm{B}}_{j+1}]\{q\}$;

$\{q\} = \dfrac{\{q\}}{\|\{q\}\|}$;

⑥ $\mu = \dfrac{\{q\}^{\mathrm{H}}[\widetilde{\mathrm{A}}_{j+1}]\{q\}}{\{q\}^{\mathrm{H}}[\widetilde{\mathrm{B}}_{j+1}]\{q\}}$;

⑦ error $= \dfrac{\|[\widetilde{\mathrm{A}}_{j+1}]\{q\} - \mu[\widetilde{\mathrm{B}}_{j+1}]\{q\}\|}{d}$;

} while (error > tolerance);

⑧ $\lambda_{j+1} = \mu$; $\{\Phi_{j+1}\} = [\mathrm{P}]^{\mathrm{T}}\{q\}$;

Fig. 3.8. IPIRQ routine for shifted symmetric [A] and [B] formulations

The process from step ① to ③ is the same as the RQI method. But, in step ④, the LU factorization is moved out of the `do while` loop. The process from step ① to ⑧ also follows the RQI method. Compared with the RQI method, the [L] and [U] matrices used at step ⑤ of the IPIRQ method are only accurate at the first iteration. At the second

or any later iteration, the RQI performs factorization to $\left[\widetilde{\mathrm{A}}_{j+1}\right]-\mu\left[\widetilde{\mathrm{B}}_{j+1}\right]$ with the updated μ value, to get updated [L] and [U]. However, IPIRQ reuses the [L] and [U] from the first iteration as approximation to these two matrices at the current iteration. Therefore, despite time saving, the accuracy of IPIRQ is yet to be examined.

3.3.3 COMSOL-MATLAB Framework

The antenna sensor models can be easily built in COMSOL through user friendly graphical interface, but it is not convenient to implement customized eigenvalue solvers into COMSOL graphical interface. Instead, COMSOL LiveLink for MATLAB allows the customized solvers to be applied to COMSOL-generalized matrices in electromagnetic domain. Fig. 3.8 shows the COMSOL-MATLAB communication process using eigenvalue techniques for updating sensor resonance frequencies at multiple strain levels. The simulation model is first built in COMSOL with proper mechanical and electromagnetic boundary conditions. Matrices $[\mathrm{C}_0]$, $[\mathrm{R}_0]$, and $[\mathrm{T}_0]$ in Eq. (3.13) are then generated by COMSOL and transferred to MATLAB. These matrices are used to construct $[\mathrm{A}_0]$ and $[\mathrm{B}_0]$according to Eq. (3.17). The eigenvalue λ_0 and eigenvector $\{\Phi_0\}$ are calculated through eigenvalue solver at zero strain level ε_0.

Upon the simulation at zero strain level and later at a *j*-th strain level, the antenna structure is subjected to corresponding loading in COMSOL. The deformed antenna shape is used to generate inductance and capacitance matrices at strain level ε_j. The corresponding system matrices $\left[\mathrm{A}_j\right]$ and $\left[\mathrm{B}_j\right]$ are constructed in MATLAB. An eigenvalue perturbation algorithm can then be applied to calculate the eigenvalue λ_j and eigenvector $\left\{\Phi_j\right\}$ at strain ε_j, based on λ_{j-1} and $\left\{\Phi_{j-1}\right\}$ from the previous strain step. The updating process continues for all required strain levels.

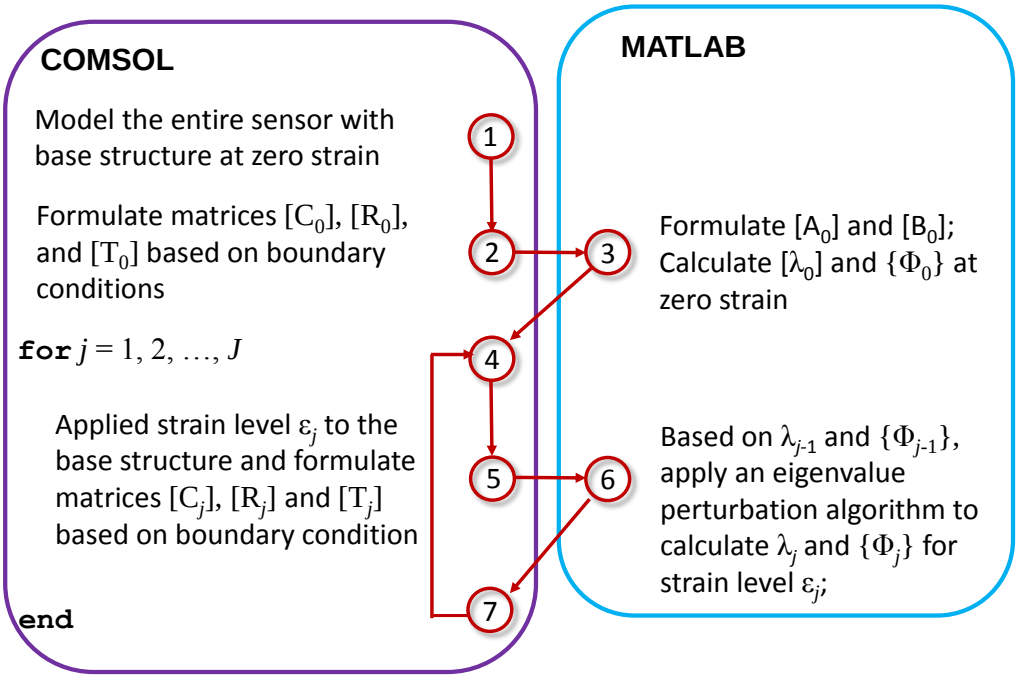

Fig. 3.9. COMSOL-MATLAB communication

3.4 Validation Example

To validate the accuracy and efficiency of the proposed partially air-filled cavity model and the IPIRQ eigenvalue perturbation algorithm, the same 2.9GHz patch antenna is investigated. Four strain levels are simulated, ranging 500~2,000 με with a strain step of 500 με. The eigenfrequency at each strain level is first calculated by `eigs` function in MATLAB. To check the effect of different starting vectors to the computation error and time, a randomly generated vector and the eigenvector from previous strain level are adopted as the starting vector, respectively for comparison. The RQI and the IPIRQ methods are applied for comparison with the two MATLAB `eigs` solutions with different starting vectors. The error tolerance for the four methods (two `eigs`, RQI, and IPIRQ) is set to 10^{-16}. The computed resonance frequency results from the four solvers are compared and summarized in Fig. 3.10.

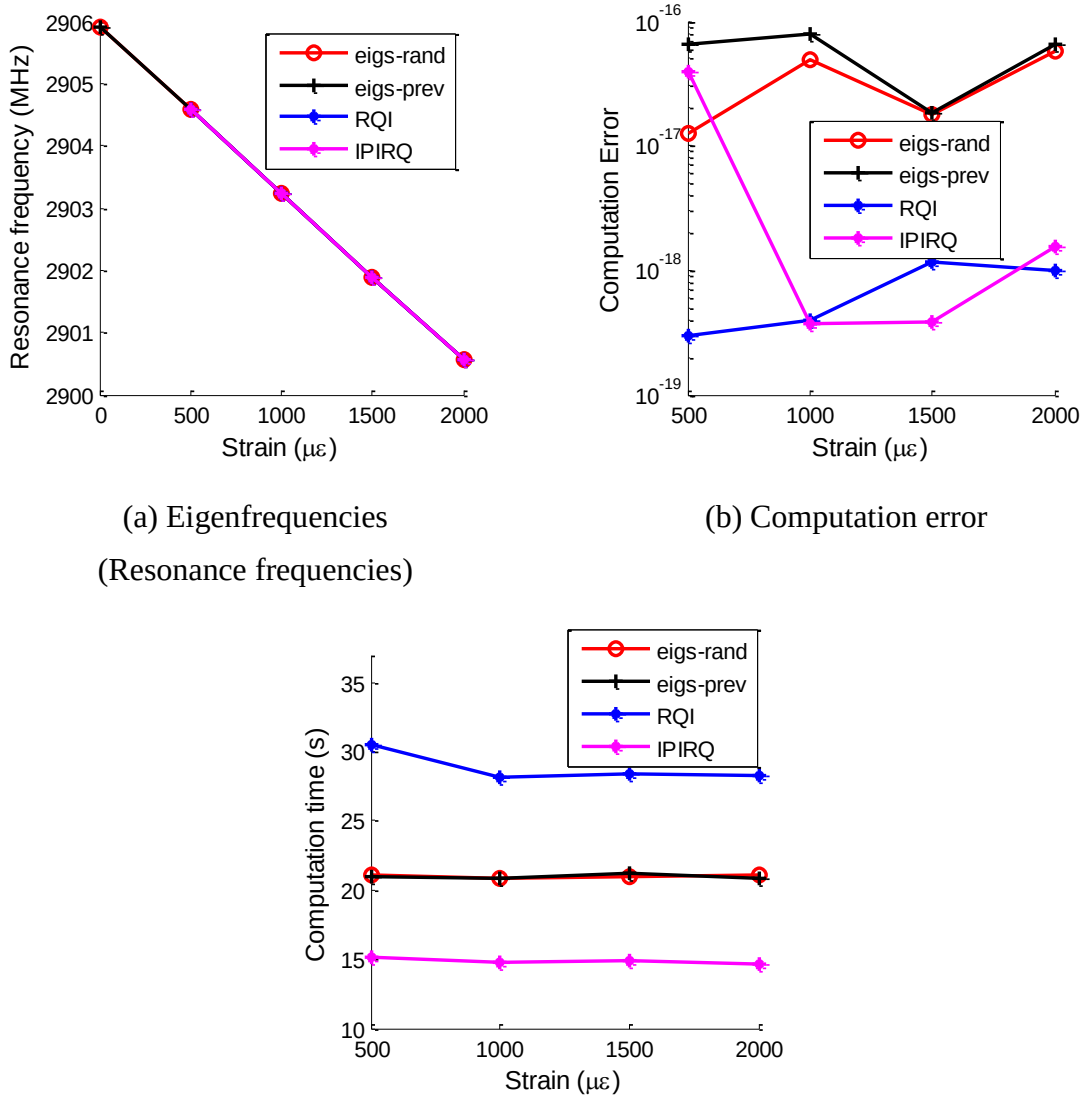

(a) Eigenfrequencies (Resonance frequencies)

(b) Computation error

(c) Computation time

Fig. 3.10. Eigenfrequency results comparison between eigs solvers and proposed method

The legend "eigs-rand" denotes the results from eigs function with randomly generated vector as starting vector; the legend "eigs-prev" indicates results from `eigs` function with previous eigenvector as starting vector; the legend "RQI" and "IPIRQ" denote the results from the RQI and the IPIRQ methods, respectively. In this example, the resonance frequencies from four solution methods show good match (Fig. 3.10(a)) at all strain steps. To further compare the solution accuracy, following error index is defined:

$$\text{error} = \frac{\left\| \mathrm{A}_{j+1}\{\Phi_{j+1}\} - \lambda_{j+1}\mathrm{B}_{j+1}\{\Phi_{j+1}\} \right\|}{\left\| \mathrm{A}_{j+1} \right\| + \left\| \lambda_{j+1}\mathrm{B}_{j+1} \right\|} \tag{3.20}$$

where λ_{j+1} and $\{\Phi_{j+1}\}$ are the computed eigenvalue and eigenvector at (j+1)-th strain step.

As shown in Fig. 3.10(b), the computational errors of all methods are lower than 1×10^{-16}. Computation error for the RQI and the IPIRQ methods is between 3.8×10^{-18} to 4.2×10^{-18}, both smaller than the `eigs` solutions. Comparison of computation time is plotted in Fig. 3.10(c). The computation time of IPIRQ is the fastest, which is about 1.3 times faster than the `eigs` solutions and 1.86 times faster than the RQI method. To explain the difference between RQI and IPIRQ, Table 3.2 provides computation time for every step of these two methods at 1,000με level.

Table 3.2. Computation time (seconds) of RQI and IPIRQ at 1,000 με

Step	**RQI**		**IPIRQ**		
①	0.1802		0.1923		
②	0.0012		0.0014		
③	0.3923		0.4170		
	First iteration	Second iteration	First iteration	Second iteration	Third iteration
④	13.4173	13.6476	13.4474		
⑤	0.2135	0.2072	0.2020	0.1855	0.1974
⑥	0.0127	0.0113	0.0124	0.0102	0.0101
⑦	0.0338	0.0384	0.0399	0.0372	0.0334

The step numbers follow Fig. 3.7 and Fig. 3.8. As shown in the table, a critical time-consuming step of both algorithms is LU factorization (Step ④ in both methods). Therefore, although RQI has only two iterations and IPIRQ needs three iterations to converge, IPIRQ is more efficient than RQI by reusing LU factorization while achieving similar accuracy.

3.5 Summary

This chapter first presents electromagnetic finite element formulation of antenna sensors for both frequency domain solver and eigenfrequency solver. The 2.9 GHz patch antenna simulation is performed using both solvers, and the calculated resonance frequency results are compared. The eigenfrequency solver consumes only about 5% of the time required by the frequency-domain solver, while providing similar accuracy.

In order to reduce computational loads, two FEM models (cavity and partially air-filled cavity models) are proposed. While the cavity model significantly reduces simulation time, the accuracy is not reliable due to the absence of air volume. It is discovered that the partially air-filled cavity model not only reduces computational efforts but also maintains accuracy for the electromagnetic simulation. To further improve the solution efficiency, two eigenvalue perturbation methods, RQI and IPIRQ are studied. The solution accuracy and efficiency are compared with MATLAB `eigs` command. The results show that the commonly used RQI method achieves high computation accuracy, but it is relatively slower than other solutions. Meanwhile, the proposed IPIRQ method achieves the best balance between accuracy and timing in this application.

Overall, the proposed antenna simulation approach, using partially air-filled model and the IPIRQ eigenvalue perturbation method, provides an eigenvalue solution in 14.82 seconds for the 2.9GHz antenna at 1,000 με. In comparison, the conventional

frequency domain solver requires 9,722 seconds (2hours, 42 minutes, 2 seconds). The efficiency improvement is significant. The proposed approach provides a simulation framework enabling much more efficient antenna sensor designs.

CHAPTER 4 MULTI-PHYSICS MODEL UPDATING OF MATERIAL PARAMETERS

Multi-physics FE models have been used to not only design antenna sensors but also predict wireless strain sensing performances of the sensors. An FE model usually uses nominal values of material property parameters or assumes ideal boundary conditions. Although necessary for modeling, these factors always lead to discrepancy between numerical analysis and experimental measurements. To resolve the discrepancy, model updating techniques can be adopted to extract actual parameter values from experimental data. Upon material parameter model updating, FEM analysis results can better reflect physical reality than the initial models with nominal parameter values.

In this chapter, Section 4.1 presents mechanical parameter updating. Extensive nonlinear tensile tests for copper and substrate (antenna sensors are made of these two materials) are conducted to investigate nonlinear behaviors. A rectangular substrate patch with copper claddings is mounted on a dog-bone aluminum plate examing the nonlinear mechanical behavior, including strain transfer ratio from the aluminum plate to the patch antenna sensor. The Menegotto-Pinto phenomenological model [48, 49] is used to describe the mechanical behavior of the aluminum, copper, and sensor substrate. A zero-length spring model is used to describe the adhesive between the sensor and the aluminum plate. After being implemented into a COMSOL FE model, model parameter updating is performed to minimize the discrepancy of strain transfer ratios between experimental data and numerical simulations.

Section 4.2 then describes electromagnetic parameter updating. The effect of substrate dielectric constant change under strain has been neglected in many antenna sensor simulations in past studies [4-6]. However, dielectric constant change can significantly affect antenna resonance frequency shift when a sensor is under strain. To accurately measure dielectric constant values under strain, a tensile test of a transmission line is conducted. Finally, the updated mechanical parameters from Section 4.1 and the

updated dielectric constant changes are built into a multi-physics COMSOL FE model to achieve more accurate modeling. The results are summarized and discussed in Section 4.3.

4.1 Mechanical Parameter Updating

This section proposes methods of the mechanical parameter updating. Section 4.1.1 presents experimental investigation of mechanical parameters through nonlinear tensile tests. Section 4.1.2 introduces the Menegotto-Pinto phenomenological model for mechanical property updating of aluminum and sensor materials and a zero-length spring model for shear modulus updating of adhesive. The model updating procedures and results are explained in Section 4.1.3.

4.1.1 Experimental Investigation of Mechanical Parameters

To investigate nonlinear mechanical behavior of corresponding materials, large-strain tensile experiments are conducted. Section 4.1.1.1 and Section 4.1.1.2 present tensile test results for Rogers RT/duroid®5880 substrate material and copper, respectively. Section 4.1.1.3 presents strain transfer ratio test for antenna sensors on an aluminum specimen.

4.1.1.1 Nonlinear tensile test for substrate

In this chapter, the nonlinear behavior of the Rogers RT/duroid®5880 substrate sheet is investigated. The anisotropic material sheet is reinforced by fiber glass along the "machine direction" (MD). The orthogonal in-plane direction to the machine direction called as the "cross machine direction" (CMD). To characterize mechanical properties of the material based on the two directions (MD and CMD), two specimens are fabricated following the ASTM standard [50] (Fig. 4.1). The dimension of the specimen is 0.65in. × 0.5in. × 31 mil. (16.51 mm × 12.7mm × 0.787mm). MD and CMD specimens are mounted on a 2.25-kip Instron 5566 tensile frame (Fig. 4.1 (c)). The extensometer

provides strain measurement data in the tensile testing. The loading rate is 1,000 με/min and strain is applied up to 10,000 με.

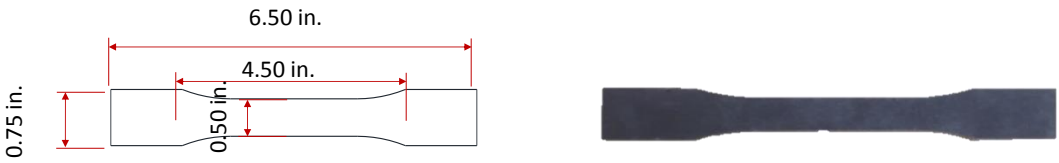

(a) Drawing of substrate specimen (b) Photo of substrate specimen

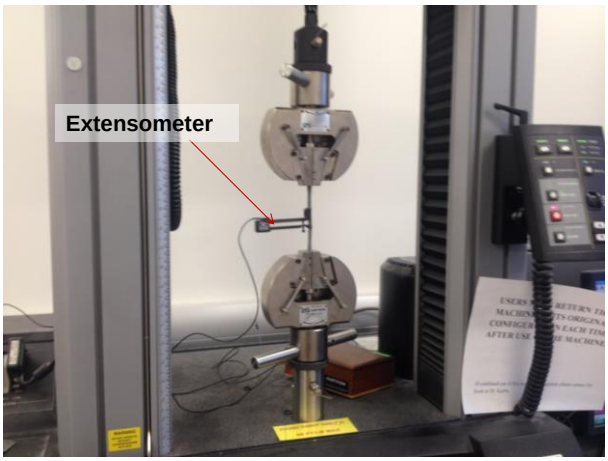

(c) Experimental setup

Fig. 4.1. Tensile test for substrate

The stress-strain relationships for MD and CMD specimens are shown in Fig. 4.2. The plot shows nonlinear constitutive relationship for both specimen, and the difference between the two directions.

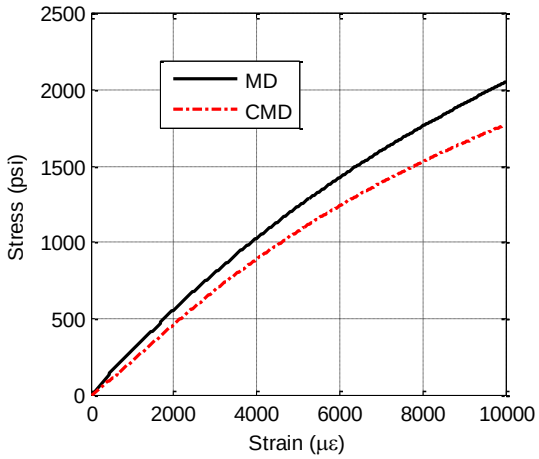

Fig. 4.2. Result of nonlinear tensile tests for substrate (stress-strain curve)

4.1.1.2 Nonlinear tensile test for copper

A patch antenna sensor is usually made of one substrate sheet sandwiched between two copper claddings. The thickness of copper cladding is 17 μm (Fig. 4.3(a)). Upon fabrication, the 17μm-thick copper claddings are attached on two sides of the substrate sheet (Fig. 4.3(b)). Using a dog bone specimen with the substrate sheet sandwiched with two copper claddings, experimental setup follows the previous tensile test for the substrate. The stress in copper at strain level ε is calculated.

$$\sigma_c(\varepsilon) = \frac{F_T(\varepsilon) - \sigma_s(\varepsilon)A_s}{2A_c} \tag{4.1}$$

where ε is applied strain level; $F_T(\varepsilon)$ is total force at strain level ε; $\sigma_s(\varepsilon)$ substrate stress at strain level ε from the previous test (Fig. 4.2); A_s and A_c are section areas of substrate and copper, respectively. Stress-strain relationship of copper is shown in Fig. 4.4.

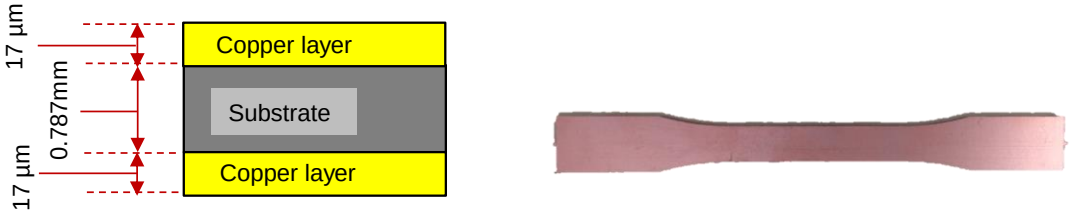

(a) Illustration of substrate with copper layers (not to scale)

(b) Photo of specimen

Fig. 4.3 Specimen of substrate sheet sandwiched between copper claddings

The copper shows the linear-elastic behavior under 2,000με level. The yielding occurs at around 2,500 με and corresponding stress level is 12ksi. After yielding point, copper is under nonlinear plastic range.

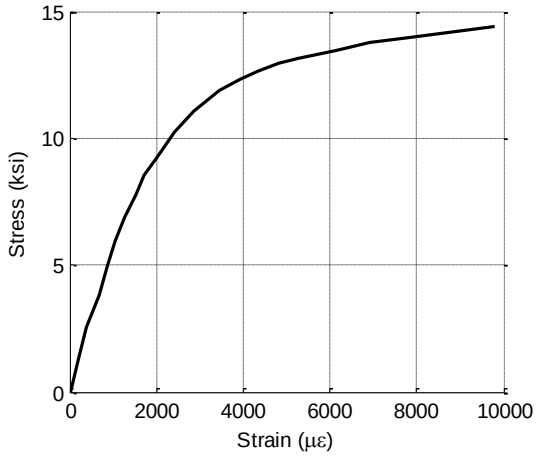

Fig. 4.4. Result of nonlinear tensile test for copper (stress-strain curve)

4.1.1.3 Strain transfer ratio test

In order to investigate the nonlinear mechanical behavior of strain transfer ratio for patch antenna sensors, a dog-bone aluminum specimen is fabricated. The rectangular substrate patch is installed on the aluminum specimen. The substrate patch consists of the same components as a patch antenna sensor: top copper cladding, substrate, and bottom copper cladding. Fig. 4.5 shows the schematic of the aluminum specimen and the substrate patch. The properties of the material are listed in Table 4.1.

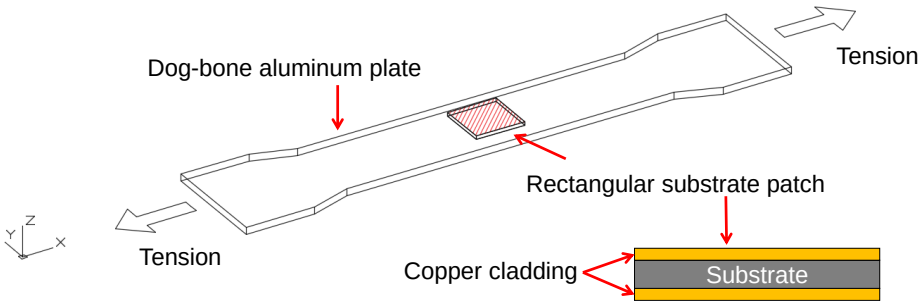

Fig. 4.5. Schematic of an aluminum plate and a substrate patch

Table 4.1. Dimensions and material properties

	Aluminum specimen	Substrate	Copper cladding
Dimension (in)	16 × 3 × 0.125 (middle part)	1.772 × 1.772 × 0.031	1.772 × 1.772 × 0.031
Material type	6061 aluminum alloy	Rogers RT/duroid®5880	Copper
Poisson ratio	0.33	0.4	0.33

To quantify the strain transfer from the specimen to the top of copper cladding, a nonlinear tensile test is conducted. Fig. 4.6 (a) shows the photo of central area of the tensile specimen. Five metal foil strain gages are installed near the center of the aluminum tensile specimen, for measuring the axial strain on the aluminum specimen. Another six strain gages are installed on the top copper cladding, for measuring the strain transferred to the top surface. For installations of strain gages and the substrate patch, M-Bond 610 strain gage adhesive (Vishay Precision Group, Inc.) is applied. The aluminum specimen is mounted on the MTS 810 testing machine. Starting from zero strain to 7,000με, 71 strain levels are applied (Fig. 4.6 (b)). Stress-strain curve for the aluminum specimen is shown in Fig. 4.6 (c). Before 4,000 με level, the aluminum specimen shows linear-elastic behavior and the yielding stress is approximately 37ksi. After 4,000 με, the aluminum is under nonlinear-inelastic range. The strain transfer ratio increases slightly between the strain levels of 1,000 με and 3,000 με, and peaks at 95% ((Fig. 4.6 (d)). After

the peak, strain transfer ratio decreases considerably down to 90% at the strain level of 6,000με. In order to update the mechanical properties of all materials for constitutive relationship will be introduced in the next section. Likewise, a zero-length spring model for shear modulus updating of the adhesive will be presented.

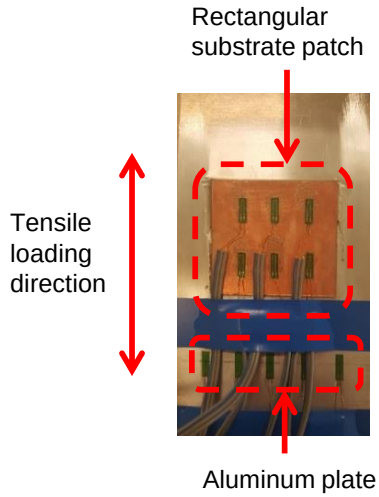

(a) Photo of tensile specimen

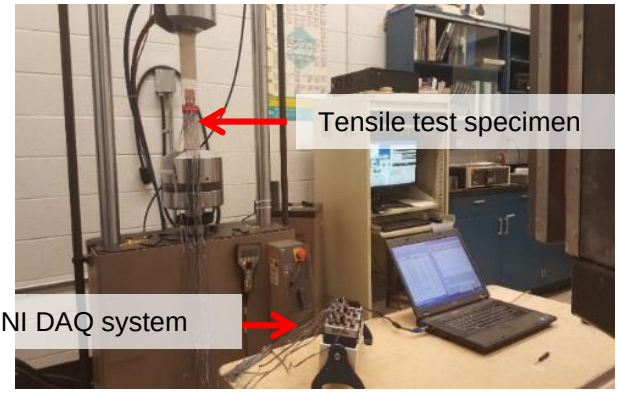

(b) Photo of experimental setup

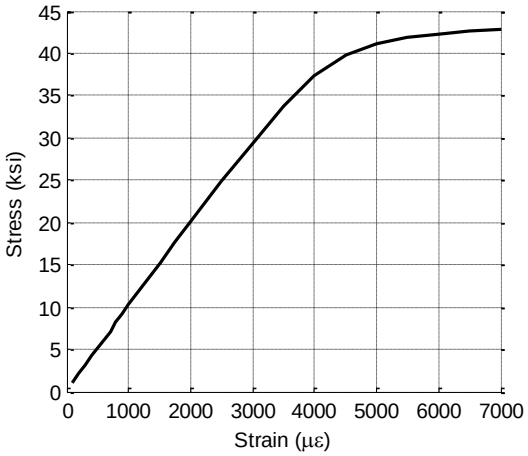

(c) Stress-strain curve for aluminum plate

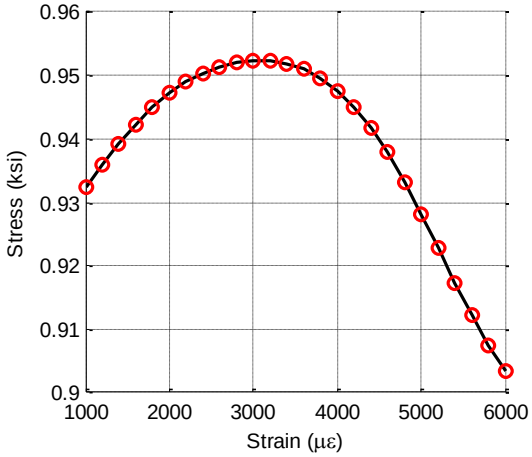

(d) Strain transfer ratio

Fig. 4.6. Nonlinear tensile test

4.1.2 Mechanical Parameter Modeling

In this Section, mechanical parameter modeling techniques are introduced. Section 4.1.2.1 explains a numerical phenomenological model describing constitutive relationships. Section 4.1.2.2 presents a zero-length spring model to describe shear modulus of the adhesive.

4.1.2.1 Constitutive relationships for aluminum, copper, and substrate

A phenomenological model is a mathematical model which explains empirical observations of phenomena such experimental results. Although the phenomenological model is not directly derived from fundamental theory, the model attempts to describe real behaviors through key parameters. In the stress-strain relationship of materials, the primary advantage of the phenomenological model is that it remains conceptually simple while offering accuracy comparable with the more sophisticated material behavior. Furthermore, the model is computationally efficient, and easy to implement in a finite element program. In this study, the Menegotto-Pinto phenomenological model [48, 49] is proposed to update mechanical properties. The general form of the Menegotto-Pinto model is as follows:

$$\frac{\sigma(\varepsilon)}{\sigma_0} = b\frac{\varepsilon}{\varepsilon_0} + d = b\frac{\varepsilon}{\varepsilon_0} + \frac{(1-b)\frac{\varepsilon}{\varepsilon_0}}{\left[1+\left(\frac{\varepsilon}{\varepsilon_0}\right)^n\right]^{\frac{1}{n}}} \tag{4.2}$$

where b is the ratio of the final to initial tangent stiffness, d is graphically described in Fig. 4.7; σ_0 (neither yielding nor ultimate stress) is a normalized stress factor; ε_0 (neither yielding nor ultimate strain) is a normalized strain factor; it should be noted that both σ_0 and ε_0 are obtained from the intersection point from initial and final tangent curve; n describes nonlinearity of a stress-strain curve; it should be noted that n is calculated at $\varepsilon/\varepsilon_0 = 1$:

$$n = \frac{\log 2}{\log(1-b) - \log d'} \tag{4.3}$$

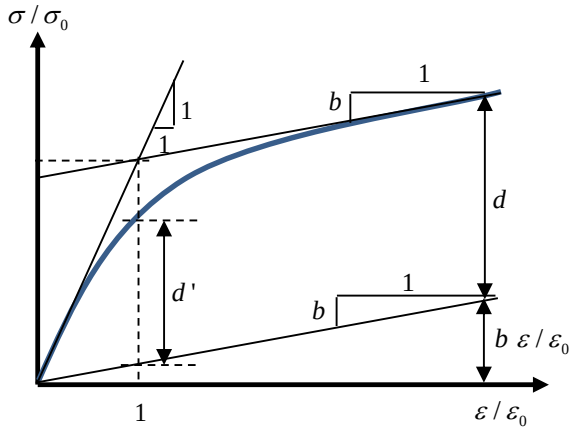

Fig. 4.7. Menegotto and Pinto phenomenological model [48, 49]

To obtain an accurate the Menegotto-Pinto model for each of materials, b, n, ε_0, and σ_0 are chosen as the corresponding set of updating variables.

4.1.2.2 Shear modulus model for adhesive

The strain transfer ratio in Section 4.1.1.3 is dependent on shear modulus of adhesive. Numerical FE modeling of adhesive in three dimensions can describe the strain transfer with appropriate finite element meshing (Fig. 4.8(a) and (b)). However, the adhesive layer is very thin, compared to other layers, such as the aluminum specimen or sensor substrate. This can cause a large concentration of finite elements near the adhesive layer and lead to high computational cost and time. On the other hand, if the adhesive layer is neglected in FE model, the perfect bonding will lead to inaccurate modeling of strain transfer. In order to address this issue, a zero-length spring model is proposed in this study (Fig. 4.8(c) and (d)). While the zero-length spring model efficiently reduces computational loads, strain transfer ratio is still considered in the FE model. Using experimental data, the spring stiffness is updated to reduce the difference in strain transfer ratio between experimental and FEM results. The tangential spring stiffness K_A is at strain level ε

$$K_A(\varepsilon) = \frac{G(\varepsilon)}{t} \tag{4.4}$$

where G is tangential shear modulus of the adhesive at ε; t is the thickness of the adhesive and the measured value is 0.02mm.

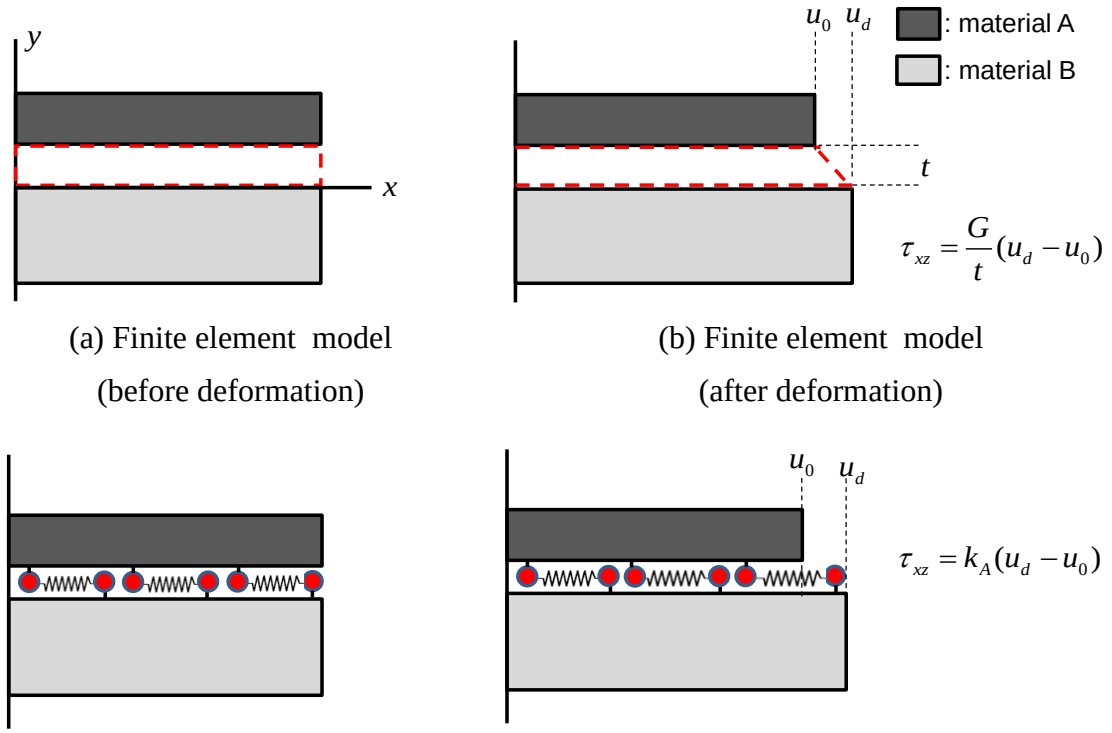

(a) Finite element model (before deformation)

(b) Finite element model (after deformation)

(c) Zero-length spring model (before deformation)

(d) Zero-length spring model (after deformation)

Fig. 4.8. Comparison of adhesive models

The shear modulus G also shows nonlinear behavior when stain increases. In order to conveniently implement the shear modulus G into the zero-length spring model, the shear modulus G is described with modification of the Menegotto and Pinto phenomenological model.

$$G(\varepsilon) = \frac{E(\varepsilon)}{2(1+\nu)} \tag{4.5}$$

where $E(\varepsilon)$ is Young's modulus of the adhesive from the Menegotto and Pinto phenomenological model; ν is Poisson's ratio of the adhesive.

4.1.3 Model Updating

Model updating procedure and results are presented in this section. Section 4.1.3.1 describes model updating setup and results of substrate, copper, and aluminum, respectively. Section 4.1.3.2 presents shear modulus updating for the adhesive.

4.1.3.1 Updating of constitutive models

Model updating aims to minimize the difference between experiment and simulation. For each material, the formulation has four optimization variables $\mathbf{x} = [b, n, \varepsilon_0, \sigma_0]$ as updating parameters. The optimization problem for model updating is formulated as:

$$\underset{\mathbf{x}}{\text{minimize}} \sum_{i=1}^{m} \left[\sigma_{\text{Exp}}(\varepsilon_i) - \sigma_{\text{FEM}}(\varepsilon_i, \mathbf{x})\right]^2 \tag{4.6}$$

$$\text{subject to } \mathbf{x}_{\text{L}} \leq \mathbf{x} \leq \mathbf{x}_{\text{U}}$$

where m is the number of strain steps; $\sigma_{\text{Exp}}(\varepsilon_i)$ is stress at strain ε_i measured from the experiment; $\sigma_{\text{FEM}}(\varepsilon_i, \mathbf{x})$ is simulated stress at strain ε_i using parameter $\mathbf{x}$ for the Menegotto-Pinto model; $\mathbf{x}_{\text{L}}$ and $\mathbf{x}_{\text{U}}$ are (element-wise) lower and upper bounds of the updating vector parameter $\mathbf{x}$.

In the substrate model updating for property along the mechanical direction (MD), the initial values of the updating variables are defined as:

$$\mathbf{x_0^{MD}} = [b, n, \varepsilon_0, \sigma_0] = [0.04, \quad 5.0, \quad 0.06, \quad 10{,}000(\text{psi})] \tag{4.7}$$

The initial parameters are from datasheet of Rogers RT/duroid®5880 substrate; lower and upper bounds of parameters are empirically set as:

$$\mathbf{x_L^{MD}} = [0.0, 0.0001, \quad 0.005, \quad 10{,}000 * 0.1] \tag{4.8}$$

$$\mathbf{x_U^{MD}} = [1.0, \quad 20, \quad 0.1, \quad 10{,}000 * 10] \tag{4.9}$$

As a global optimization solver, `MultiStart` in MATLAB optimization toolbox is adopted to solve the model updating problem. Using `MultiStart`, 1000 trial starting points for the updating variables ($\mathbf{x_0^{MD}} = [b, n, \varepsilon_0, \sigma_0]$) for each of four parameters are randomly generated.

Starting from each of 1,000 points, the `lsqnonlin` (nonlinear least-squares solver) with "trust-region-reflective" algorithm finds a local optimum around the point. Fig. 4.10 plots the corresponding 1,000 optimized values. The optimized values for parameter n and ε_0 mostly converge to 1.136 and 0.0173, respectively. Optimized values for parameter b and σ_0 do not show any convergence. The smallest objective function value is 982.7 and corresponding optimized parameters are:

$$\mathbf{x^{MD^*}} = [0.042, \quad 1.136, \quad 0.0173, \quad 5{,}406] \tag{4.10}$$

Fig. 4.11 plots stress strain relation of the experimental, initial, optimized results. After model updating procedure, the numerical model matches well with the experimental result.

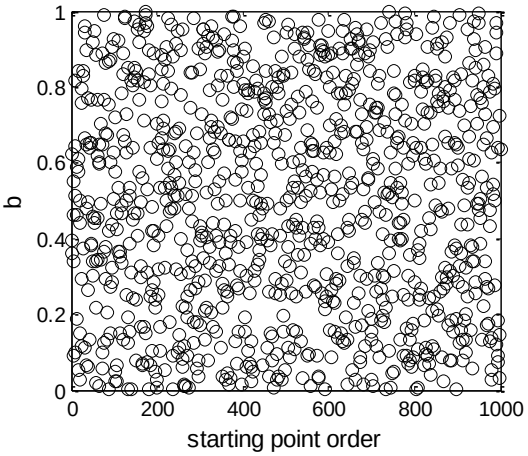

(a) Parameter b

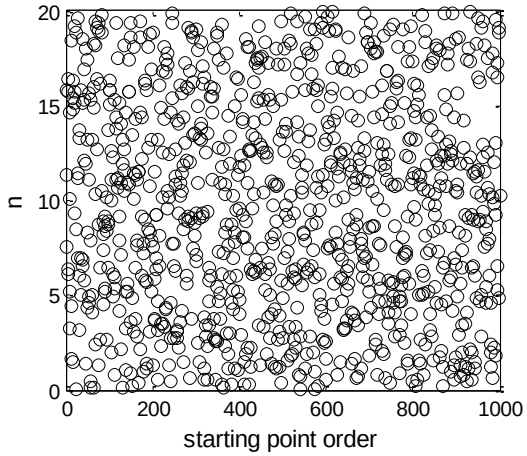

(b) Parameter n

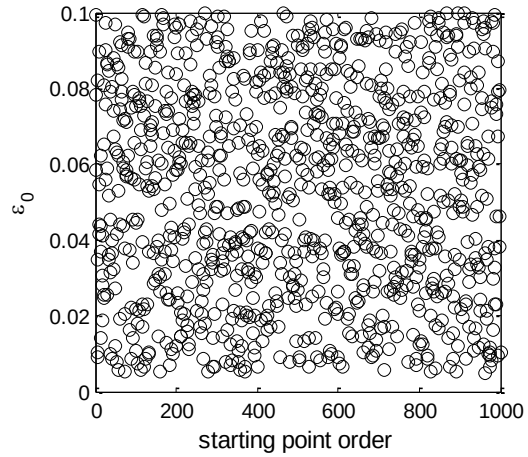

(c) Parameter ε_0

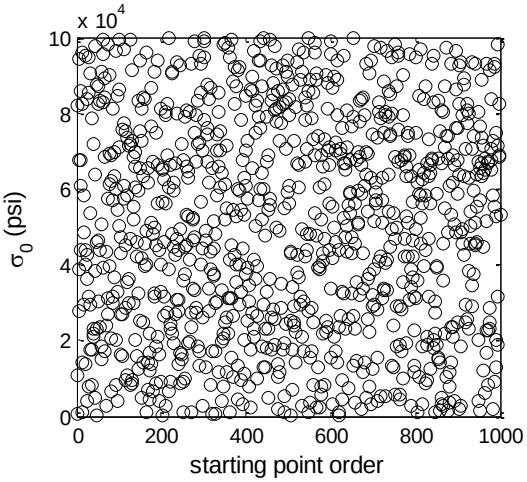

(d) Parameter σ_0

Fig. 4.9. 1000 starting points for updating substrate constitutive model along MD

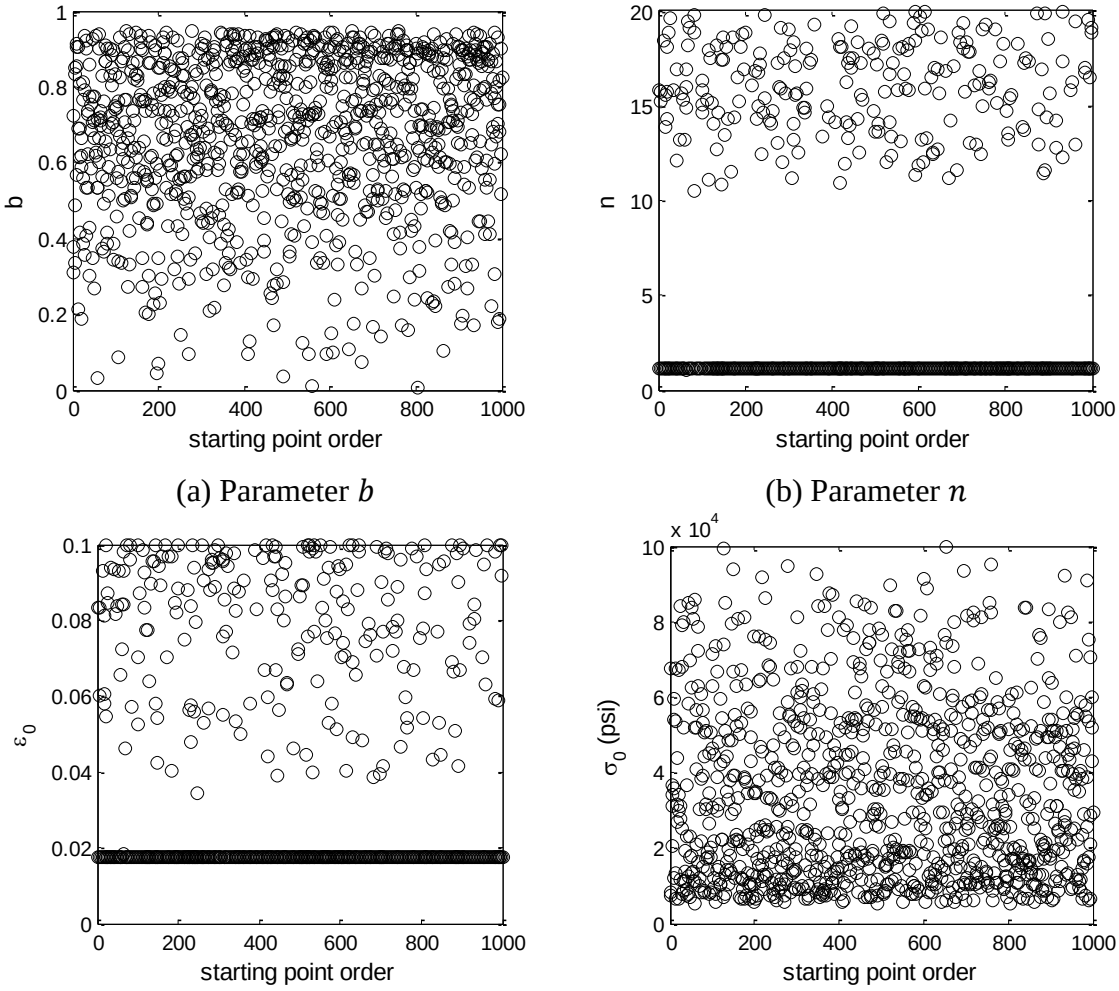

(a) Parameter b (b) Parameter n

(c) Parameter ε_0 (d) Parameter σ_0

Fig. 4.10. Optimized points for updating substrate constitutive model along MD

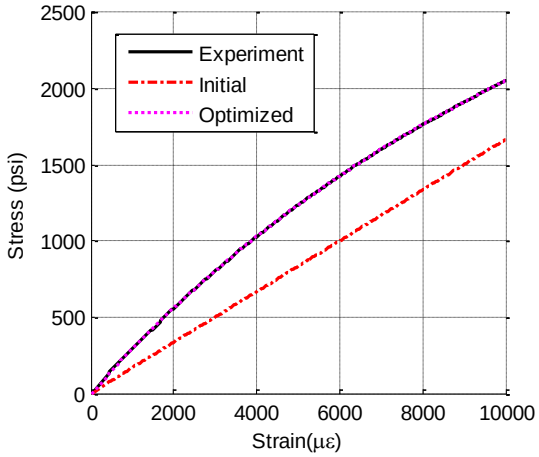

Fig. 4.11. Updating results for substrate along MD (stress-strain curve)

For CMD direction updating, the initial model parameters $\mathbf{x_0^{CMD}}$ and bounds are same as MD updating (Eq. (4.7), (4.8), and (4.9)). The 1,000 sets of search starting values are as shown in Fig. 4.12. The optimized sets of values are shown in Fig. 4.13. Similar as the previous model updating along MD, while optimal parameter n and ε_0 mostly converge to 1.85 and 0.012, respectively, b and σ_0 do not converge consistently. Finally, optimized parameters are chosen as:

$$\mathbf{x^{CMD^*}} = [0.043, \quad 1.846, \quad 0.0120, \quad 2{,}967] \tag{4.11}$$

The updated numerical model also shows much closer stress-strain relationship with the experimental results (Fig. 4.14).

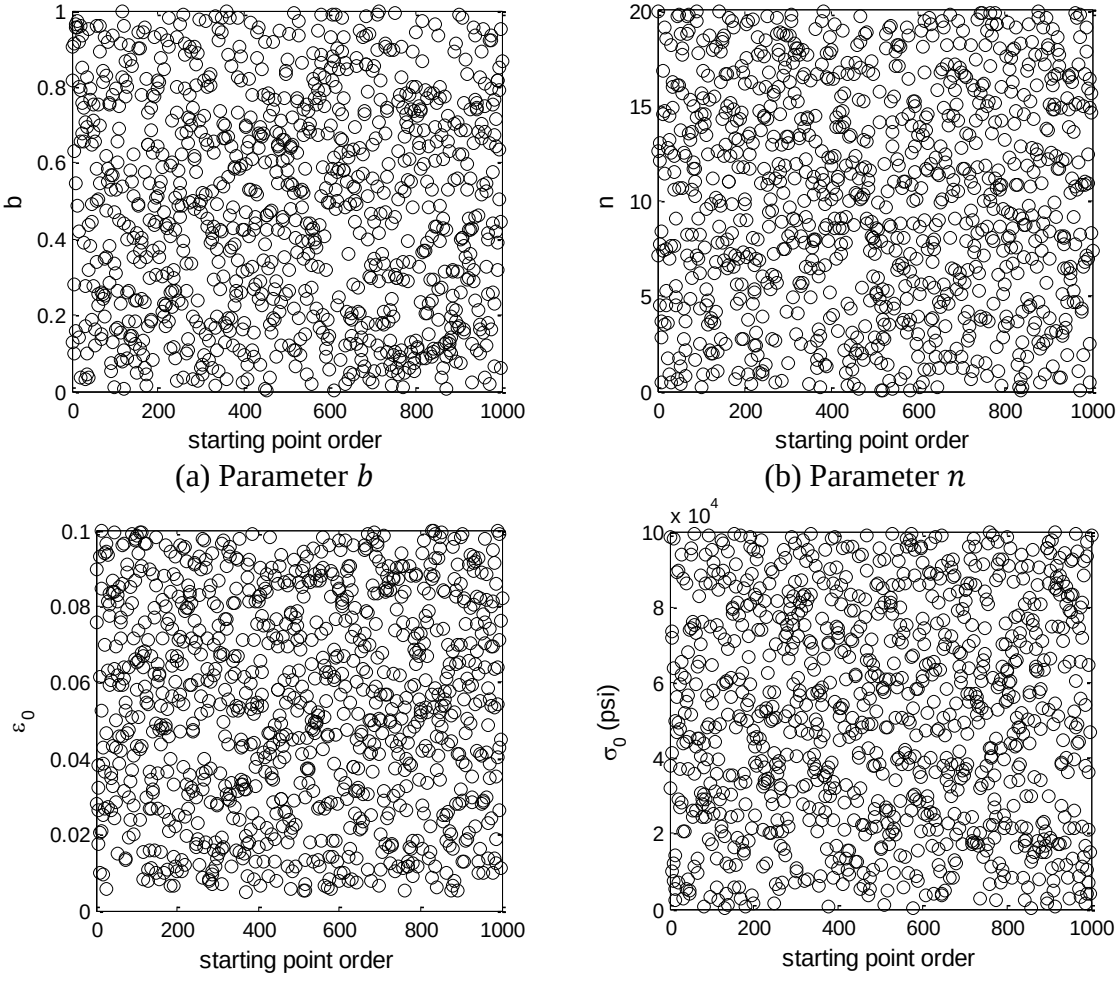

(a) Parameter b (b) Parameter n

(c) Parameter ε_0 (d) Parameter σ_0

Fig. 4.12. 1000 starting points for updating substrate constitutive model along CMD

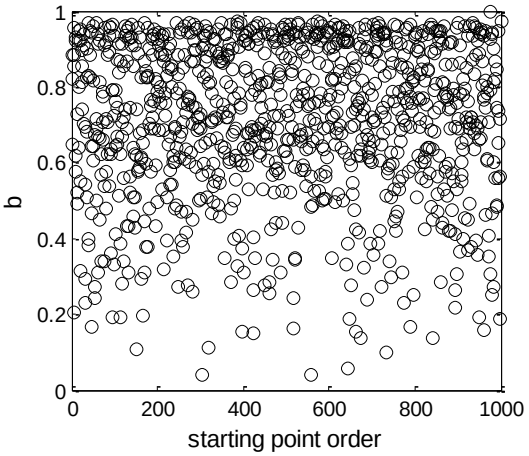

(a) Parameter b

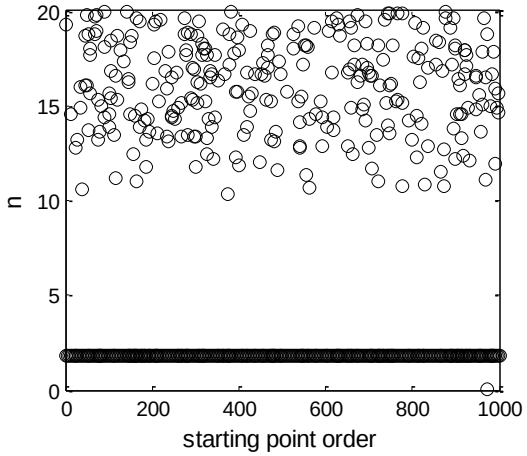

(b) Parameter n

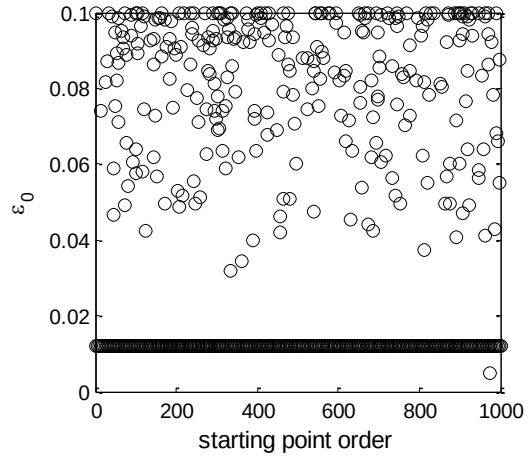

(c) Parameter ε_0

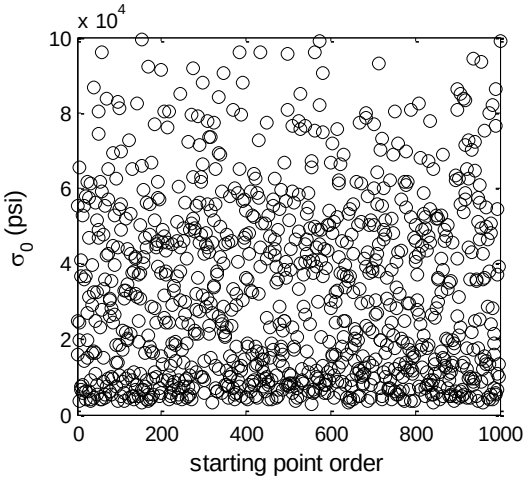

(d) Parameter σ_0

Fig. 4.13. Optimized points for updating substrate constitutive model along CMD

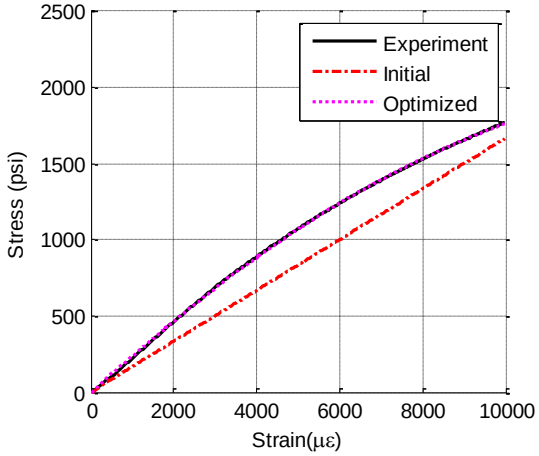

Fig. 4.14. Updating results substrate along CMD (stress-strain curve)

While updating the Menegotto-Pinto model for the copper updating, the initial values of the updating variables are defined as:

$$\mathbf{x_0^{Cu}} = [b, n, \varepsilon_0, \sigma_0] = [0.046, \quad 3.0, \quad 0.02, \quad 15{,}000(\text{psi})] \tag{4.12}$$

Lower and upper bounds of parameters are set as:

$$\mathbf{x_L^{Cu}} = [0.0, \quad 0.0001, \quad 0.005, \quad 15{,}000 * 0.1] \tag{4.13}$$

$$\mathbf{x_U^{Cu}} = [1.0, 20, \quad 0.1, \quad 15{,}000 * 10] \tag{4.14}$$

The 1,000 sets of search starting values are as shown in Fig. 4.15. Optimized parameters are shown in Fig. 4.16. Most of parameter n and ε_0 converge to 1.8011 and 0.0024, respectively. Most of optimized values for parameter b and σ_0 are around 0.7 and 50,000, respectively; however, these two optimized values do not have clear convergence as parameter n and ε_0. Finally, the smallest objective function value among the 1,000 solutions is 1.231×10^5 and corresponding optimized parameters are:

$$\mathbf{x^{Cu^*}} = [0.71, \quad 1.8011, \quad 0.0024, \quad 52{,}733] \tag{4.15}$$

Fig. 4.17 plots stress strain relation of the experimental, initial, and optimized results. After model updating procedure, the numerical model matches well with the experimental result.

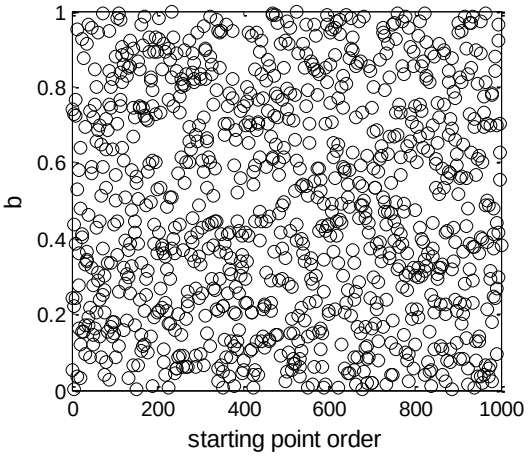

(a) Parameter b

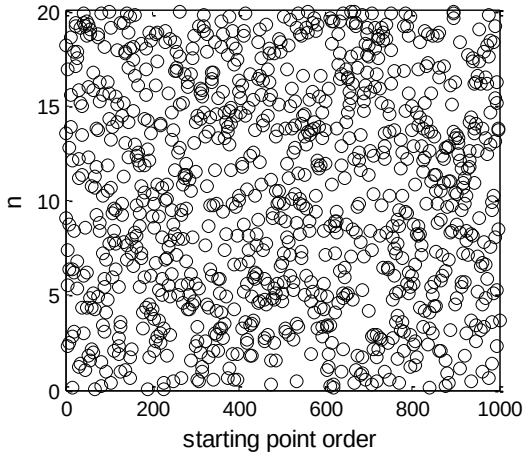

(b) Parameter n

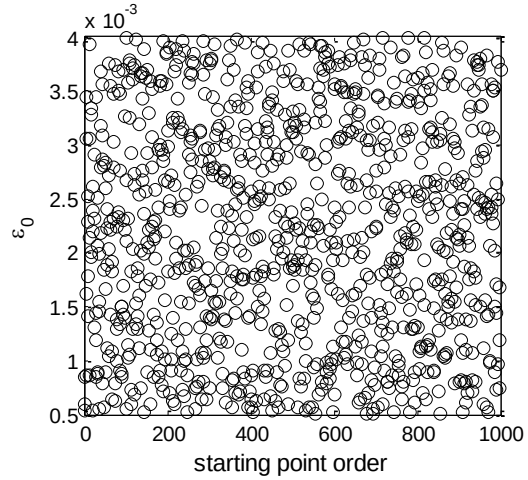

(c) Parameter ε_0

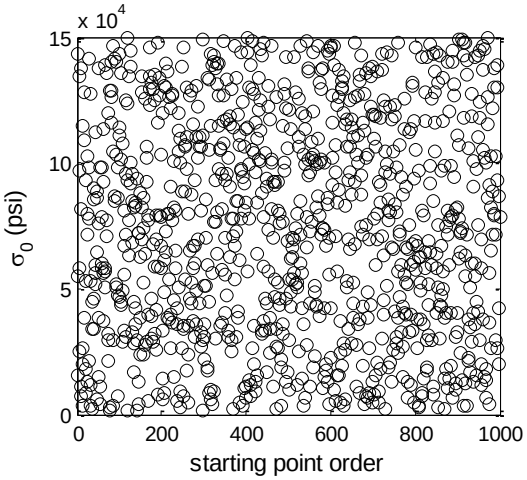

(d) Parameter σ_0

Fig. 4.15. 1000 starting points for updating copper constitutive model

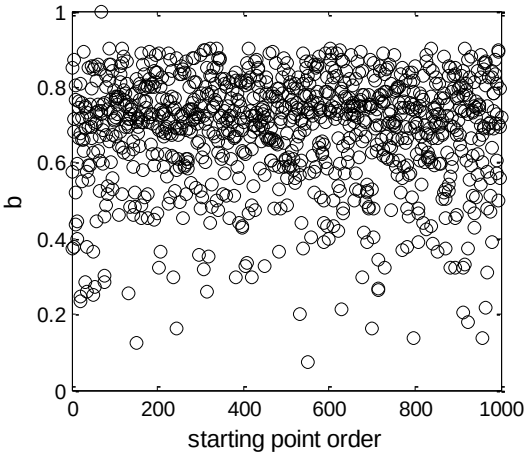

(a) Parameter b

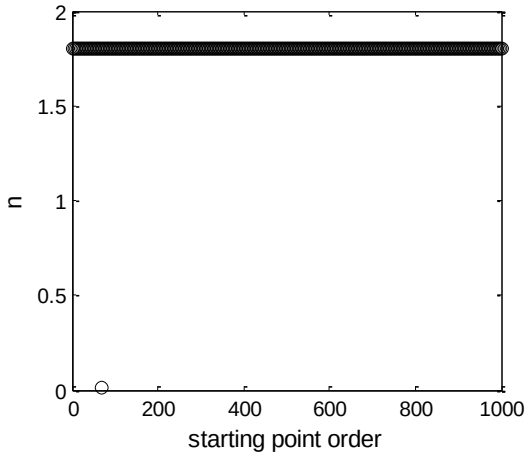

(b) Parameter n

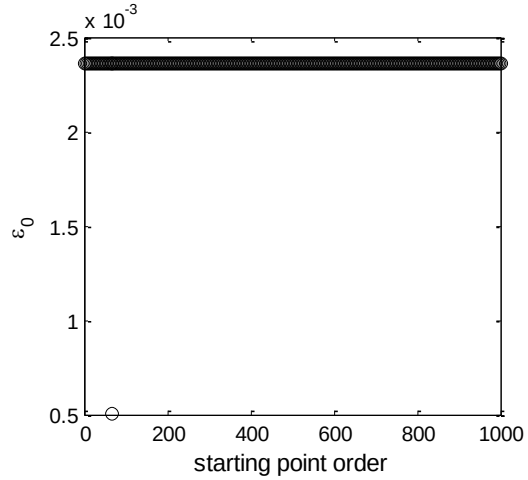

(c) Parameter ε_0

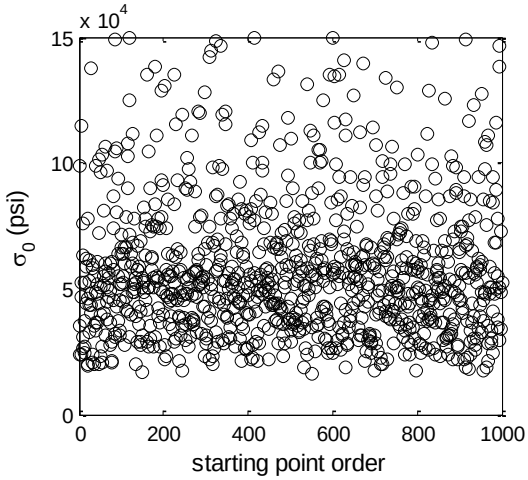

(d) Parameter σ_0

Fig. 4.16. Optimized points for updating copper constitutive model

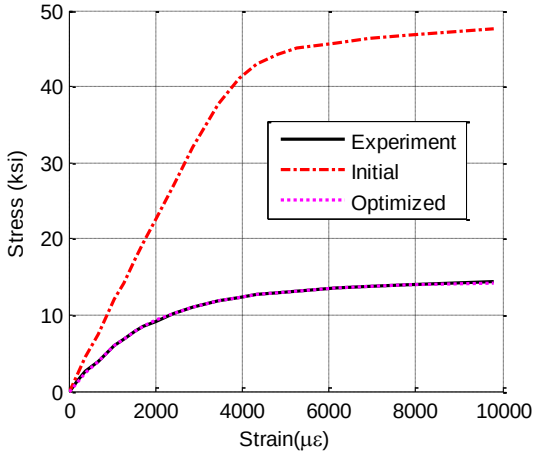

Fig. 4.17. Updating results copper (stress-strain curve)

For updating the aluminum constitutive model, the initial values of the updating variables are set as:

$$\mathbf{x_0^{Al}} = [b, n, \varepsilon_0, \sigma_0] = [0.04, \quad 8.0, \quad 0.004, \quad 45{,}000] \tag{4.16}$$

Lower and upper bounds of parameters are set as:

$$\mathbf{x_L^{Al}} = [0.0, \quad 0.0001, \quad 0.003, \quad 45{,}000 * 0.1] \tag{4.17}$$

$$\mathbf{x_U^{Al}} = [1.0, \quad 20, \quad 0.005, \quad 45{,}000 * 10] \tag{4.18}$$

The 1,000 sets of search starting values are randomly generated in Fig. 4.18. Optimized parameters are shown in Fig. 4.19. Most of optimized values for parameter b, n, ε_0 and σ_0 converge to:

$$\mathbf{x^{Al^*}} = [2.25 \times 10^{-14}, \quad 5.0741, \quad 0.0043, \quad 43{,}856] \tag{4.19}$$

And the smallest objective function value is 380,580. Fig. 4.20 plots stress strain relation of the experimental, initial, optimized results. After model updating procedure, the numerical model matches well with the experimental result.

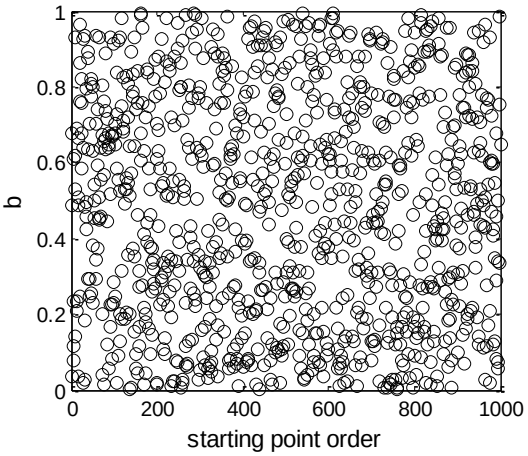

(a) Parameter b

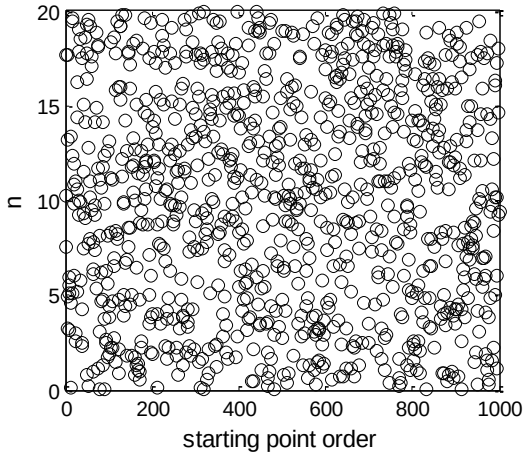

(b) Parameter n

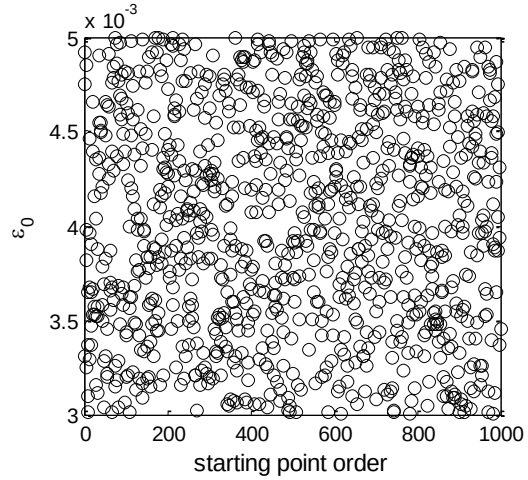

(c) Parameter ε_0

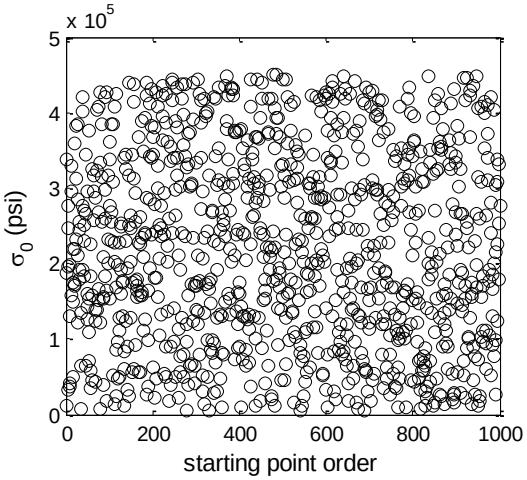

(d) Parameter σ_0

Fig. 4.18. 1000 starting points for updating aluminum constitutive model

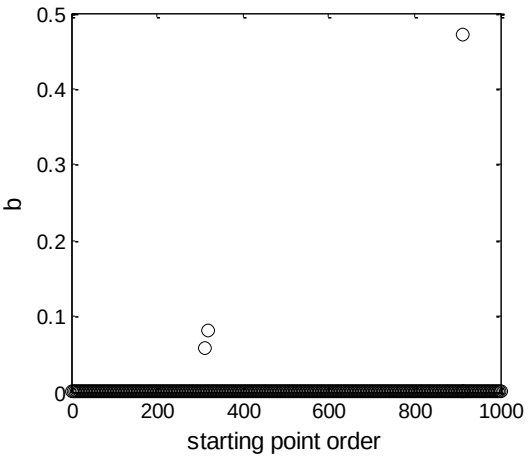

(a) Parameter b

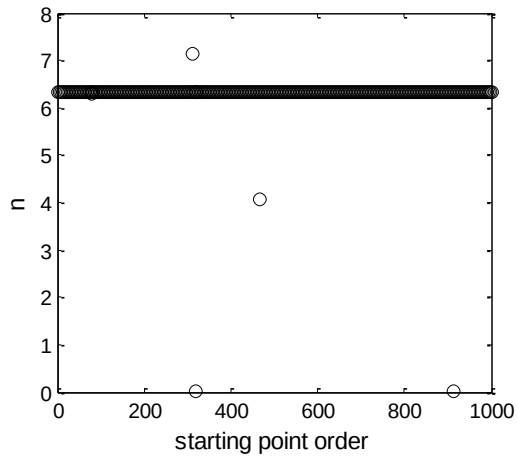

(b) Parameter n

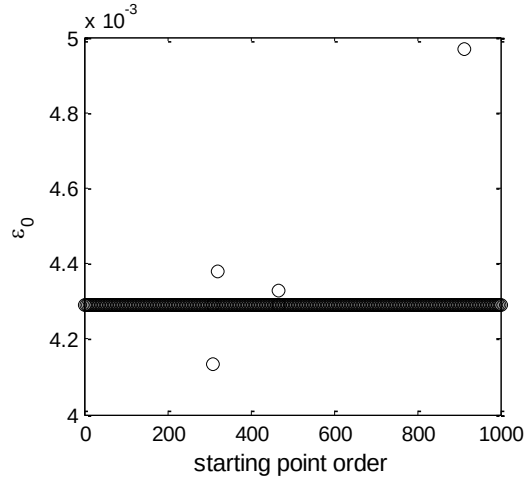

(c) Parameter ε_0

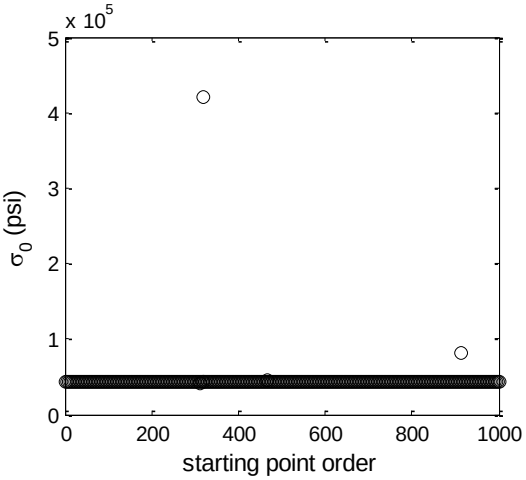

(d) Parameter σ_0

Fig. 4.19. Optimized points for updating aluminum constitutive model

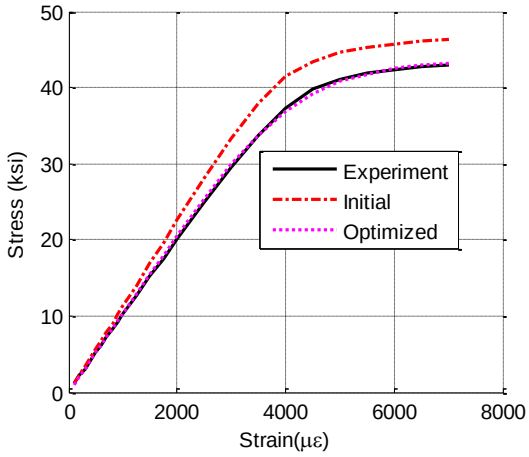

Fig. 4.20. Updating results for aluminum (stress-strain curve)

4.1.3.2 Shear modulus of the adhesive

To reduce the discrepancy in strain transfer ratio between numerical solution and the experimental result, the shear modulus updating of the adhesive is conducted. The updated constitutive models are implemented into a COMSOL FE model, in order to improve the accuracy of the numerical model (Fig. 4.21). As previously described, zero-length springs are used to model the sheer behavior of the adhesive between the substrate patch and the aluminum specimen, in order to describe the strain transfer effect.

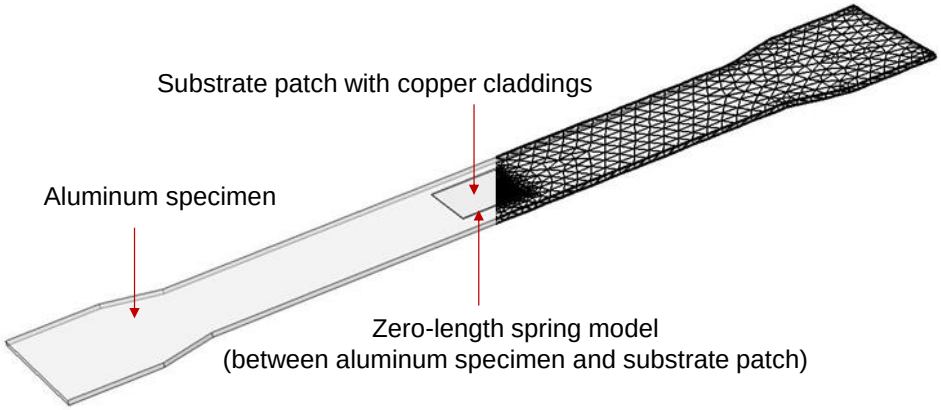

Fig. 4.21. FE model for strain transfer ratio

The optimization method for model updating is formulated as:

$$\underset{\mathbf{x}}{\text{minimize}} \sum_{i=1}^{m} \left[\mathrm{T}_{\mathrm{Exp}}(\varepsilon_i) - \mathrm{T}_{\mathrm{FEM}}(\varepsilon_i, \mathbf{x}) \right]^2 \tag{4.20}$$

$$\text{subject to } \mathbf{x}_{\mathrm{L}} \leq \mathbf{x} \leq \mathbf{x}_{\mathrm{U}}$$

where m is the number of strain steps; ε_i is strain level at i^{th} step; $\mathrm{T}_{\mathrm{Exp}}(\varepsilon_i)$ is strain transfer ratio at strain step ε_i from the experiment; $\mathrm{T}_{\mathrm{FEM}}(\varepsilon_i, \mathbf{x})$ is transfer ratio at strain step ε_i from the COMSOL FE model; $\mathbf{x}(= [b, n, \varepsilon_0, \tau_0])$ is updating parameters for the zero-length spring model; $\mathbf{x}_{\mathrm{L}}$ and $\mathbf{x}_{\mathrm{U}}$ are lower and upper bounds. The initial values of the updating variables are defined as:

$$\mathbf{x_0^G} = [b, n, \varepsilon_0, \tau_0] = [0.17, \quad 5.0, \quad 0.06, \quad 2{,}000(\text{psi})] \tag{4.21}$$

Lower and upper bounds of parameters are set as:

$$\mathbf{x_L^G} = [0.0, \quad 0.0, \quad 0.001, \quad 1{,}200] \tag{4.22}$$

$$\mathbf{x_U^G} = [0.6, \quad 20, \quad 0.006, \quad 3{,}500] \tag{4.23}$$

`The MultiStart` setup is the same as the previous section except that the number of starting points is reduced to 600 in Fig. 4.22.

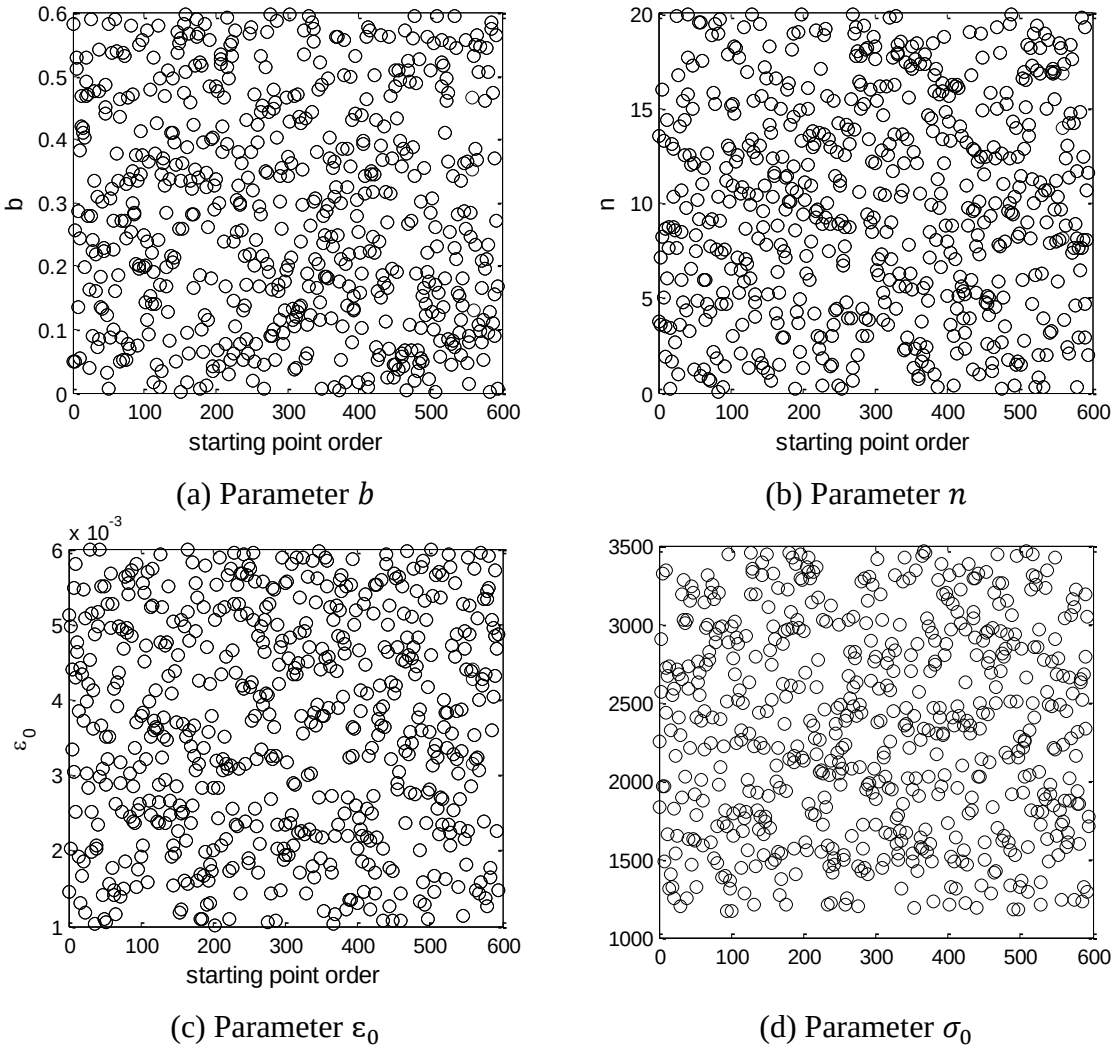

(a) Parameter b (b) Parameter n

(c) Parameter ε_0 (d) Parameter σ_0

Fig. 4.22. 600 starting points for adhesive model updating

Optimized parameters are plotted in Fig. 4.23. Optimized values of parameter b do not show clear trends although some of them are clouded around 0.25. After the 250th starting point, optimized values of parameter n show a tendency to be close to 2.5. Many optimized values of parameter ε_0 are in the range between 0.0025 and 0.0028. For the parameter σ_0, many optimized points are close to 2,300. Fig. 4.24(a) plots the objective function values; Fig. 4.24(b) plots closed-up view to show the smallest values. Although the 253th local solution ($\mathbf{x}^{253} = [0.12,\ 2.59,\ 0.027,\ 2870]$) show the smallest objective function values, the parameter values are away from most concentrations. Finally, the 324th local solution is selected as a global solution and the optimized parameters are:

$$\mathbf{x}^* = [0.2773, \quad 2.5875, \quad 0.0027, \quad 2{,}673] \tag{4.24}$$

Fig. 4.24 (c) shows the model updating results. While the numerical model with initial parameters shows the different strain transfer ratios from the experimental result, the updated model well matches with experimental data.

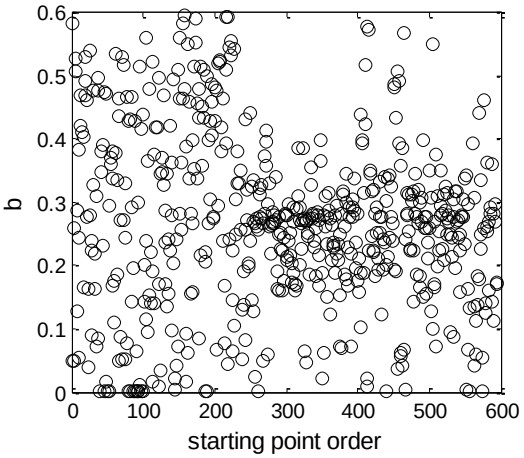

(a) Parameter b

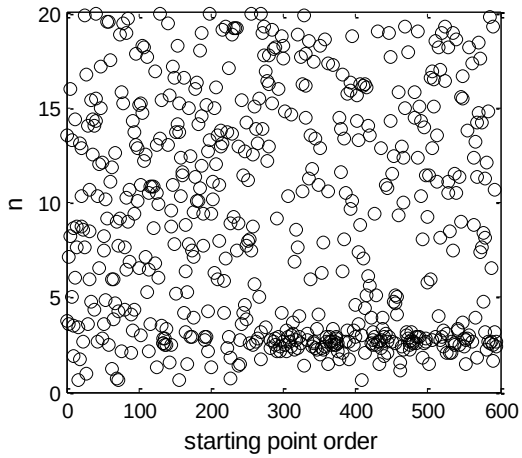

(b) Parameter n

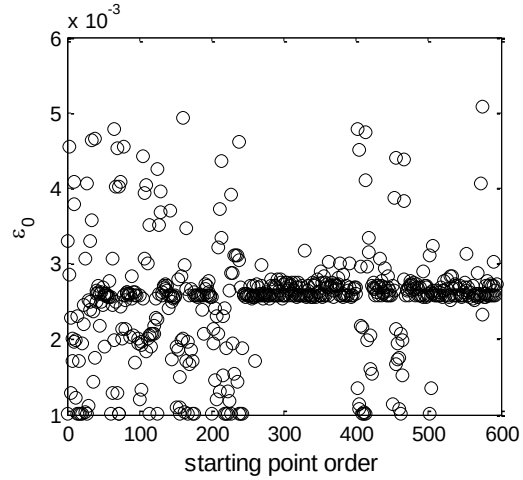

(c) Parameter ε_0

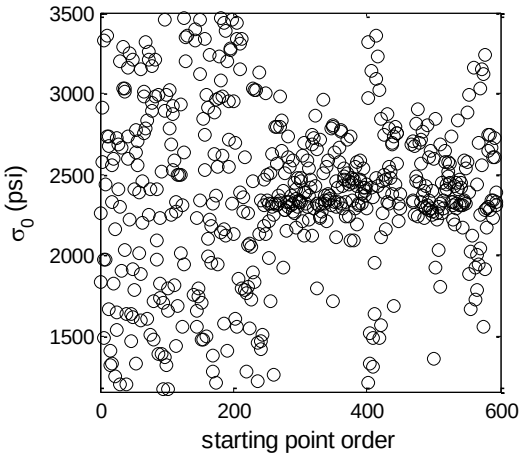

(d) Parameter σ_0

Fig. 4.23. Optimized points for adhesive model updating

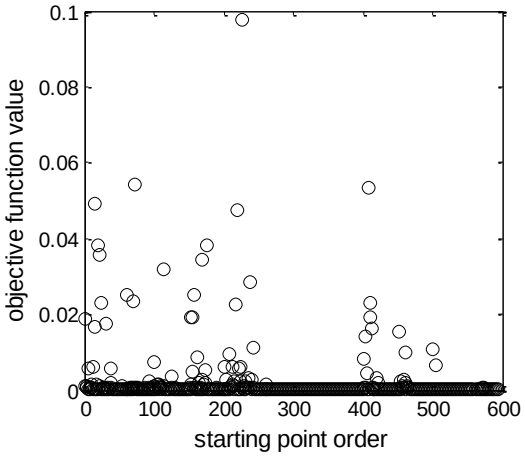

(a) Objective function values for each starting point

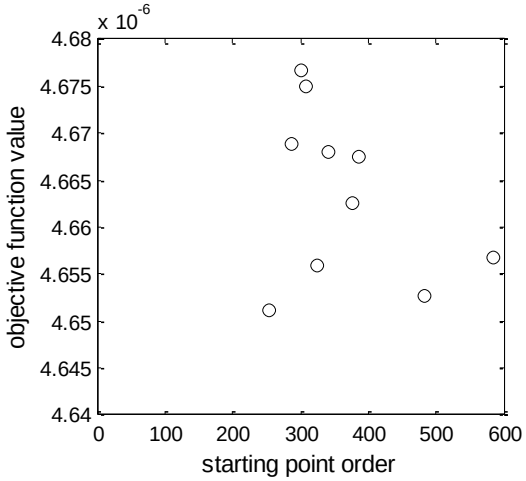

(b) close up for Fig. 4.24(a)

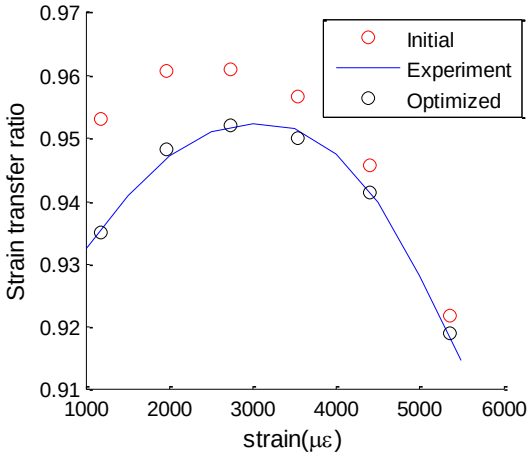

(c) Strain transfer ratio

Fig. 4.24. Updating results for adhesive model

4.2 Electromagnetic Parameter Updating

The dielectric constant of the antenna substrate is one of the key parameters determining the resonance frequency of an antenna sensor (Eq. (2.1)). In Section 4.2.1, a 950 MHz transmission-line resonator is designed and the tensile test of the resonator is conducted to investigate the dielectric constant change under strain. Section 4.2.2 describes a dielectric constant model that can describe strain effect. The dielectric constant model is then built into an optimization problem for model updating. Section 4.2.3 presents the model updating process and results.

4.2.1 Experimental Investigation

To investigate the variation of dielectric constant caused by strain effect, a 950MHz transmission-line resonator (Fig. 4.25) is designed based on the ASTM standard D3380-10 [51]. The resonator consists of top microstrip copper lines which are separated from the bottom copper ground plane by the 31-mil Rogers RT/duroid®5880 substrate. The 950 MHz resonance frequency requires the length of the center microstrip line to be 112mm. The resonance frequency can be experimentally measured by identifying the peak of the transmission coefficient (S_{21}) curve:

$$S_{21}(f) = \frac{V_2^{\mathrm{Out}}(f)}{V_1^{\mathrm{Input}}(f)} \tag{4.25}$$

where V_1^{Input} is the incident voltage from Port 1 at certain frequency f; V_2^{Out} is the output voltage from Port 2 at the same electromagnetic frequency as the input frequency f.

Given constant input power, the maximum output power is transferred from Port 1 to Port 2 at resonance frequency. The peak of the S_{21} curve of the transmission-line resonator corresponds to the resonance frequency of the resonator.

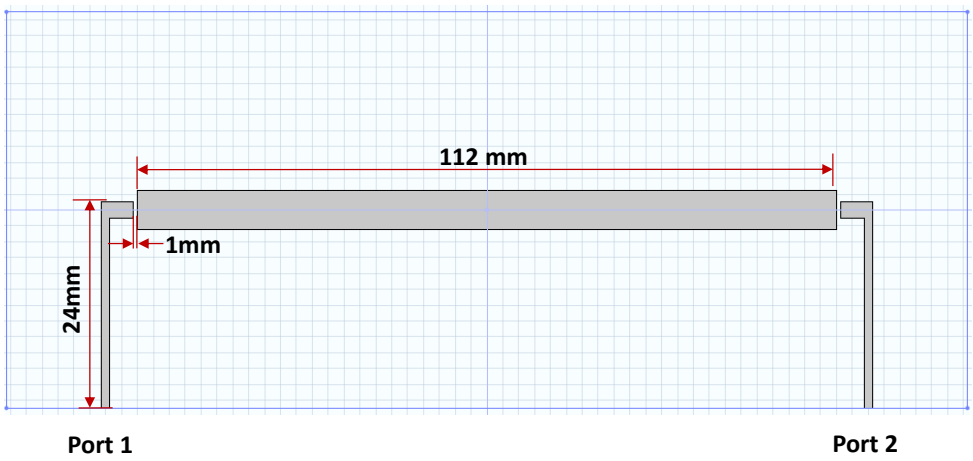

Fig. 4.25. Transmission line design

To characterize strain effect on dielectric constant change, a tensile test for the transmission-line resonator is conducted. Experimental setup is shown in Fig. 4.26. Three strain gages are installed on the aluminum specimen and other four strain gages are installed on the substrate (Fig. 4.26(a)). A National Instruments strain gage module (NI 9235), with a CompactDAQ Chassis (NI cDAQ-9172), is used for collecting data from metal foil strain gages. The axial force is applied by the MTS 810 testing machine (Fig. 4.26(b)). Two ports of the transmission-line resonator are connected to an Agilent Technologies Professional Network Analyzer (N5222A) to measure the S_{21} parameter curve. A 100με strain increment is achieved at each loading step till 6,000 με. For clarity, S_{21} curves with only seven strain levels are plotted in Fig. 4.27(a). The resonance frequency (the maximum peak point) clearly shifts towards left as strain increases. The resonance frequency at each strain level is extracted from the S_{21} plot and linear regression is performed to construct the resonance frequency versus strain plot (Fig. 4.27(b)). The coefficient of determination is found to be 0.9999 and the strain sensitivity of the transmission-line resonator is -752Hz/με.

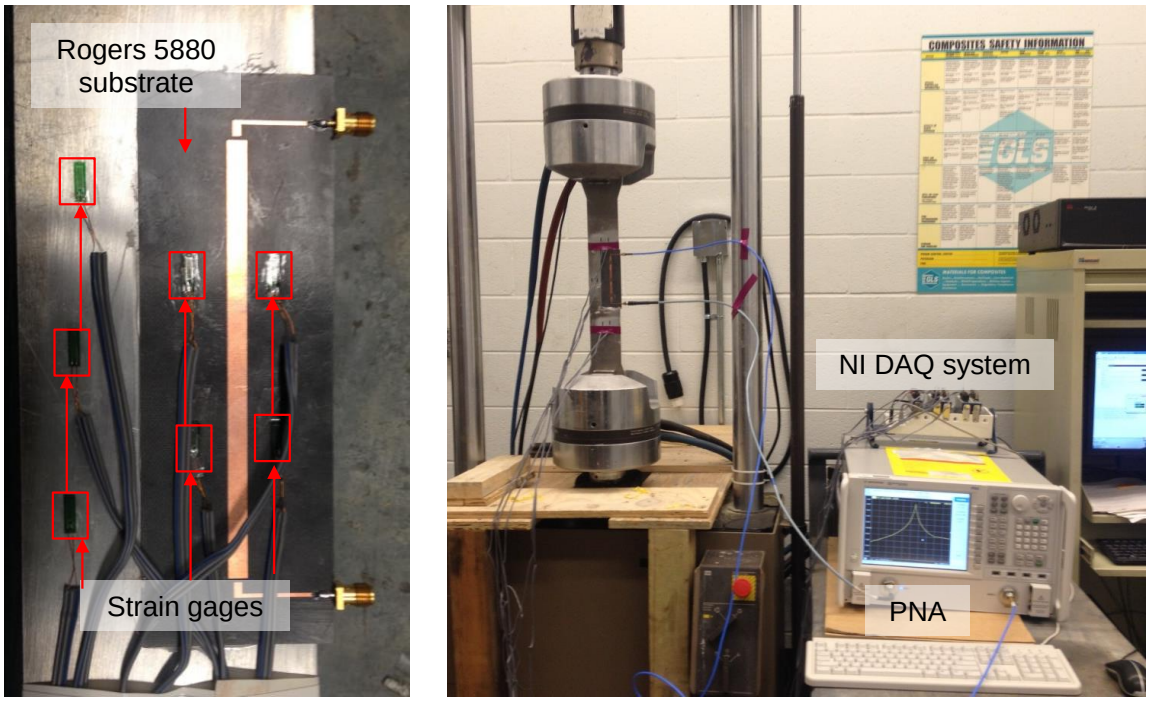

(a) Specimen configuration (b) Experimental setup

Fig. 4.26. Experimental setup for transmission line test

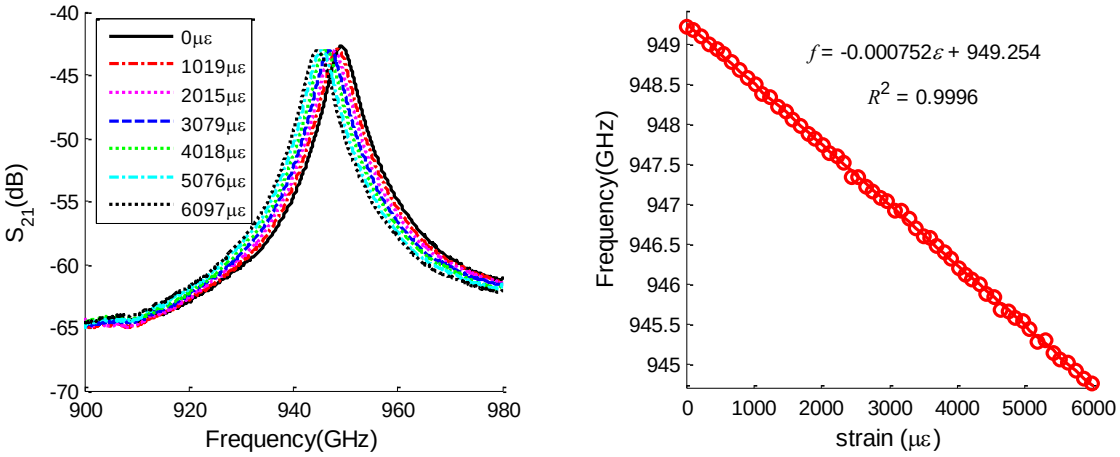

(a) S_{21} curve (b) Resonance frequency versus strain plot

Fig. 4.27. Test results

4.2.2 Dielectric Constant Modeling

Electrostriction is defined as the variation of the dielectric properties of a material under strain [52]. When the length of an antenna sensor increases with tensile strain, the

value of dielectric constant usually decreases. A multi-physics model should consider the electrostriction effect, in order to perform accurate antenna simulation under large strain. The relation between dielectric constant and strain can be expressed by a second-order dielectric tensor [53, 54].

$$\beta_{ij} = \beta_0 \delta_{ij} + \alpha_1 \varepsilon_{ij} + \alpha_2 \varepsilon_{kk} \delta_{ij} \tag{4.26}$$

Where β_0 is an initial value of dielectric constant value at zero strain; δ_{ij} is the Kronecker delta; ε_{ij} is strain tensor; α_1 and α_2 are electrostriction parameters. These two parameters will be updated in the model updating process. Their initial values can be estimated by the Shkel and Klingenberg's equations [55].

$$\alpha_1 = -\frac{2}{5}(\beta_0 - 1)^2 \tag{4.27}$$

$$\alpha_2 = -\frac{1}{3}(\beta_0 - 1)(\beta_0 + 2) + \frac{2}{15}(\beta_0 - 1)^2 \tag{4.28}$$

Fig. 4.28 illustrates a multi-physics COMSOL model for dielectric constant model updating. The updated mechanical properties of aluminum plate, substrate, copper, and glue from previous Section 4.1 are implemented into the multi-physics FE model. The substrate model with the second-order dielectric tensor (Eq. (4.26)) describes electrostriction effect.

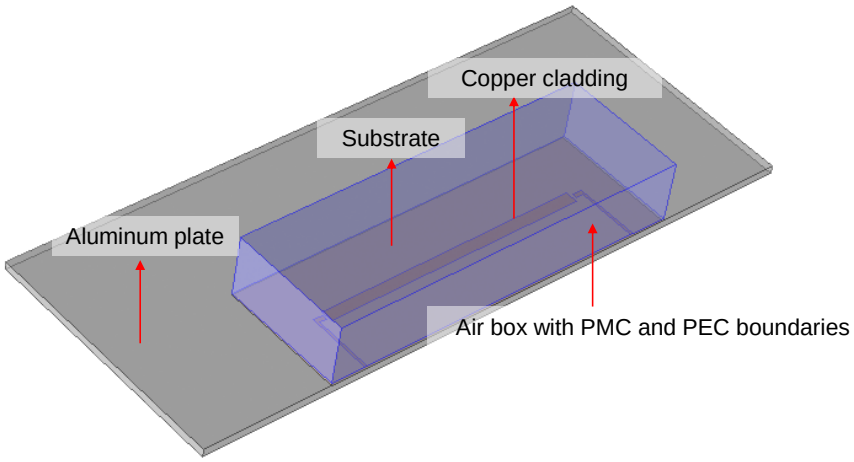

Fig. 4.28. Illustration of multi-physics COMSOL model for dielectric constant model updating

4.2.3 Model Updating Procedure and Result

The objective of dielectric constant model updating is to reduce discrepancy of electrostriction effects between experiment and numerical solution. The model updating formulation through two optimization values $\boldsymbol{\alpha} = [\alpha_1,\ \alpha_2]$ is:

$$\underset{\boldsymbol{\alpha}}{\text{minimize}} \sum_{i=1}^{m} \left[f_{\text{Exp}}(\varepsilon_i) - f_{\text{FEM}}(\varepsilon_i, \boldsymbol{\alpha}) \right]^2 \tag{4.29}$$

$$\text{subject to } \boldsymbol{\alpha}_{\text{L}} \leq \boldsymbol{\alpha} \leq \boldsymbol{\alpha}_{\text{U}}$$

where m is the number of strain steps; ε_i is strain level at i-th step; $f_{\text{Exp}}(\varepsilon_i)$ is normalized resonance frequency at ε_i from an experiment; $f_{\text{FEM}}(\varepsilon_i, \boldsymbol{\alpha})$ is the normalized resonance frequency at ε_i from the COMSOL multi-physics simulation in the previous section; $\boldsymbol{\alpha}_{\text{L}}$ and $\boldsymbol{\alpha}_{\text{U}}$ are lower and upper bounds of the updating vector parameter $\boldsymbol{\alpha}$.

Although dielectric constant β_0 of Rogers 5880 at zero strain is 2.2 from datasheet, this value causes resonance frequency difference between experiment (949.22 MHz) and simulation (943.55MHz). To reduce the discrepancy, initial dielectric constant β_0 is updated to 2.1708.

In this model updating, the same global optimization setup is adopted as Section 4.1.3. The initial parameters calculated from Eq.(4.27) and (4.28) are defined as:

$$\boldsymbol{\alpha_0} = [-0.5483, \quad -1.445] \tag{4.30}$$

Lower and upper bounds are estimated from trial and error and their ranges are set as:

$$\boldsymbol{\alpha_L} = [-1, \quad -2.5] \tag{4.31}$$

$$\boldsymbol{\alpha_U} = [-0.2, \quad -0.5] \tag{4.32}$$

As shown in Fig. 4.29, 80 trial starting points are randomly generated. The corresponding optimized solutions are shown in Fig. 4.30. All optimized values for parameter α_1 and α_2 converge to:

$$\boldsymbol{\alpha}^* = [-0.41081, \quad -1.92280] \tag{4.33}$$

Fig. 4.31 shows the updating results. When the effect of dielectric constant change under strain is neglected, the discrepancy between experimental and simulated resonance frequencies is clear. Although the Shkel and Klingenberg's equations (initial parameters) describe dielectric constant change under strain, model updating results gave the best match between experiment and simulation.

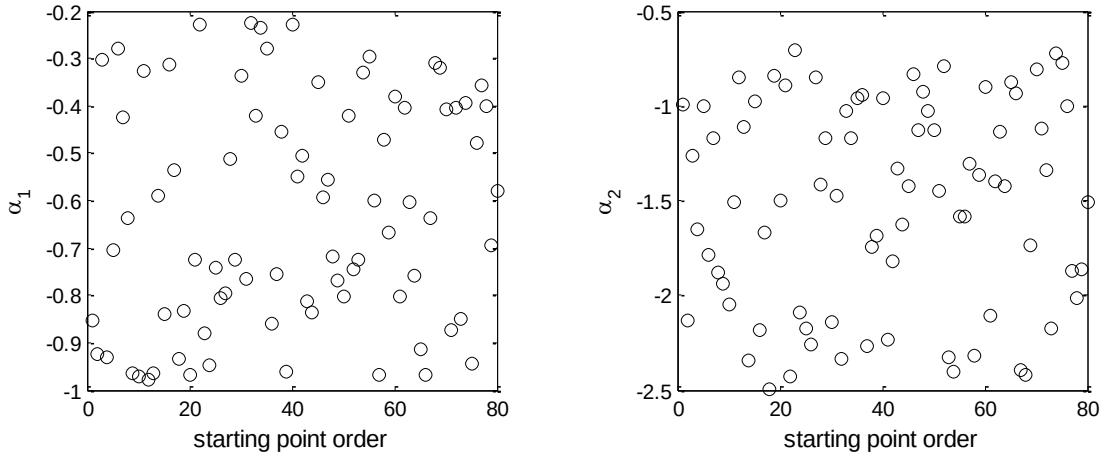

(a) Parameter a_1 (b) Parameter a_2

Fig. 4.29. 80 starting points for updating dielectric constant model

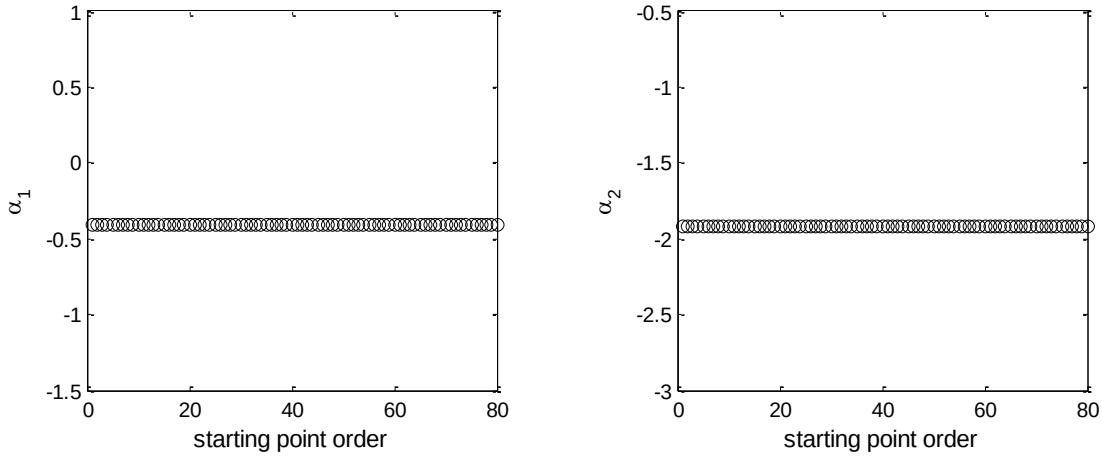

(a) Parameter a_1 (b) Parameter a_2

Fig. 4.30. Optimized points for updating dielectric constant model

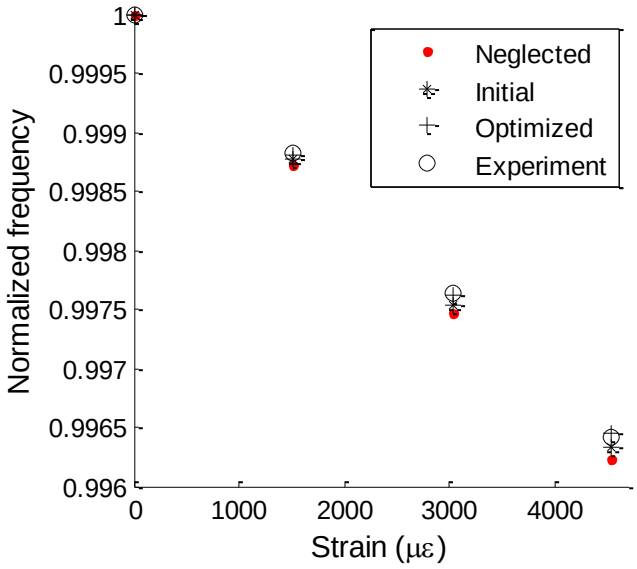

Fig. 4.31. Updating results for adhesive shear modulus updating

4.3 Summary

This chapter describes mechanical and electromagnetic parameters updating. To investigate the mechanical and electromagnetic properties under strain, nonlinear tensile tests are conducted. The Menegotto-Pinto and zero-length spring models are introduced to characterize the constitutive relation in mechanical domain. A second-order dielectric tensor is used to describe the relationship between dielectric constant and strain. The mechanical and electromagnetic models are implemented to multi-physics FE model. Model updating is shown to reduce the discrepancy between the numerical and experimental results. Finally, an accurate multi-physics FE model is achieved using the updated model parameters. Using the updated FE model, design optimization of the antenna sensors will be described in the next chapter.

CHAPTER 5 FRAMEWORK FOR SYSTEMATIC OPTIMIZATION OF ANTENNA SENSOR DESIGN

Although passive (battery-free) RFID antenna sensors have shown promising performance for strain sensing, the sensor design was mostly manually optimized by experience [5, 7]. Building on the improved simulation efficiency and updated FE model parameters as described in previous two chapters, a framework to automatically optimize sensor design is proposed in this chapter.

Performance of antenna stain sensors is evaluated by major two indexes, strain sensitivity and radiation gain. While the strain sensitivity defines resonance frequency changes due to strain, radiation gain determines possible wireless interrogation distance. To simultaneously optimize these two performance indexes, a multi-objective optimization problem is formulated.

The rest of this chapter is organized as follows. Section 5.1 describes the design optimization framework with two objectives, strain sensitivity and antenna gain. Section 5.2 validates the optimization framework with an example of a slotted patch antenna strain sensor. Performance of the initial design is compared with the optimized design. The results are summarized and discussed in Section 5.3.

5.1 Design Optimization Framework

The objective of sensor design optimization is to improve strain sensitivity and the radiation gain, both of which are mainly dependent on the pattern of the top copper layer. Geometry parameters of the copper pattern are chosen as optimization variables. For example, Fig. 5.1 shows that geometry vector **x** of a slotted patch antenna as the design valuables.

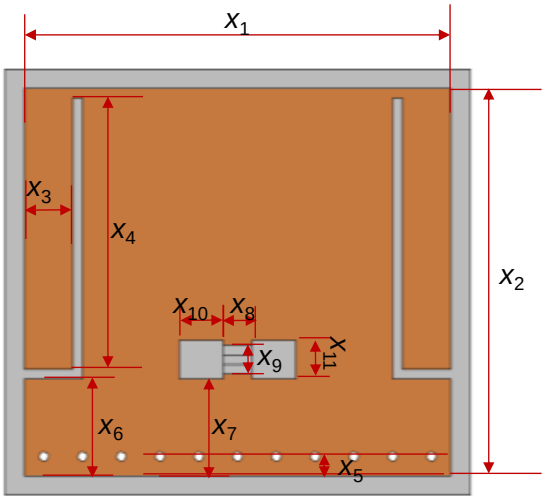

$\mathbf{x} = [x_1, x_2, \cdots, x_{11}]$

Fig. 5.1. Examples geometry parameters for a slotted patch antenna sensor

To obtain strain sensitivity value of an antenna design, a partially air-filled cavity model is created by COMSOL. Static mechanics simulation is performed according to prescribed strain levels. At each strain level, eigenfrequency of the deformed antenna is calculated. Experience shows the simulated coefficient of determination between resonance frequencies and strains is very close to 1.0 (Fig. 3.6(b)). Therefore, eigenfrequencies at only two strain steps (zero and 3,000με) are calculated to define strain sensitivity.

To obtain radiation gain, a full-wave model is created for a frequency domain solution. The partially air-filled cavity model is not used because it cannot perform far-field analysis needed to calculate radiation. As mentioned in Section 3.1.4, the full-wave model with the frequency domain solver is time-consuming when S_{11} is required at multiple frequency points. However, since the gain simulation is only needed at one frequency point (corresponding to the eigenfrequency), computational load is not as significant as in Section 3.1.4. In addition, the radiation gain changes very little due to strain and thus is why needed at 0με. Finally, the multi-objective optimization method is formulated as:

$$\underset{\mathbf{x}}{\text{maximize}}\ [-(1-\lambda)S(\mathbf{x}) + \lambda G(\mathbf{x})] \tag{5.1}$$

$$\text{subject to}\ \mathbf{x}_{\mathrm{L}} \le \mathbf{x} \le \mathbf{x}_{\mathrm{U}}$$

where $\mathbf{x}$ is the geometry vector containing optimization variables; $\mathbf{x}_{\mathrm{L}}$ and $\mathbf{x}_{\mathrm{U}}$ are lower and upper bounds for $\mathbf{x}$; $\lambda \in [0, 1]$ is the regularization parameter which balances the weighting between strain sensitivity and gain; $S(\mathbf{x})$ is the strain sensitivity which is the slope between two resonance frequencies at different strain level (0 and 3,000$\mu\varepsilon$) from COMSOL. The algebraic sign of strain sensitivity $S(\mathbf{x})$ is always negative, because resonance frequency decreases when the sensor is in tension. $G(\mathbf{x})$ is radiation gain generated by COMSOL. The COMSOL−MATLAB framework for optimizing sensor design is illustrated in Fig. 5.2.

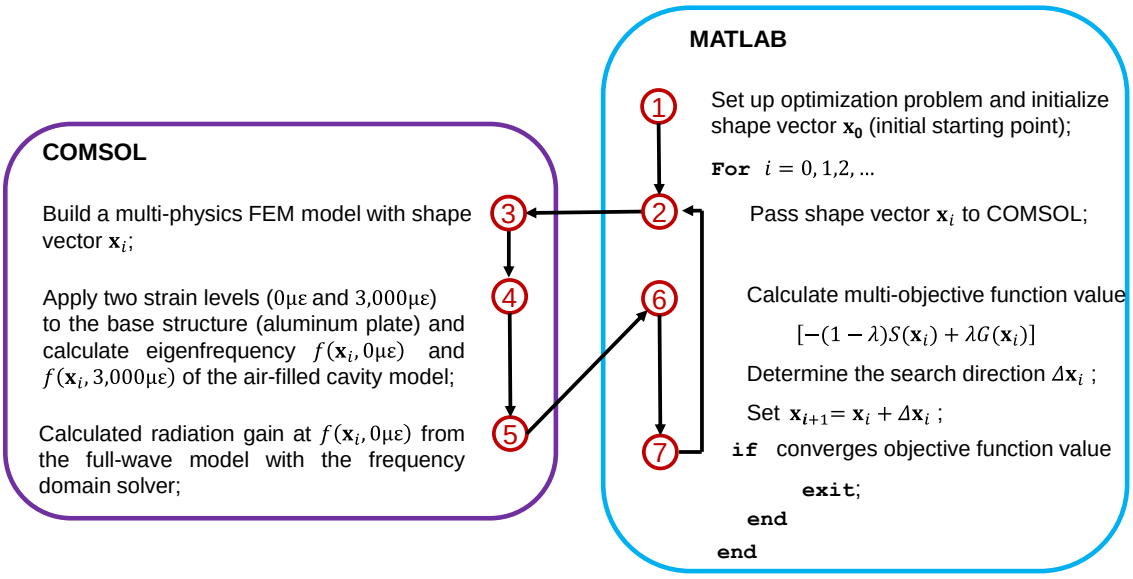

Fig. 5.2. Optimization procedure of antenna sensor

5.2 Validation Example

In order to validate the proposed the design optimization of antenna sensors, an RFID slotted patch antenna is investigated as an example. Section 5.2.1 describes the numerical optimization procedure to obtain an optimized design by the framework. Section 5.2.2 presents experimental validation for the optimized design.

5.2.1 Slotted Patch Antenna Optimization

In the design optimization of the slotted patch antenna sensor, the geometry vector **x** is as show in Fig. 5.1. The initial parameters $\mathbf{x}_0$ are chosen as [7]:

$$\mathbf{x}_0 = [44, 40, 6, 29, 2, 10, 10, 3, 3, 16, 0.4\ ]\text{mm} \tag{5.2}$$

Constrained by the substrate size, the lower and upper bounds are set as:

$$\mathbf{x}_\text{L} = [37, 30, 2, 10, 1.5, 4, 5, 2, 2, 12, 0.1]\text{mm} \tag{5.3}$$

$$\mathbf{x}_\text{U} = [50, 50, 15, 45, 3, 20, 30, 5, 5, 18, 4]\text{mm} \tag{5.4}$$

Most MATLAB optimization functions are programmed to find a minimum objective function value. In order to conveniently implement the multi-objective formulation into the MATLAB `fmincon`(Finding minimum of constrained nonlinear multivariable function) with interior-point algorithm, the maximization problem in Eq. (5.1) should be modified. In addition, because strain sensitivity $S(\mathbf{x})$ and radiation gain $G(\mathbf{x})$ have different orders of magnitude, some scaling is added to the new formulation below.

$$\underset{\mathbf{x}}{\text{minimize}}\ [(1-\lambda)f_1(\mathbf{x}) + \lambda f_2(\mathbf{x})] \tag{5.5}$$

$$\text{subject to}\ \mathbf{x}_\text{L} \le \mathbf{x} \le \mathbf{x}_\text{U}$$

where

$$f_1(\mathbf{x}) = \frac{S(\mathbf{x})}{1{,}000} \tag{5.6}$$

$$f_2(\mathbf{x}) = -10^{G(\mathbf{x})/10} \tag{5.7}$$

Because the strain sensitivity amplitude of the slotted patch is lower than 1,000, Eq. (5.6) defines $f_1(\mathbf{x})$ to have a range between –1.0 and 0. On the other hand, a gain value of the slotted patch antenna $G(\mathbf{x})$ is usually between –10 to 0dB. Eq. (5.7) defines $f_2(\mathbf{x})$ that converts from logarithmic-dB scale to a number between –1.0 and 0.

To find appropriate regularization parameter λ, the value λ is assigned from 0.0 to 1.0 with 0.1 step size. At every step, 10 trial starting geometry vectors are randomly generated by `MultiStart`. The `fmincon` optimization MATLAB toolbox finds a local optimum around each starting point, and the best among 10 solutions is chosen for that λ value. Fig. 5.3 presents optimal trade-off curve between $f_1(\mathbf{x})$ (strain sensitivity) and $f_2(\mathbf{x})$ (radiation gain). For both axes, smaller values mean better performance.

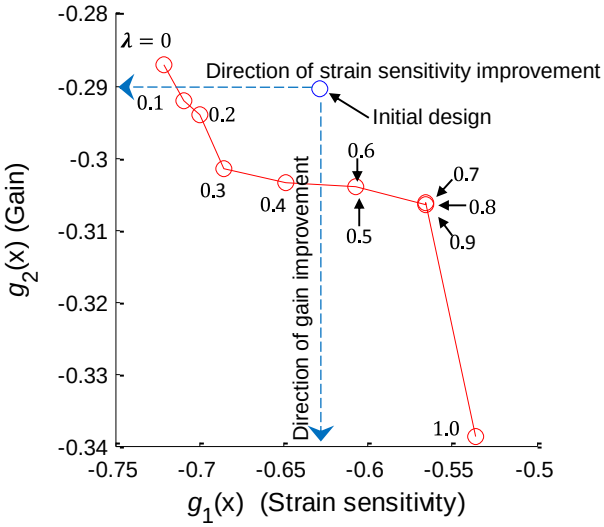

Fig. 5.3. Optimal trade-off curve (L-curve) between $f_1(\mathbf{x})$ and $f_2(\mathbf{x})$ changed values by Eq. (5.6) and (5.7)

The point of initial design is also plotted, and shown to be far from the optimal trade-off curve. Values of $f_1(\mathbf{x})$ and $f_2(\mathbf{x})$ from the initial design are –0.6288 and –0.2904 (corresponding strain sensitivity of –624.84Hz/με and gain of –5.37dB). When the regularization parameter λ is 0.0, the amplitude of strain sensitivity is maximized and the values of $f_1(\mathbf{x})$ and $f_2(\mathbf{x})$ are –0.7207 and –0.2872, respectively (–720.76Hz/με and –5.41dB). On the contrary, when the regularization parameter λ is 1.0, the gain is maximized to be –4.70dB. The corresponding values of $f_1(\mathbf{x})$ and $f_2(\mathbf{x})$ are – 0.5361 and – 0.3385, respectively and the strain sensitivity becomes –536.06Hz/με. The solution

point λ=0.3 is regarded as the "best", because L-curve slope is suddenly changed here and $f_2(\mathbf{x})$ is not sensitive anymore after $\lambda > 0.3$. The geometry parameter values are:

$$\mathbf{x}^* = [41.67, 45.51, 2.49, 25.11, 4.01, 5.22, 4.99, 8.53, 13.17, 2.46] \quad (5.8)$$

At this optimized shape, the strain sensitivity is –685Hz/με and the radiation gain is –5.16dB. Fig. 5.4 shows the alteration of the total dimension and the top copper pattern after optimization process. Fig. 5.5 shows the frequency domain solution for the optimized sensor. The resonance frequency is 913.7MHz based on the S_{11}.

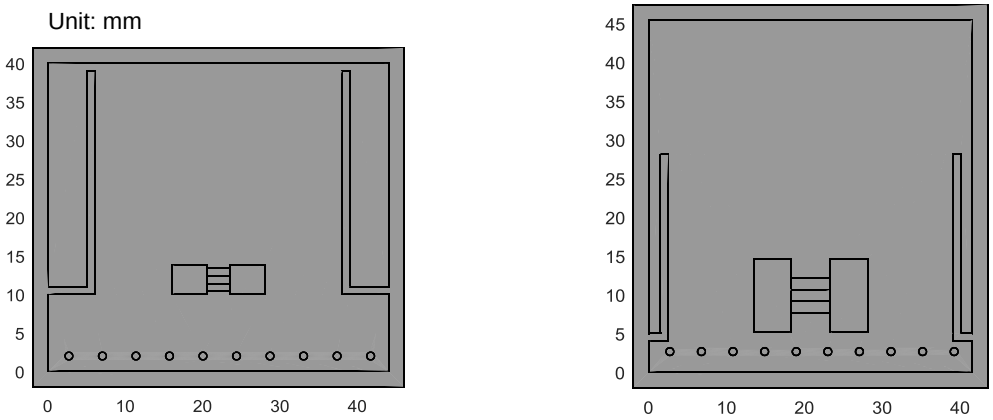

(a) Initial design (b) Optimized design

Fig. 5.4. The design optimization result for the slotted patch antenna

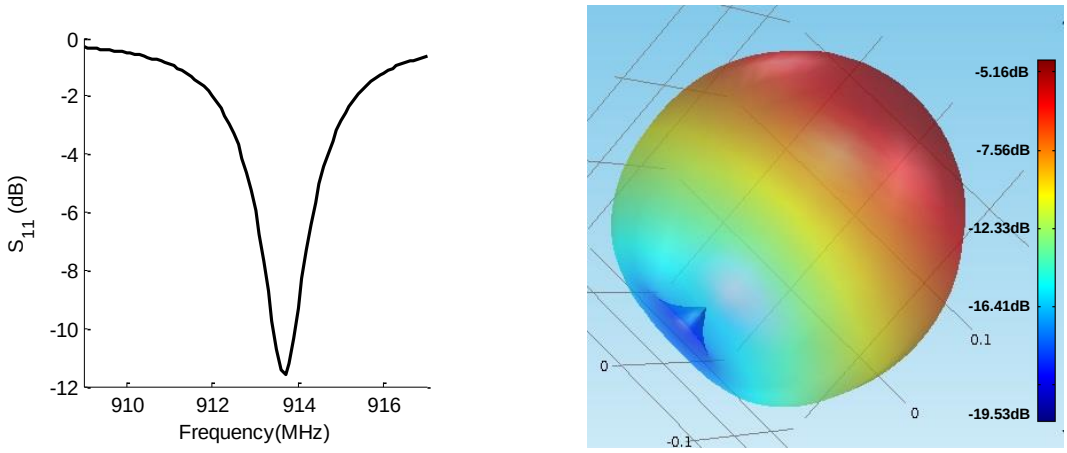

(a) S_{11}curve (b) Gain pattern

Fig. 5.5. Frequency domain solution of optimized sensor

5.2.2 Experimental Validation

In order to validate strain sensing performance of the optimized slotted patch antenna sensor, a tensile test is conducted. The optimized sensor is bonded to the aluminum specimen by M-bond 610 adhesive (Vishay Precision Group, Inc.) (Fig. 5.6(a)). The aluminum specimen is mounted to the tensile testing setup with a 22-kip SATEC machine (Fig. 5.6(b)).

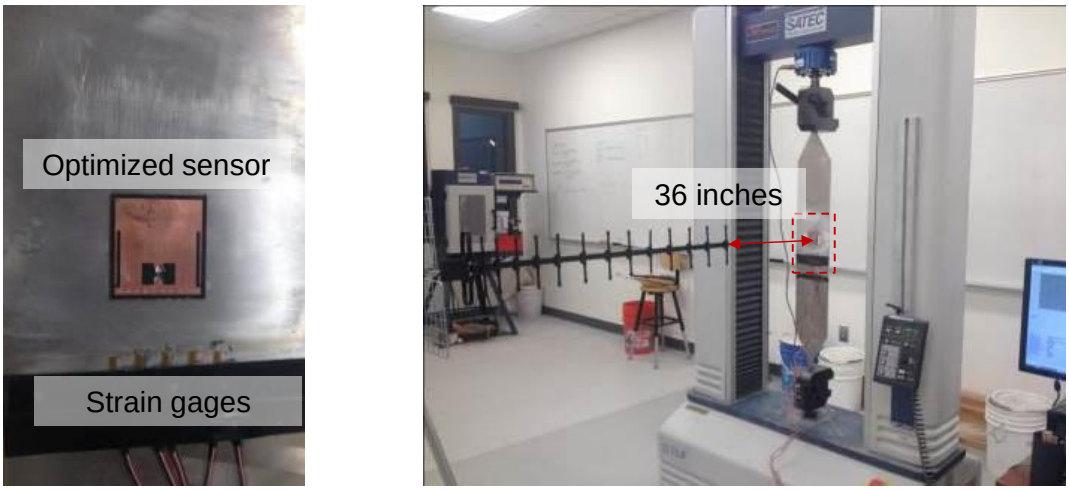

(a) Sensor configuration (b) Experimental setup

Fig. 5.6. Tensile test for the optimized sensor

Applied strain is from zero to 300με with a 50με step. At the reader side, an 18dBi Yagi antenna is located and interrogation distance is 36 inches. For clarity, only three strain levels of average transmitted power curves are plotted in Fig. 5.7(a). Since the valley area of the interrogation power threshold plot is relatively flat, a 4^{th} order polynomial curve fitting is performed to the valley area of each plot. The fitted 4^{th} order polynomial is used for identifying the resonance frequency that corresponds to the minimum power. After extracting the resonance frequency, the linear regression is performed as shown in Fig. 5.7(b). The measured strain sensitivity is –741Hz/με and the determination of the coefficient is 0.9690. The strain sensitivity in the optimized slotted patch antenna sensor is improved from the original design.

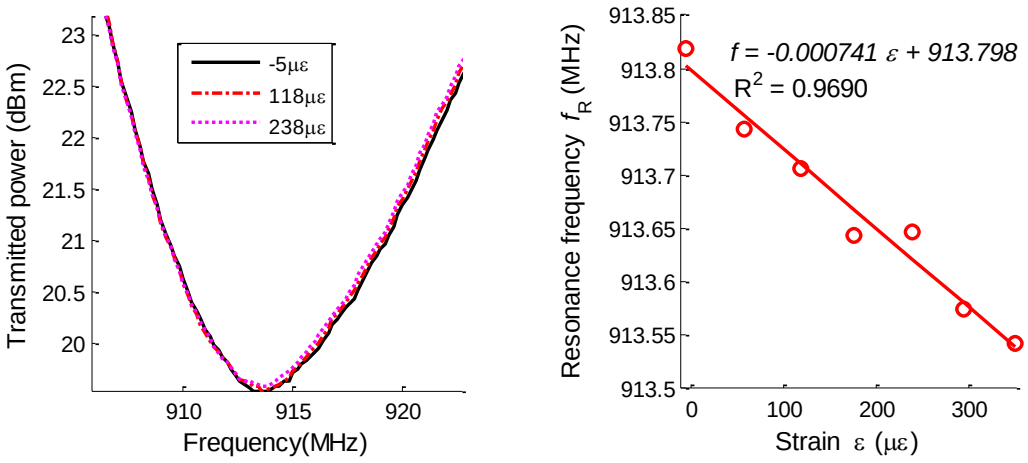

(a) Average transmitted power (b) Resonance frequency change versus strain

Fig. 5.7. Tensile test result for the optimized sensor

In order to validate the radiation-gain improvement, transmitted powers from two sensors (the original and the optimized design) are compared. The interrogation distance of the reader is set to 36 inches. Measured transmitted power curves are plotted in Fig. 5.8. While the minimum transmitted power required by the original design is around 20.8dBm, the optimized design needs only 19.5dBm around the resonance frequency. The optimized sensor reduces the required transmitted power level by 1.3dB. Since the interrogation process includes signal emitting and backscattering, the improved radiation gain of the antenna sensor is around 0.65dB.

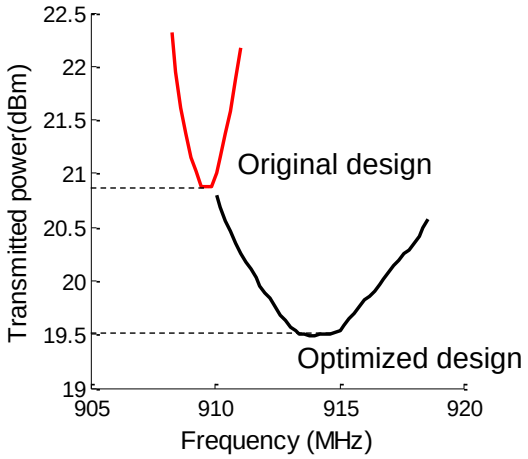

Fig. 5.8. Radiation gain test

5.3 Summary

This chapter proposes the design optimization framework for antenna sensors. Strain sensitivity and radiation gain are chosen to formulate a multi-objective optimization problem. As a validation example of the optimization framework, the slotted patch antenna sensor is investigated. To find optimal regulation parameter λ, the optimal trade-off curve between $f_1(\mathbf{x})$ (strain sensitivity) and $f_2(\mathbf{x})$ (antenna gain) is constructed and λ=0.3 is chosen as the "best" design. The optimized strain sensitivity and antenna gain are –685Hz/με and –5.37dB, respectively. Both indexes are improved compared with the original values of strain sensitivity and radiation gain. Through the experimental validation, the strain sensitivity is –741Hz/με and the radiation gain is improved as 0.65dB.

CHAPTER 6 FREQUENCY DOUBLING ANTENNA SENSOR

Current RFID antenna sensors have space for improvement for higher strain sensitivity and smaller footprint size. However, patch aspects are mainly limited by commercial off-the-shelf RFID chips with a fixed operating frequency around 900MHz [39]. First, the strain sensitivity (Hz/με) is approximately to the resonance frequency (MHz) of the antenna sensor. Second, the antenna resonance frequency is inversely proportional to the length of electrical path, which is relevant to sensor size. The dependency on 900MHz frequency range dictates that further sensitivity increased or size reduction are limited for RFID antenna sensors.

As an alternative way to modulate electromagnetic signal (instead of using RFID), this chapter introduces a frequency doubling technique to improve strain sensitivity and achieve size reduction. Operating at higher frequency range, the frequency doubling antenna sensor consists of three main components — a 2.4GHz receiving patch antenna, a matching network, and a 4.8GHz transmitting patch antenna. For interrogation, a wireless reader emits a 2.4GHz interrogation signal to the 2.4GHz receiving patch antenna of the antenna sensor. The matching network integrated with a Schottky diode then doubles the interrogation frequency of 2.4GHz to the backscattering frequency of 4.8GHz. The 4.8GHz transmitting patch antenna finally responds with the backscattered signal to the reader (Fig. 6.1).

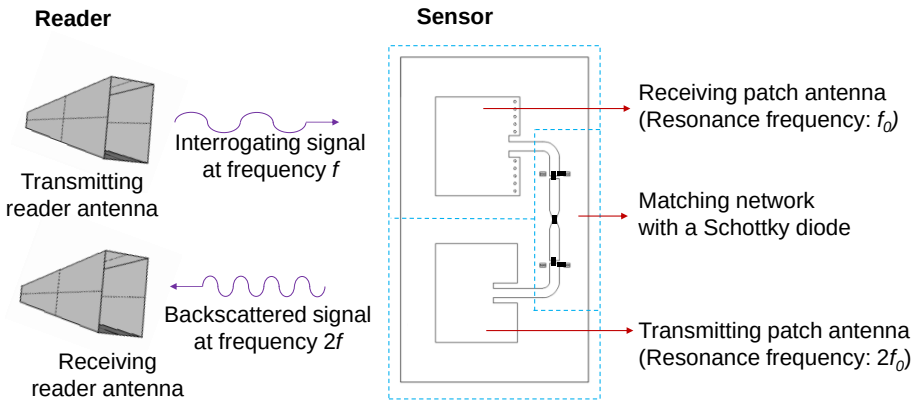

Fig. 6.1. Operation mechanism of a frequency doubling antenna sensor

Although the frequency doubling sensors operating at higher frequency have advantages over RFID sensors, the drawback of this system is difficult to distinguish between multiple antenna sensors. To this end, a wireless frequency doubling switch is proposed to avoid data-collision between of the frequency doubling sensors [56]. Between two ends of a Schottky diode, DC forward biasing voltage is wirelessly applied to eliminate the nonlinear electrical behavior of the diode, efficiently and selectively disabling the sensor. The wireless switch consists of a receiving patch antenna and an RF rectifier whose detailed operating mechanism will be introduced.

In this chapter, Section 6.1 describes the frequency doubling antenna sensor design, including the 2.4GHz receiving folded patch antenna, the 4.8GHz transmitting patch antenna, and the matching network. In Section 6.2, multi-physics simulation is conducted to evaluate the strain sensing performance. S_{11} scattering parameter simulation for the 2.4GHz receiving folded patch antenna and the 4.8GHz transmitting patch antenna are conducted by COMSOL. Advanced Design System (ADS) software package is used for harmonic balance simulation of the diode. Section 6.3 introduces the anti-data-collision method for the frequency doubling antenna sensor. The wireless switch design and the simulation are described. Section 6.4 presents experimental validations. Performance of a single frequency sensor is validated first, following by a sensor array test.

6.1 Design of Frequency Doubling Antenna Sensor

To design the receiving patch and the transmitting patch of the antenna sensor, COMSOL radiofrequency (RF) module is adopted. However, in order to simulate the nonlinear behavior of the frequency doubling matching network, the simulation software should support harmonic balance simulation. This is needed to characterize the second harmonic performance of the Schottky diode output, i.e. at a frequency twice of the incident frequency [57]. Because the AC/DC module in COMSOL does not support

harmonic balance simulation, ADS software package is adopted to design the matching network. Section 6.1.1 describes design of the receiving and transmitting patch antennas. Section 6.1.2 presents the matching network design.

6.1.1 Receiving and Transmitting Patch Antenna Designs

The Rogers 5880 substrate with 0.7874mm (31mil) thickness is used in patch antenna designs. As shown in Fig. 6.2(a), the planar dimension of a receiving patch antenna is 25.0mm × 21.1mm, operating at the 2.4GHz frequency range. To reduce patch antenna footprint, antenna folding technique is utilized through vias as Section 5.2. COMSOL simulation shows the scattering parameter of the receiving antenna named S_{11}^{R} is –13dB at 2.4GHz, as shown in Fig. 6.2 (b). This is lower than the required –10dB return loss threshold of a typical antenna, indicating high radiation efficiency.

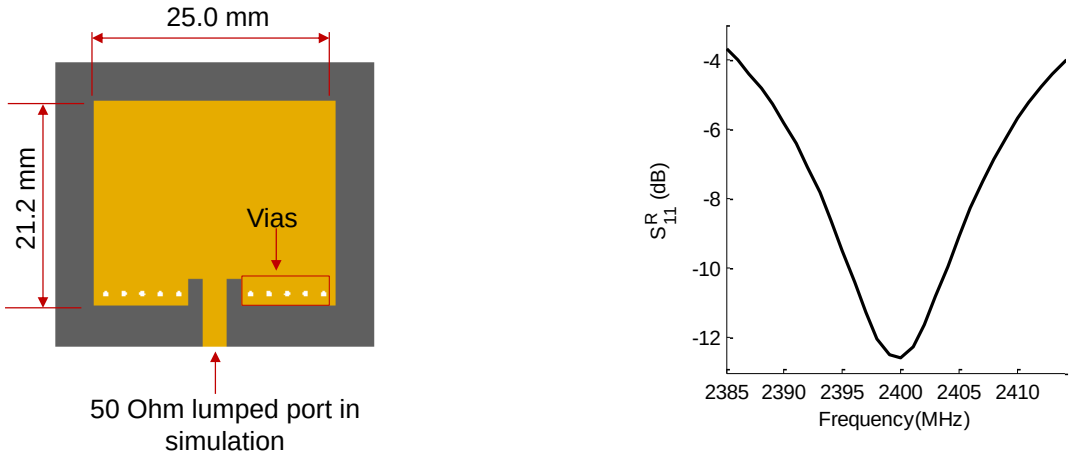

(a) Dimensions of the folded 2.4GHz receiving antenna

(b) Simulated S_{11}^{R} parameter

Fig. 6.2. Sensor-side receiving antenna design

Designed on the same substrate, dimension of the 4.8GHz transmitting patch antenna is 25.0mm × 20.6mm (Fig. 6.3(a)). As shown in Fig. 6.3(b), the simulated scattering parameter S_{11}^{T} is –15.5dB at 4.8GHz. This is twice the value of the receiving antenna's resonance frequency, and thus achieves frequency doubling.

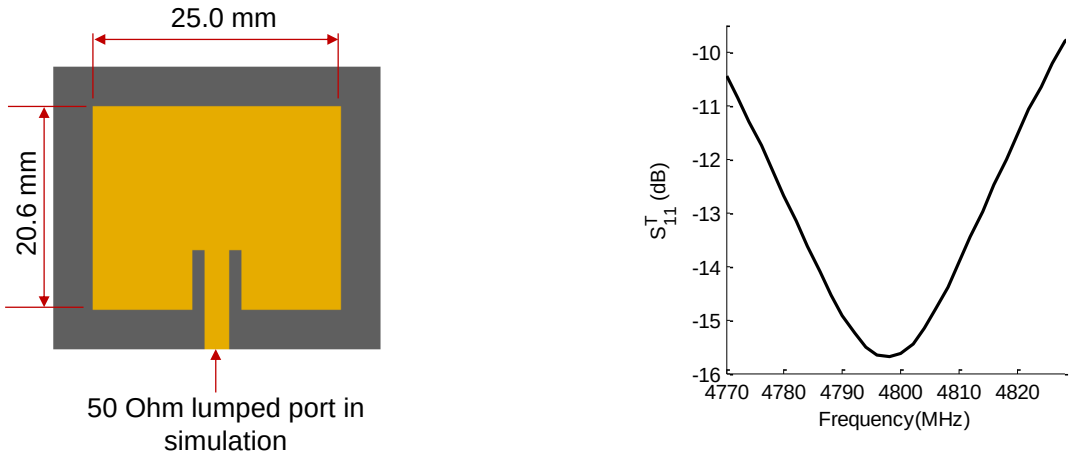

(a) Dimensions of the 4.8 GHz receiving antenna

(b) Simulated S_{11}^T parameter

Fig. 6.3. Sensor-side transmitting antenna design

6.1.2 Matching Network Design

Fig. 6.4(a) shows the matching network design. Input power with frequency *f* is from the 2.4 GHz receiving patch antenna connected to Port 1. Output power with doubled frequency 2*f* is transferred to Port 2 connected to the 4.8GHz transmitted patch antenna. The main goal of the matching network design is to maximize output power (at Port 2) upon frequency doubling. Discrete component matching technique is used between input and output of the diode. In order to match impedances between the diode and two patch antennas, a 3.2pF capacitor and a 4.7nH inductor are used at the input matching; an 1.0pF capacitor and an 1.0nH inductor are used in the output matching. The diode in the matching network, which is a two-terminal semiconductor device, offers a nonlinear relationship between excitation voltage and current. This nonlinearity produces the second harmonic wave (i.e. doubling frequency) at the output terminal. A Schottky diode (SMS7621-79LF, Skyworks Solutions, Inc.) is selected in this research due to its relatively low junction capacitance, allowing operation at high frequency. The overall

size of the matching network is 22.4mm × 59.6mm (Fig. 6.4(a)). To validate the design performance, the power loss due to diode-integrated matching network is investigated by a harmonic balance simulation in a commercial circuit simulation software package, ADS. The SPICE diode model is used to simulate the performance of the Schottky diode. Conversion gain is an index to show how matching network is well designed for frequency doubling. Conversion gain in the frequency doubling process is defined as:

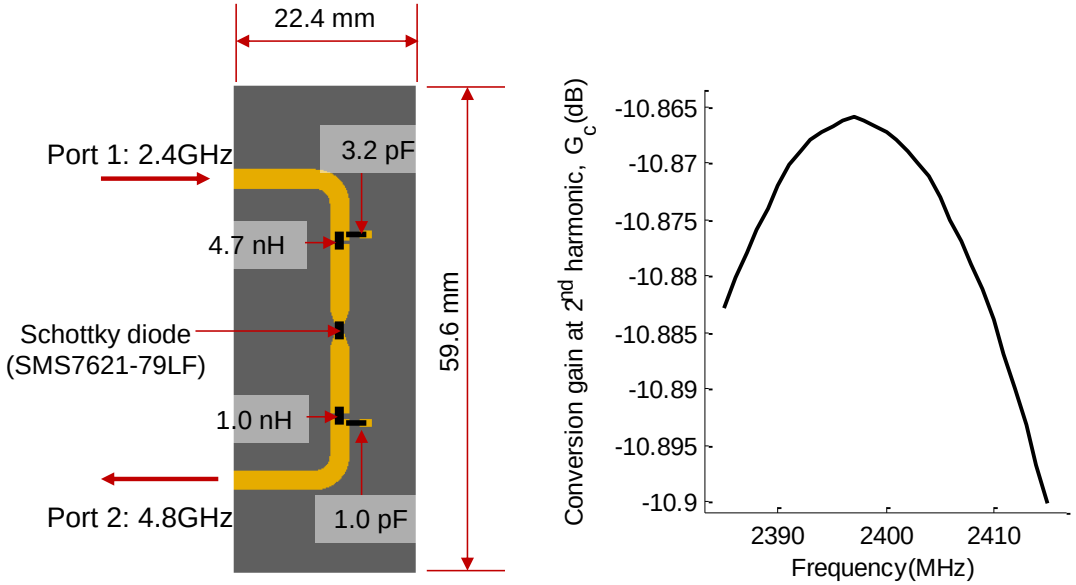

(a) Dimensions of matching network

(b) Simulated conversion gain at the 2nd harmonic, G_c with different input power levels

Fig. 6.4. Matching network design for a 2.4GHz to 4.8GHz frequency doubling antenna sensor

$$G_c = \frac{P_2}{P_1} \tag{6.1}$$

where P_1 is input power at frequency f to Port 1; P_2 is output power with doubled frequency $2f$ from Port 2 (Fig. 6.4 (a)).

In ADS simulation, the input power to Port 1 (P_1) in the matching network is set to –10dBm. The value is obtained from an experimental measurement by setting the reader interrogation power at 15dBm and the reader 12 in. away from the sensor. The

simulated conversion gain is plotted in Fig. 6.4(b). The gain is around –11 dB at the interrogation frequency band.

6.2 Multi-Physics Simulation for Characterizing Performance

A special three-step simulation is proposed in order to simulate strain sensing performance of the entire frequency doubling antenna sensor. Fig. 6.5 shows the flow chart of the three-step coupled simulation. The mechanical behavior of the 2.4GHz sensor-side receiving antenna under strain is first simulated in COMSOL. Electromagnetic simulation is then performed with the deformed antenna shape. The mechanical-electromagnetic coupled model simulates scattering parameters (S_{11}^{R}) of the 2.4GHz receiving antennas at different strain levels, in order to calculate corresponding power P_1, which serves as input power to the matching network at Port 1. The following simulation of the diode-integrated matching network in ADS then generates the output power P_2 at the doubled frequency. With output power P_2 from ADS simulation combined with the scattering parameter of the 4.8GHz transmitting patch antenna (S_{11}^{T}), one can calculate the power level P of the overall response signal backscattered from the sensor to the reader. Section 6.2.1 describes the mechanical-electromagnetic coupled simulation for the 2.4GHz receiving patch antenna at different strain levels. Section 6.2.2 introduces simulation setup and results for the matching network design. Section 6.2.3 presents backscattered signal from the 4.8GHz transmitting antenna.

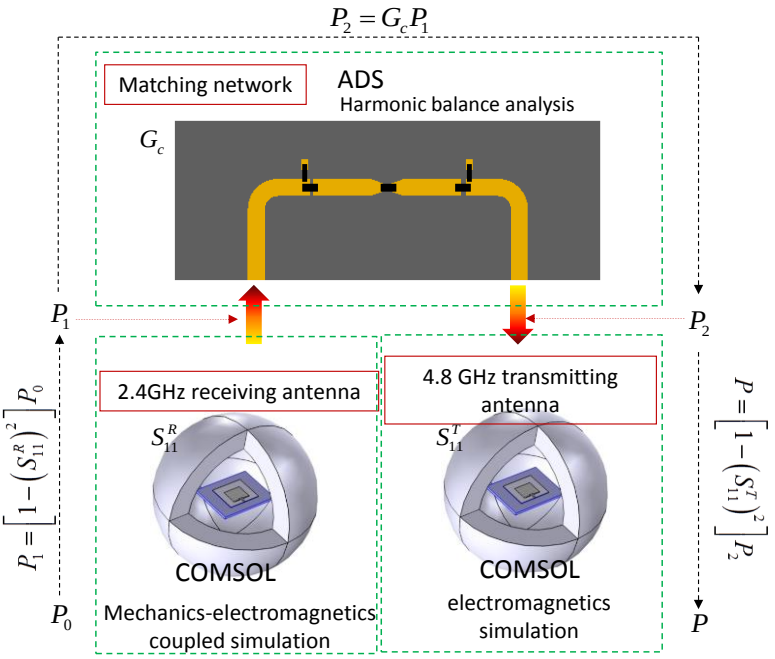

Fig. 6.5. Flow chart of the multi-physics coupled simulation for the entire sensor

6.2.1 Receiving 2.4GHz Patch Antenna

In this study, it is proposed that only the 2.4GHz receiving patch antenna is bonded on the structural surface, while other parts of the sensor (the matching network and the 4.8GHz patch antenna) are not. Therefore, the 2.4GHz sensor-side receiving antenna not only receives interrogation power from the reader, but also serves as the strain sensing element. While the 2.4GHz antenna experiences strain with structural surface, all other parts of the sensor are strain free. Therefore, a mechanical-electromagnetic coupled simulation is required for the 2.4GHz patch antenna model, in order to accurately describe the electromagnetic performance of the patch antenna under strain.

Fig. 6.6(a) shows the COMSOL mechanical-electromagnetic coupled simulation model of the 2.4GHz patch antenna. The 2.4GHz patch antenna, together with an aluminum plate, is placed in the center of an air sphere. Outside of the air sphere is the PML (perfectly matched layer). Updated material parameters from Chapter 4 are used in

the simulation. Different element types of the finite element model are adopted to better simulate the antenna structure. Table 6.1 lists the number of each type of elements, and the corresponding DOFs in COMSOL model.

To investigate the strain sensing capability of the sensor, prescribed displacements are applied to the two ends of the aluminum plate. Five strain levels are applied from zero to 2,000με, with 500με strain change per step. Fig. 6.6(b) shows S_{11} plot of the 2.4GHz patch antenna under different strain levels. As the applied strain increases, the antenna resonance frequency decreases gradually, as expected.

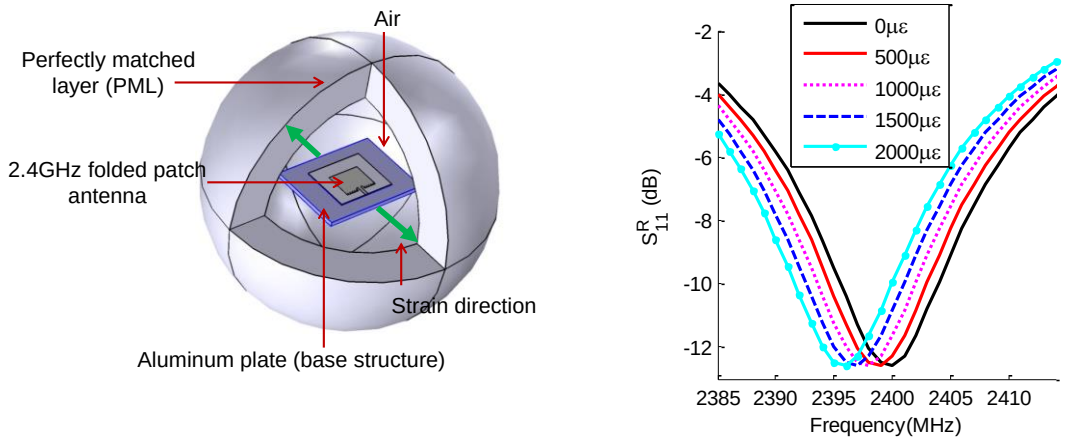

(a) Multi-physics simulation model of the 2.4 GHz receiving antenna

(b) Simulated S_{11}^R parameter under strain

Fig. 6.6. Multi-physics modeling and simulation for the receiving 2.4GHz patch antenna

Table 6.1. Number of elements and degrees for freedom in the receiving 2.4GHz patch antenna model

Number of elements		**Number of DOFs**	
Tetrahedron	165,560	Mechanics	435,252
Prism	6,540		
Triangle	19,983	Electromagnetics	1,144,094

6.2.2 Harmonic Simulation of Matching Network

The power flow through the 2.4GHz receiving patch antenna to the input port (Port 1) of the matching network is described as:

$$P_1 = [1 - (S_{11}^{\mathrm{R}})^2]P_0 \tag{6.2}$$

where P_0 is set to –10dBm from experimental measurement and S_{11}^{R} from different strain levels are obtained by COMSOL simulation, as presented in Fig. 6.6(b).

To characterize backscattering resonance of the sensor, sensor response for a neighborhood frequency range needs to be analyzed. With P_1 as input, conversion gain G_c of the matching network, generated by the harmonic balance simulation in ADS, is used to calculate the output power at Port 2 of the matching network as $P_2 = G_c P_1$. The output power result is plotted in Fig. 6.7.

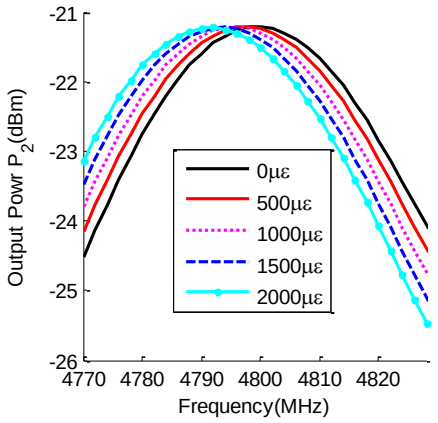

Fig. 6.7. Output power P_2 from matching network

6.2.3 Transmitting 4.8GHz Antenna with Backscattered Signal

The final step of the sensor operation is to let the power P_2 flow through the 4.8GHz patch antenna. The simulated scattering parameter S_{11}^{T} is needed to estimate overall output power P:

$$P_1 = [1 - (S_{11}^{\mathrm{R}})^2]P_0 \tag{6.3}$$

The simulation results for overall output power P are shown in Fig. 6.8(a). Resonance frequency of the entire sensor decreases as applied strain increases. The

resonance frequency at each strain level is extracted from Fig. 6.8(a), and linear regression is performed between strain and resonance frequency in Fig. 6.8 (b). The figure shows a strain sensitivity of –3.642 kHz/με, which is more than five times higher than the RFID-based antenna sensor. In addition, the coefficient of determination is close to be one, which indicates a good linearity.

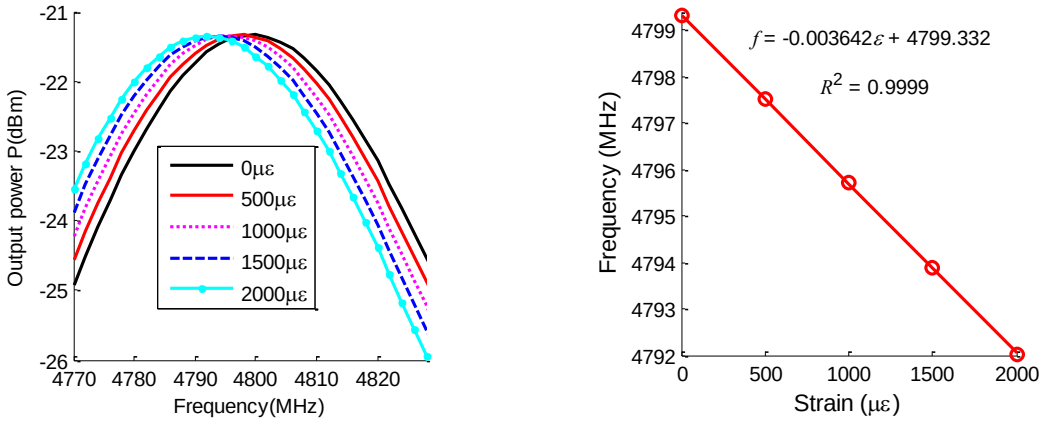

(a) Output power at different strain levels (b) Resonance frequency versus strain

Fig. 6.8. Multi-physics simulation results of an entire frequency doubling antenna sensor

6.3 Anti-Data-Collision Method for Frequency Doubling Antenna Sensor

Frequency doubling technology is a convenient signal modulation method for antenna strain sensors, because response signals are easily distinguishable from electromagnetic environmental reflections through harmonics of interrogation signals. However, a basic frequency doubling technique cannot distinguish multiple sensors. In this section, an anti-data-collision method for frequency doubling antenna sensor is presented. Section 6.3.1 presents a wireless switch to realize the anti-data-collision for frequency doubling antenna sensors. Section 6.3.2 provides detailed design of the frequency doubling switch with antennas, and an RF rectifier.

6.3.1 Scheme of Anti-Data-Collision Method

The frequency doubling is achieved through the second harmonic performance of the Schottky diode output. Harmonic waves are generated due to nonlinearity Relationship between voltage and current for the Schottky diode can be described by the following equation [56].

$$I = \frac{dV}{dt} C_j + I_s \left(e^{\frac{V - IR_S}{V_T}} - 1 \right) \tag{6.4}$$

where I is the current across the diode; V is the voltage; C_j is the junction capacitance; I_s is the saturation current; R_s is the series resistance; V_T is thermal voltage. The voltage V of the diode can be separated into DC biasing voltage V_{bias} and AC signal voltage V_{sig} (i.e. $= V_{bias} + V_{sig}$). If V_{bias} is closed to zero, V_{sig} will generate nonlinear current I, which causes harmonic waves. However, if V_{bias} is nearby the turn-on value (i.e. $V = IR_s$) of the diode, the exponential term of Eq. (6.4) is closed to one and the equation of AC signal I_{sig} is simplified [56].

$$I_{sig} = \frac{dV_{sig}}{dt} C_j + \frac{V_{sig}}{R_S} \tag{6.5}$$

Thus, I_{sig} would be linear and no harmonic wave generates. This is the main switching mechanism to turn on/off frequency doubling.

In order to apply the switching mechanism to a frequency doubling antenna sensor, Fig. 6.9 shows the schematic of a wireless switch. While operation mechanism of the frequency doubling antenna sensor is the same as Fig. 2.4, a wireless switch mechanism is added. When a disabling signal from the reader-side switch antenna is sent to the wireless switch, the switch captures the electromagnetic power and uses an RF rectifier to generate a DC voltage. The DC voltage is then applied to the diode in the matching network of the frequency doubling antenna sensor, disabling the frequency

doubling and effectively turning off the sensor. When the disabling signal from the reader-side switch antenna is removed, the frequency doubling antenna sensor resumes operations. The signal from the reader-side wireless switch antenna should have an operation frequency different from the sensor operating frequencies (e.g. 2.4GHz and 4.8GHz) to avoid interference to operation.

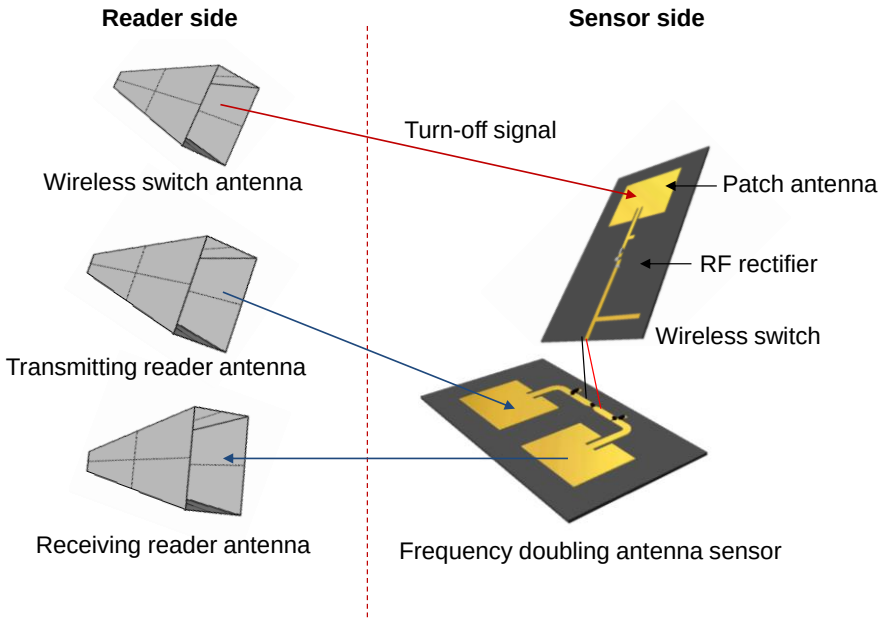

Fig. 6.9. Schematic of switching on/off a frequency doubling antenna sensor

6.3.2 Wireless Switch Design of Frequency Doubling System

The wireless switch of a frequency doubling antenna sensor consists of two components. The first component is an antenna for receiving disable signal from the reader. The second component is an RF rectifier for rectifying the RF power (AC) to DC voltage. In order to distinguish two frequency doubling antenna sensors, disabling signals with two different frequencies are needed. Therefore, Section 6.3.2.1 presents two patch antenna designs (2.9GHz and 3.6GHz). Section 6.3.2.2 presents the RF rectifier design.

6.3.2.1 Two antenna designs (2.9GHz and 3.6GHz)

A 2.9GHz and a 3.6GHz patch antennas are designed on the Rogers 5880 substrate with 0.7874mm (31mil) thickness. Each antenna will be connected to an RF rectifier for switching on/off a frequency doubling sensor. Fig. 6.10 shows the design of the 2.9GHz patch antenna. The planar dimension of the 2.9GHz patch antenna is 44.5mm × 34.3mm (Fig. 6.10(a)). The simulated scattering parameter S_{11} from COMOSOL is around -13dB at operating frequency 2.9GHz (Fig. 6.10(b)).

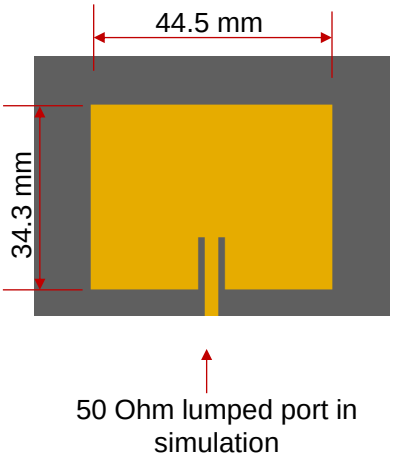

(a) Dimensions of the 2.9GHz patch antenna

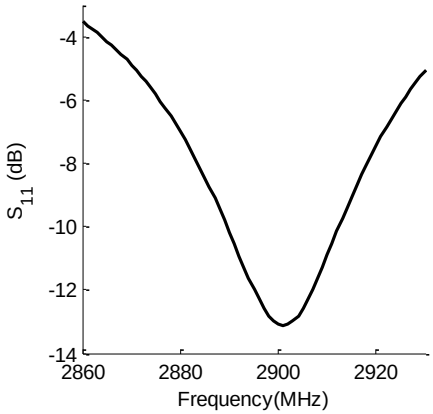

(b) Simulated S_{11} parameter

Fig. 6.10. 2.9GHz patch antenna design

Fig. 6.11 shows the design of the 3.6GHz patch antenna with a planar dimension of 35.8mm × 27.8mm. In order to investigate impedance matching performance of the patch antenna at its resonance frequency 3.6GHz, scattering parameter S_{11} is simulated by COMOSOL (Fig. 6.11(b)). The S_{11}has the lowest value of -30dB near 3.6GHz.

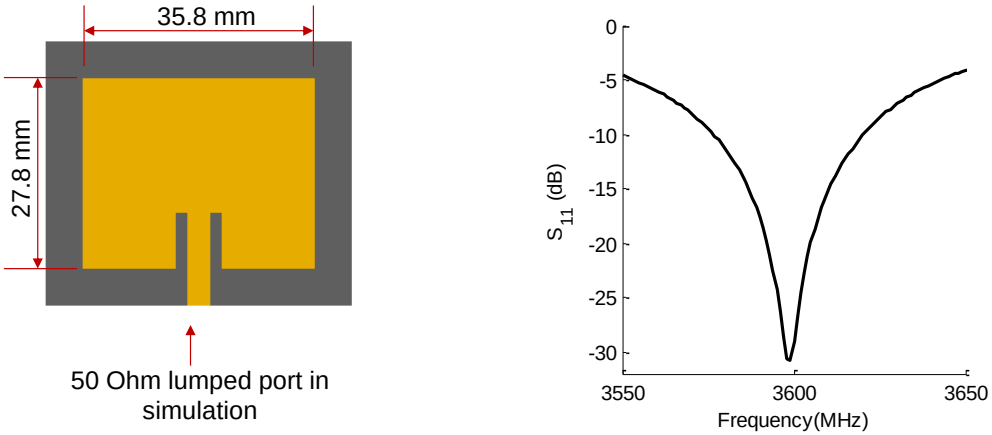

(a) Dimensions of the 3.6GHz patch antenna

(b) Simulated S_{11} parameter

Fig. 6.11. 3.6GHz patch antenna design

6.3.2.2 RF rectifier design

A single-stage RF rectifier is designed to convert RF power to DC power (voltage) as shown in Fig. 6.12. The dimension of the RF rectifier is 74.0mm × 52.0mm, designed on the Rogers 5880 substrate. Two Schottky diodes are adopted in the design. Capacitors of 30, 50, and 500pF store the DC charge and match the impedance. The input port is connected to a patch antenna to be provided with RF power. After rectifying, DC current and voltage are generated at the output port.

For performance evaluation of the RF rectifier, ADS simulation is conducted and results are as shown in Fig. 6.13. Two frequency levels, 2.9GHz and 3.6GHz are simulated and input power is set to 5dBm. The power level of 5dBm is obtained from an experimental measurement when transmitting power from the switching antenna (reader-side) is 25dBm and the distance between the switching antenna and the sensor is 12in. After 1000ns, simulated DC voltages from 2.9GHz and 3.6GHz input power are rectified to 1200mV and 1300mV, respectively. The obtained DC voltages are much higher than the required forward biasing voltage (400mV) of the Schottky diode, and thus, can disable the corresponding frequency doubling sensor.

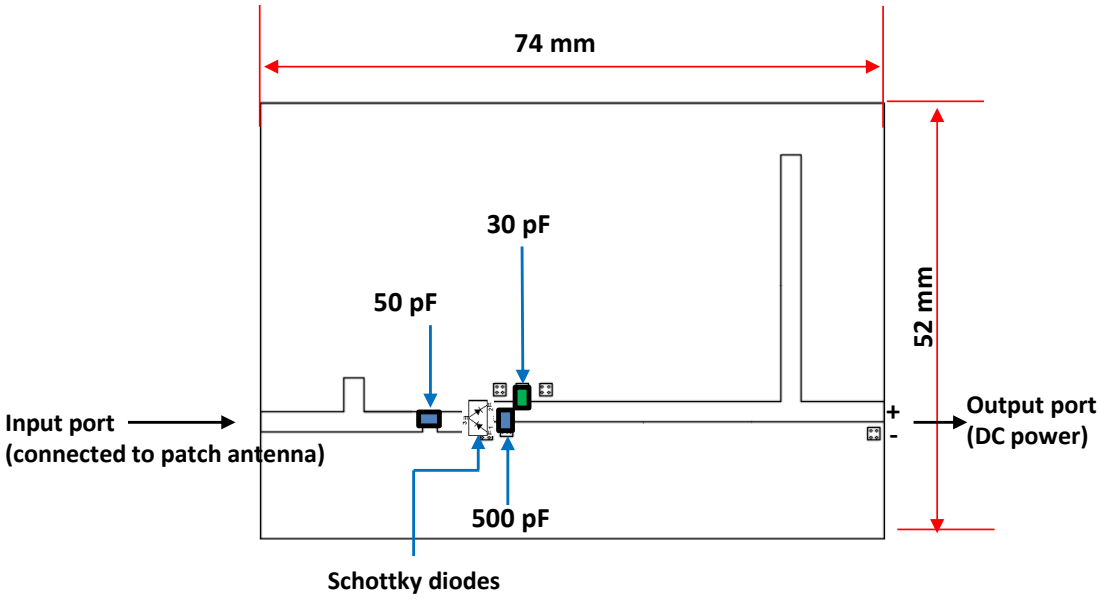

Fig. 6.12. Single-stage RF rectifier design

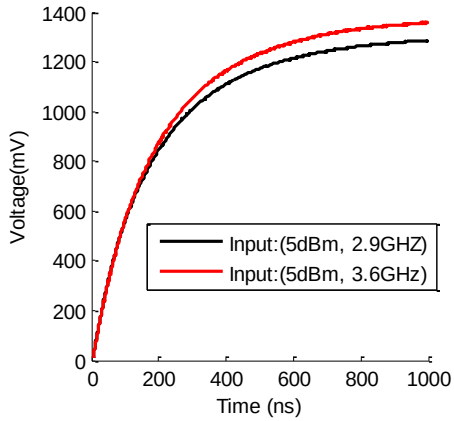

Fig. 6.13. ADS simulation result of the RF rectifier

6.4 Experimental Validation

In order to validate the sensor performance, two experimental tests were conducted. Strain sensing performance with a single frequency doubling antenna sensor is shown in Section 6.4.1. A wireless switching test is described in Section 6.4.2.

6.4.1 Strain Sensing Experiment with a Single Frequency Doubling Sensor

To investigate strain sensing performance of the frequency doubling antenna sensor, a tensile test with a single sensor is first conducted. As shown in Fig. 6.14(a), only the 2.4GHz transmitting antenna of the sensor is bonded to the surface of an aluminum plate, while all other components float over the structural surface. The resonance frequency of the fabricated frequency doubling sensor can be different from simulation results due to soldering imperfection, environmental reflection, etc. Therefore, two trimer capacitors are used to physically rematch input and output impedances of the diode. Five strain gages are on the aluminum specimen installed for reference. The specimen is mounted on the 22-kip SATEC machine (Fig. 6.14(b)).

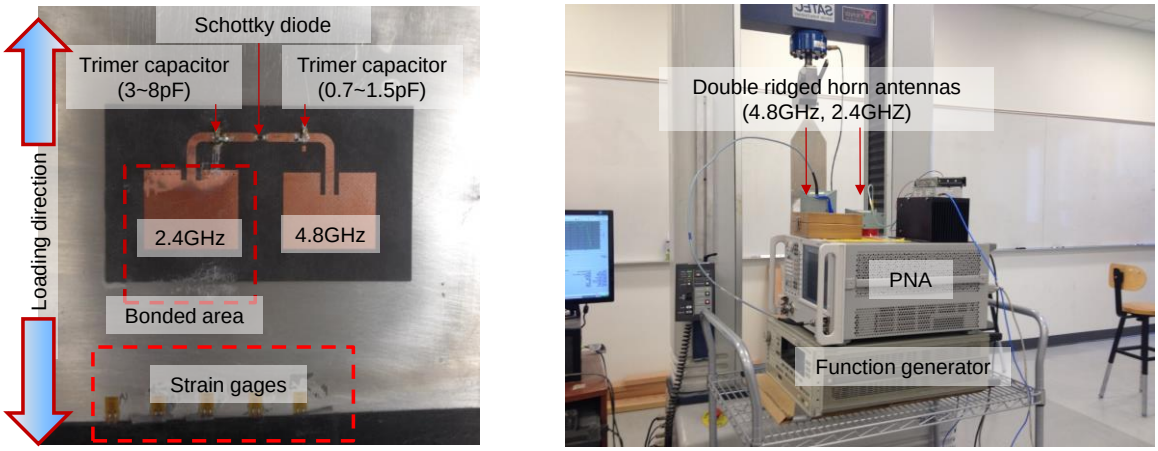

(a) Sensor configuration (b) Experimental setup

Fig. 6.14. Tensile test of frequency doubling antenna sensor

During the test, the interrogation distance between reader antennas and the sensor is set as 12in. At the reader side, two 12dBi double-ridged horn antennas are placed at the reader side. The tensile loading to the aluminum plate is increased to generate strain up to 300με, with 50με increment per loading step. At every strain level, the function generator (Agilent 83622B) with a power amplifier sweeps the 2.4GHz frequency band (*f*) at 25dBm transmitted power level. The PNA (Agilent N5222A) captures the sensor

responses at doubled frequency (2*f*). For clarity, power received by the PNA of only four strain levels is plotted in Fig. 6.15(a). The resonance frequency at each strain level is then extracted. Finally, the relationship between resonance frequency and strain is plotted in Fig. 6.15(b), and linear regression is performed. The strain sensitivity is –3.71kHz/με, which is close to the simulated strain sensitivity (–3.642kHz/με) in Section 6.2. The determination of coefficient is 0.9905, which shows good linearity.

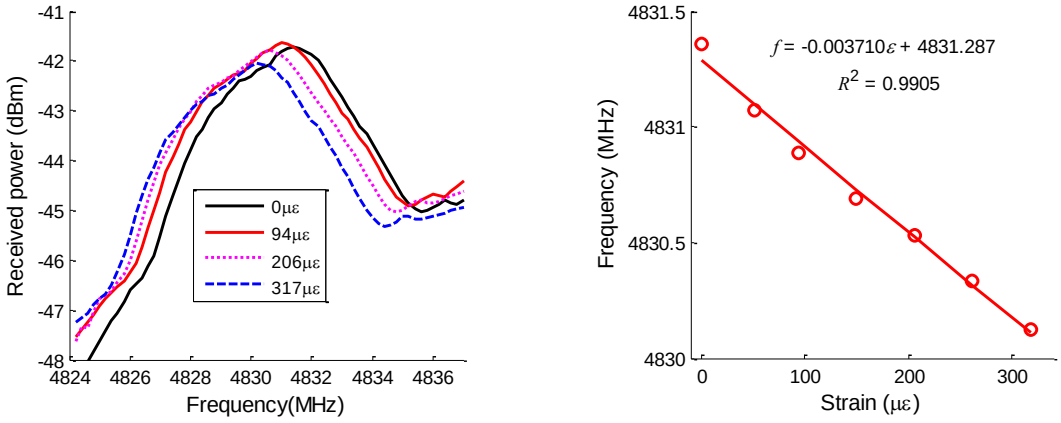

(a) Average received power (b) Resonance frequency change versus strain

Fig. 6.15. Tensile test results of frequency doubling antenna sensor

6.4.2 Tensile Test with Sensor Array

To validate strain sensing performance with multiple-sensor deployment, a tensile test with two frequency doubling antenna sensors (Sensor 1 and Sensor 2) is conducted. Fig. 6.16(a) and (b) show experimental setup for the tensile test with two frequency doubling antenna sensors. At the reader side, two double ridged horn antennas are placed with the 12in. interrogation distance away from the two sensors. Another double ridged horn antenna is used as the reader-side wireless switch antenna which transmits 2.9GHz or 3.6GHz signals to provide RF power to switch on/off a sensor. At the sensor side, both switch units (Switch 1 and Switch 2) are placed next to the sensor which are installed on the aluminum plate (Fig. 6.16(c)). DC cables from Switch 1 and 2 are connected to

Sensor 1 and 2, respectively. Fig. 6.16(d) shows the frequency doubling switches. Trimer capacitors on each switch are adjusted to maximize reflected DC power at 2.9GHz and 3.6 GHz, respectively.

When Sensor 1 is interrogated, the reader-side switch antenna transmits a 3.6GHz signal to turn off Sensor 2. On the contrary, When Sensor 2 is interrogated, the wireless switch antenna transmits a 2.9GHz signal to turn off Sensor 1. The tensile loading is applied to generate strain up to 250με, with 50με increment per loading step. Two sensors are sequentially interrogated at each strain level. For clarity, received power at three strain levels for each sensor is plotted in Fig. 6.16(a) and (b). Strain sensitivities of Sensor 1 and Sensor 2 are −3.423 and −3.572kHz/με, respectively. The linearity of two sensors are close to 1.0 (Sensor1: 0.9248 and Sensor2: 0.9609).

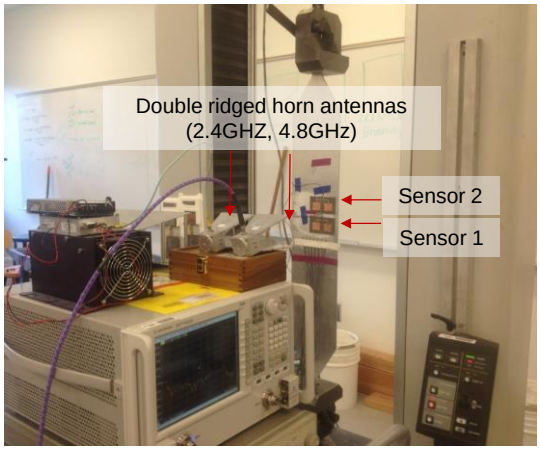

(a) Experimental setup (right view)

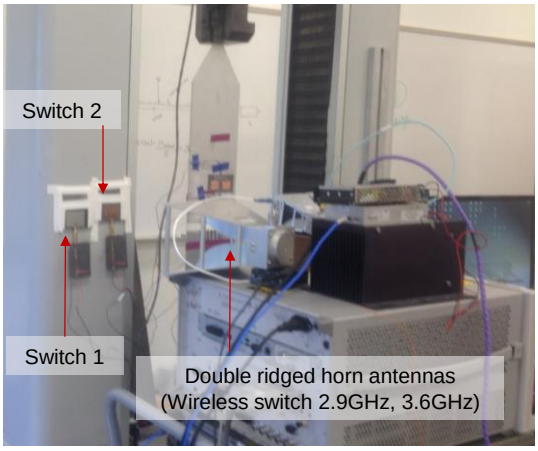

(b) Experimental setup (left view)

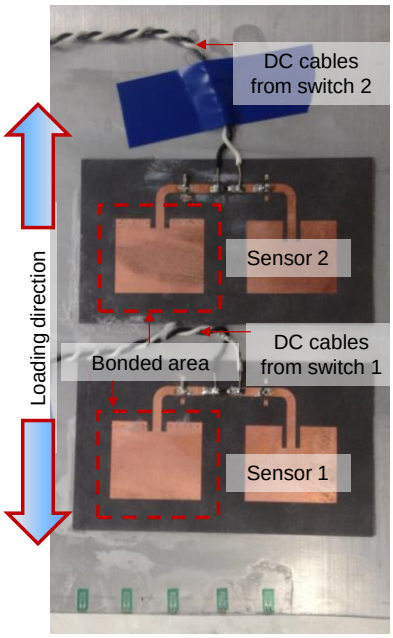

(c) Sensor configuration

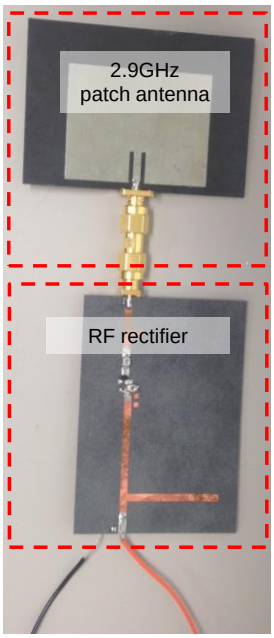

(d) Switch with 2.9GHz patch antenna

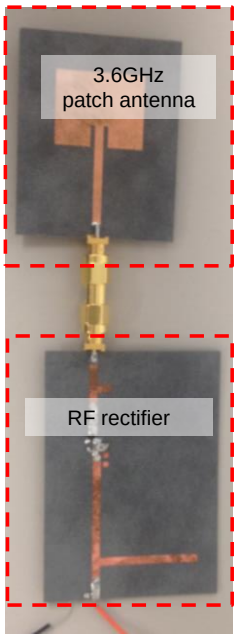

(e) Switch with 3.6GHz patch antenna

Fig. 6.16. Tensile test with an array of frequency doubling antenna sensors

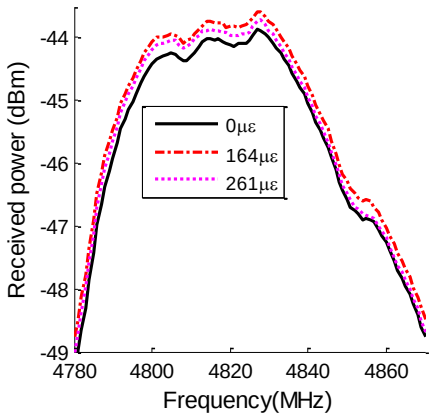

(a) Average received power (sensor 1)

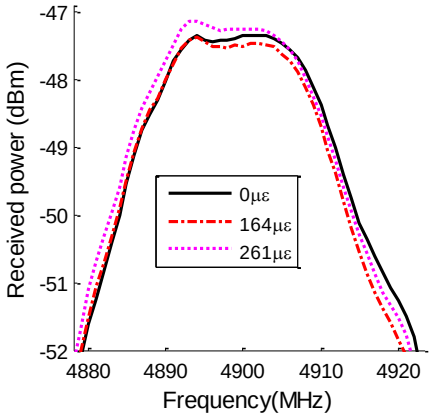

(b) Average received power (sensor 2)

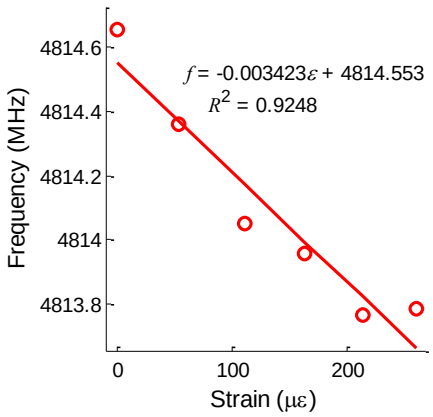

(c) Resonance frequency change versus strain (sensor 1)

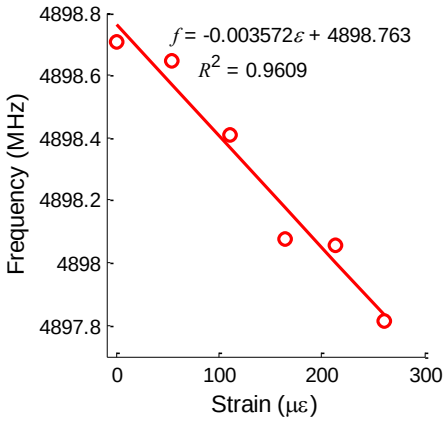

(d) Resonance frequency change versus strain (sensor 2)

Fig. 6.17. Test results for the sensor array

6.5 Summary

In this chapter, a novel frequency doubling technique is proposed for passive (battery-free) wireless strain measurement. A 2.4 to 4.8GHz frequency doubling antenna sensor is designed. The wireless strain sensing performance is first estimated by multi-physics modeling and simulation. Validation experiments are conducted to characterize wireless strain sensing performance. Tensile testing shows a strain sensitivity of –3.710kHz/με and a determination coefficient of 0.9905. The strain sensitivity of the frequency doubling sensor is around five times of previously developed RFID antenna sensors. A new wireless switching mechanism for frequency doubling sensors is also

proposed and validated. A frequency doubling antenna sensor is turned off when a forward biasing voltage is applied to its frequency doubling diode. The experimental results demonstrate the potential of a frequency doubling antenna sensor array for wireless strain sensing.

CHAPTER 7 SUMMARY

This dissertation develops passive (battery-free) wireless strain sensing techniques for low-cost structural health monitoring. Through the innovative modeling and numerical solution, computational speed for strain sensing simulation is significantly improved. Accurate multi-physics FE modeling is achieved using the updated model parameters. In addition, an optimization framework for antenna sensor design is proposed and numerically and experimentally validated. Finally, in order to overcome the limit of RFID antenna sensors, a frequency doubling technology is investigated. To achieve close deployment of multiple frequency doubling antenna sensors, a wireless switching mechanism is designed and implemented. Performance of frequency doubling antenna sensors with wireless switches is experimentally validated. The main contributions are summarized in Section 7.1. Section 7.2 discusses future work of the research.

7.1 Contributions

The dissertation has made contributions in the following areas:

1. Current numerical approach for strain sensing requires a high computational load which limits the ability to improve antenna sensor design. To improve solution efficiency, a partially air-filled cavity model is proposed. This model not only reduces computational efforts but also maintains similar accuracy as the previous approach (i.e. the full-wave model with the frequency domain solver). To further improve the solution efficiency, the inverse power iteration with Rayleigh quotient (IPIRQ) method is proposed for eigenfrequency solution. Compared to other methods such as the Rayleigh quotient iteration (RQI) method and MATLAB `eigs` command in this application, the IPIRQ method shows the best trade-off between simulation accuracy and computation time.

2. A model updating framework is proposed to reduce discrepancy between numerical solution and experimental measurement. To update both mechanical and

electromagnetic parameters, extensive experiments are first conducted. Based on experimental data, mechanical and electromagnetic parameters are updated through numerical optimization. The model updating provides an FE model with accurate parameters, so that model predictions more accurately match experimental results.

3. To maximize performance of an antenna sensor, a design optimization framework is proposed. A multi-objective (including strain sensitivity and antenna gain) function is formulated, with geometry parameters of top copper pattern as optimization variables. In the numerical solution, the strain sensitivity is improved to –685Hz/με from –624.84Hz/με and the optimized antenna gain is improved to –5.16dB from –5.37dB. In the experimental validation, the strain sensitivity is improved to –741Hz/με. Around 0.65dB of radiation gain is improved compared to the original design.

4. As an alternative signal modulation, the frequency doubling scheme is implemented into antenna sensors to overcome the limit of RFID antenna sensors. A special three-step multi-physics simulation method is proposed to evaluate the performance of the frequency doubling antenna sensor. Upon fabrication and experimental testing, the measured strain sensitivity is shown to be –3.710kHz/με and the determination of coefficient is 0.9905. The strain sensitivity of the frequency doubling sensor is around five times of the RFID antenna sensors. Furthermore, a novel wireless switching mechanism for frequency doubling antenna sensors is proposed and implemented to conveniently turn on/off a sensor in an array.

7.2 Future Work

Based on the current research achievements, future research can be expanded into following directions.

1. Performance of antenna sensors has been mainly validated by laboratory tests. In order to perform long-term field monitoring with antenna sensors, large amount of studies need to be devoted to reliability and robustness of the antenna sensors in outdoor

conditions. For example, a waterproof film to prevent top copper on an antenna sensor from corrosion needs to be incorporated.

2. Performance consistency under environmental influences needs further study. Although both the RFID antenna sensor and the frequency doubling sensor show promising results for wireless strain sensing, performance is affected by environmental conditions such as temperature and electromagnetic reflections. Therefore, better understanding about far-field electromagnetic behavior and temperature effect is needed. Appropriate calibration methods can be studied.

3. The maximum interrogation distance of present antenna strain sensors is shown to be around 2m. This distance can be inconvenient in practice. To improve interrogation distance, energy harvesting techniques such as solar cells can be incorporated. Power collected by energy harvesting techniques can be used to increase wireless interrogation distance.

REFERENCES

[1] H. Sohn, C. R. Farrar, F. M. Hemez, D. D. Shunk, D. W. Stinemates, and B. R. Nadler, "*A Review of Structural Health Monitoring Literature: 1996-2001*," Los Alamos National Laboratory, Los Alamos, NM Report No. LA-13976-MS, 2003.

[2] F.-K. Chang and A. Güemes, "Structural Heath Monitoring 2013: A Roadmap to Intelligent Structures," Lancaster, PA, USA, 2013.

[3] M. Çelebi, "*Seismic Instrumentation of Buildings (with Emphasis on Federal Buildings)*," United States Geological Survey, Menlo Park, CA Report No. 0-7460-68170, 2002.

[4] X. Yi, T. Wu, Y. Wang, R. T. Leon, M. M. Tentzeris, and G. Lantz, "Passive wireless smart-skin sensor using RFID-based folded patch antennas," *International Journal of Smart and Nano Materials*, vol. 2(1), pp. 22-38, 2011.

[5] X. Yi, C. Cho, J. Cooper, Y. Wang, M. M. Tentzeris, and R. T. Leon, "Passive wireless antenna sensor for strain and crack sensing-electromagnetic modeling, simulation, and testing," *Smart Materials and Structures*, vol. 22(8), p. 085009, 2013.

[6] X. Yi, C. Cho, B. Cook, Y. Wang, M. M. Tentzeris, and R. T. Leon, "A slotted patch antenna for wireless strain sensing," in *Proceedings of the ASCE 2014 Structures Congress*, Boston, MA, USA, 2014.

[7] X. Yi, Y. Wang, M. M. Tentzeris, and R. T. Leon, "Multi-physics modeling and simulation of a slotted patch antenna for wireless strain sensing," in *Proceedings of the 9th International Workshop on Structural Health Monitoring (IWSHM)*, pp. 1857-1864, Stanford, CA, USA, 2013.

[8] E. G. Straser and A. S. Kiremidjian, "*A Modular, Wireless Damage Monitoring System for Structures*," John A. Blume Earthquake Eng. Ctr., Stanford University, Stanford, CA Report No. 128, 1998.

[9] J. P. Lynch, K. H. Law, A. S. Kiremidjian, C. E., C. R. Farrar, H. Sohn, D. W. Allen, B. Nadler, and J. R. Wait, "Design and performance validation of a wireless sensing unit for structural health monitoring applications," *Structural Engineering and Mechanics*, vol. 17(3-4), pp. 393-408, 2004.

[10] Y. Wang, J. P. Lynch, and K. H. Law, "A wireless structural health monitoring system with multithreaded sensing devices: design and validation," *Structure and Infrastructure Engineering,* vol. 3(2), pp. 103-120, 2007.

[11] J. P. Lynch and K. J. Loh, "A summary review of wireless sensors and sensor networks for structural health monitoring," *The Shock and Vibration Digest,* vol. 38(2), pp. 91-128, 2006.

[12] G. Park, T. Rosing, M. D. Todd, C. R. Farrar, and W. Hodgkiss, "Energy harvesting for structural health monitoring sensor networks," *Journal of Infrastructure Systems,* vol. 14(1), pp. 64-79, 2008.

[13] A. Deivasigamani, A. Daliri, C. H. Wang, and S. John, "A review of passive wireless sensors for structural health monitoring," *Modern Applied Science,* vol. 7(2), pp. 57-76, 2013.

[14] F. Gasco, P. Feraboli, J. Braun, J. Smith, P. Stickler, and L. DeOto, "Wireless strain measurement for structural testing and health monitoring of carbon fiber composite," *Composite Part A: Applied Science and Manufacturing,* vol. 42(9), pp. 1263-1274, 2011.

[15] J. C. Butler, A. J. Vigliotti, F. W. Verdi, and S. M. Walsh, "Wireless, passive, resonant-circuit, inductively coupled, inductive strain sensor," *Sensors and Actuators A: Physical,* vol. 102(1-2), pp. 61-66, 2002.

[16] K. J. Loh, J. P. Lynch, and N. A. Kotov, "Inductively coupled nanocomposite wireless strain and pH sensors," *Smart Structures and Systems,* vol. 4(5), pp. 531-548, 2008.

[17] Y. Jia, K. Sun, F. J. Agosto, and M. T. Quinones, "Design and characterization of a passive wireless strain sensor," *Measurement Science and Technology,* vol. 17(11), pp. 2869-2876, 2006.

[18] A. Daliri, A. Galehdar, S. John, C. H. Wang, W. S. T. Towe, and K. Ghorbani, "Wireless strain measurement using circular microstrip patch antennas," *Sensors and Actuators A: Physical,* vol. 184(1), pp. 86-92, 2012.

[19] S. Deshmukh and H. Huang, "Wireless interrogation of passive antenna sensors," *Measurement Science and Technology,* vol. 21(3), 2010.

[20] X. Xu and H. Huang, "Battery-less wireless interrogation of microstrip patch antenna for strain sensing," *Smart Materials and Structures,* vol. 21(12), p. 125007, 2012.

[21] X. YI, C. Cho, J. Cooper, R. Vyas, Y. Wang, M. M. Tentzeris, and R. T. Leon, "Passive frequency doubling antenna sensor for wireless strain sensing," in *Proceeding of the ASME 2012 Conference on Smart Materials, Adaptive Structures and Intelligent Systems (SMASYS 2012),* Stone Mountain, GA, USA, 2012.

[22] K. S. Yee, "Numerical solution of initial boundary-value problems involving Maxwell's equations in isotropic media," *IEEE Transactions on Antennas and Propagation,* vol. AP-14(pp. 302-307, 1966.

[23] A. Taflove, "Review of the formulation and applications of the finite-difference time-domain method for numerical modeling of electromagnetic wave interactions with arbitrary structures," *Wave Motion,* vol. 10(6), pp. 547-582, 1988.

[24] N. A. Bushyager and M. M. Tentzeris, "*MRTD (Multi Resolution Time Domain) Method in Electromagnetics*." USA: Morgan & claypool, 2005.

[25] J. M. Jin, "*The Finite Element Method in Electromagnetics*," 2nd ed. New York: John Wiley & Sons, Inc., 2002.

[26] J. L. Volakis, A. Chatterjee, and L. C. Kempel, "*Finite Element method for Electromagnetics: with Applications to Antenna, Microwave Circuits, and Scattering*." New York, NY: The Institute of Electrical and Electronics Engineers, Inc., 1998.

[27] M. Clemens and T. Weiland, "Discrete electromagnetism with the finite integration technique," *Progress in Electromagnetics Research,* vol. 32(pp. 65-87, 2001.

[28] M. M. Ney, "Method of moments as applied to electromagnetics problems," *IEEE Transcations on Microwave Theory and techniques,* vol. 33(10), pp. 972-980, 1985.

[29] A. A.T., "An introduction to the method of moments," *Computer Physics Communications,* vol. 68(1-3), pp. 1-18, 1974.

[30] COMSOL, "*COMSOL multiphysics reference guide*," COMSOL, Inc., Burlington, MA, USA 2012.

[31] ANSYS Inc., "*ANSYS Coupled-field Analysis Guide*," ANSYS Inc., Canonsburg, PA, USA 2005.

[32] X. YI, "*Wireless antenna sensors for strain and crack monitoring*," Ph.D. Dissertation, *Georgia Institute of Technology*, Atlanta, 2014.

[33] L. Yu, L. Cheng, L. H. Yam, and Y. J. Yan, "Application of eigenvalue perturbation theory for detecting small structural damage using dynamic responses," *Composite Structures,* vol. 78(3), pp. 402-409, 2007.

[34] S. H. Chen, X. W. Yang, and H. D. Lian, "Comparison of several eigenvalue reanalysis methods for modified structures," *Structural and Multidisciplinary Optimization,* vol. 20(4), pp. 253-259, 2000.

[35] B. N. Parlett, "*The Symmetric Eigenvalue Problem*." Englewood Cliffs, NJ: Prentice-Hall, 1980.

[36] C. A. Balanis, "*Advanced Engineering Electromagnetics*." New York: Wiley & Sons, 1989.

[37] X. Yi, C. Cho, B. Cook, Y. Wang, M. M. Tentzeris, and R. T. Leon, "Design and simulation of a slotted patch antenna sensor for wireless strain sensing," in *Proceedings of SPIE, Nondestructive Characterization for Composite Materials, Aerospace Engineering, Civil Infrastructure, and Homeland Security*, p. 86941J, San Diego, California, USA, 2013.

[38] Voyantic, "*Tagformance Lite Measurement System User Guide*." Espoo, Finland: Voyantic Ltd., 2011.

[39] EPCglobal Inc., "*EPC^{TM} Radio-frequency Identity Protocols Class-1 Generation-2 UHF RFID Protocol for Communications at 860 MHz-960 MHz* " EPCglobal Inc. Version 1.2.0, 2008.

[40] W. C. Chew and W. H. Weedon, "A 3-D perfectly matched medium from modified Maxwell's equations with stretched coordinates," *Microwave and Optical Technology Letters,* vol. 7(13), pp. 599-604, 1994.

[41] H. Guo, B. Oswald, and P. Arbenz, "3-dimensional eigenmodal analysis of plasmonic nanostructures," *Optics Express,* vol. 20(5), pp. 5481-5500, 2012.

[42] A. Chatterjee, J. M. Jin, and J. L. volakis, "Edge-based finite elements and vector ABC's applied to 3-D scattering," *IEEE Transactions on Antennas and Propagation* vol. 41(2), pp. 221-226, 1993.

[43] D. M. Pozar, "*Microwave Engineering*," 4th ed. New York, 2012.

[44] F. Tisseur and K. Meerbergen, "The quadratic eigenvalue problem," *SIAM Review,* vol. 43(2), pp. 235-286, 2001.

[45] T. G. Wright and L. N. Trefethen, "Large-scale computation of pseudospectra using ARPACK and eigs," *Journal of Scientific Computing,* vol. 23(2), pp. 591-605, 2001.

[46] J. A. George and J. W.-H. Liu, "*Computer Solution of Large Sparse Positive Definite Systems*." Hanford, CA.: Prentice-Hall, 1981.

[47] J. H. Wilkinson, "*The Algebraic Eigenvalue Problem*." Oxford: Clarendon Press, 1965.

[48] M. Menegotto and E. Pinto., "Method of analysis for cyclically loaded reinforced concrete plane frames including changes in geometry and non-elastic behavior of elements under combined normal force and bending," in *IABSE Symposium,* Lisbon, Portugal. , 1973.

[49] M. Bruneau, C.-M. Uang, and A. Whittaker, "*Ductile design of steel structures*." New-York: Mcgraw-Hill, 1998.

[50] "ASTM D638," in *Standard Test Method for Tensile Properties of Plastics*(Issue): American Society of Testing and Materials, 2005.

[51] "ASTM D3380-10," in *Standard test Method for Relative Permittivity (Dielectric Constant) and Dissipation Factor of Polymer-Based Microwave Circuit Substrates*(Issue): American Society of Testing and Materials, 2010.

[52] Y. Peng, Y. M. Shkel, and G. Kim, "Stress dielectric response in liquid polymers," *Journal of rheology,* vol. 49(p. 297, 2005.

[53] L. D. Landau, E. M. Lifshitz, and L. P. Pitaevskii, "*Electrodynamics of Continuous Media*," vol. 8: Oxford: Butterworth-Heinenann, 1984.

[54] J. A. Stratton, "*Electromagnetic theory*." New York: McGraw-Hill, 1941.

[55] Y. M. Shkel and D. J. Klingenberg, "Electrostriction of polarizable materials: Comparison of models with experimental data," *Journal of physics,* vol. 83(15), pp. 7834-7843, 1998.

[56] J. R. Cooper, B. S. Cook, and M. M. Tentzeris, "The first hardware-based, anti-collision methodology for frequency doubling transceivers for RFID and wireless sensing applications," in *Microwave Symposium (IMS)*, Phoenix, AZ, 2014.

[57] S. A. Maas, "*Nonlinear Microwave and RF Circuits*," 2nd ed. Norwood, MA: Artech House, 2003.